LA-6561-T
Thesis

UC-34c

Issued: October 1976

Measurements of Pion-Helium Total Cross Sections at Energies from 51 to 105 MeV

by

Kenneth F. Johnson*

*LAMPF Guest Scientist. Physics Department, Temple University, Philadelphia, PA 19122.

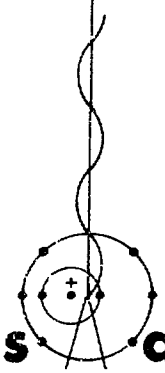

los alamos
scientific laboratory
of the University of California
LOS ALAMOS, NEW MEXICO 87545

An Affirmative Action/Equal Opportunity Employer

UNITED STATES ENERGY RESEARCH AND DEVELOPMENT ADMINISTRATION
CONTRACT W-7405-ENG. 36

This thesis was submitted to the New Mexico State University, Las Cruces, NM, in partial fulfillment of the requirements for the degree of Doctor of Philosophy. It is the independent work of the author and has not been edited by the Technical Information staff.

This work was supported by the US Energy Research and Development Administration, Division of Physical Research.

Printed in the United States of America. Available from
National Technical Information Service
U.S. Department of Commerce
5285 Port Royal Road
Springfield, VA 22161
Price: Printed Copy $7.75 Microfiche $2.25

TABLE OF CONTENTS

TABLE OF CONTENTS--(cont'd.)

TABLE OF CONTENTS--(cont'd.)

LIST OF TABLES

LIST OF TABLES--(cont'd.)

List of Figures

LIST OF FIGURES--(cont'd.)

ABSTRACT

MEASUREMENTS OF PION-HELIUM TOTAL CROSS SECTIONS

AT ENERGIES FROM 51 TO 105 MeV

BY

KENNETH FLOYD JOHNSON, B.S., M.S.

Doctor of Philosophy in Physics

New Mexico State University

Las Cruces, New Mexico, 1976

Professor George R. Burleson, Chairman

Measurements of $\pi^{\pm}$-^{4}He total cross sections have been made at energies from 51 to 105 MeV using a superfluid ^{4}He target at the Low Energy Pion channel of the LAMPF accelerator in Los Alamos. Pions were selected with either a DISC counter or a time-of-flight system. The scattered pions were detected by a series of circular plastic scintillation counters using standard transmission techniques. The resulting partial removal cross sections were

extrapolated to zero solid angle after being corrected for Coulomb effects, pion decay, accidental counts, counter absorption and efficiencies, and statistical correlations. The resulting statistical errors were generally ~3-5%. The measured total cross sections were found to be in good statistical agreement with previous measurements and in poor agreement with the predictions of several optical potentials in current use. Through an optical theorem the imaginary part of the forward scattering amplitude was found. The total cross sections have been used with previously-measured angular distributions through a phenomenological model to obtain the real part of the forward scattering amplitude at four energies between 50 and 75 MeV. These results were found to be in good agreement with forward dispersion relation calculations.

1. INTRODUCTION

Ever since their discovery in 1947,[1] and their later production by particle accelerators, pions have been used to probe the nucleus. The early experiments suffered from the low intensity and poor energy resolution of the then available pion beams as compared to conventional nuclear beams (protons, neutrons, alphas, etc.). In recent years, the quality of data from pion-nucleus scattering experiments has greatly improved and a review of these experiments is given by Stroot.[2] They are expected to continue to improve with the completion of the new meson facilities. They will provide high-intensity pion beams with good energy resolution.

The Pion as a Nuclear Probe

There are several properties of the pion which make it attractive as a nuclear probe. The mass of the charged pion is $m_{\pi^{\pm}} = 139.6$ MeV, and that of the neutral pion is $m_{\pi^0} = 135.0$ MeV. This makes the pion the lightest of the strongly-interacting particles, having about 1/7 the mass of a nucleon. Consequently, a nucleon in the nucleus is less likely to suffer severe recoil effects in pion scattering than in the scattering of other strongly interacting particles.

The charged pion has a long lifetime (26 ns) which allows beams of charged pions to be transported over reasonable distances. The mean decay length λ of a charged pion is $\lambda = \frac{Pc}{mc^2} c\tau$ or $\lambda = 5.56P$ cm where P is the pion laboratory momentum in MeV, mc^2 the pion rest energy in MeV, and $c\tau$ the mean lifetime in cm.

Another property which makes the pion a useful probe is its zero spin. This greatly simplifies the theoretical analysis of pion reaction and scattering processes. Furthermore, it means that the pion is a boson. It can be created or destroyed singly. Pion production and absorption processes are fundamentally different from processes involving nucleons alone. Pion absorption has a drastic effect on a nucleus because it gives a minimum of ~140 MeV to the nucleus.

The pions (π^+, π^0, π^-) form an isospin triplet. This is of use in theoretical attempts to separate electromagnetic from strong interaction effects. The symmetry is not perfect since nuclei consist of neutral and positively-charged nucleons. Thus, in scattering off nuclei, positively- and negatively-charged pions of equal energy will experience different Coulomb effects which are not easily calculable in a model-independent way. Neutral pions have too short a lifetime to be a useful nuclear probe. The three charge states allow the pion to undergo double charge exchange in pion-nucleus scattering. This is an exotic feature not available in nucleon-nucleus scattering.

Another useful point about the pion as a nuclear probe is that the π-nucleon interaction is simple to describe theoretically in the isospin $T = 3/2$ state (i.e., $\pi^+ p$ or $\pi^- n$ interaction). In addition, the $T = 3/2$ state is much stronger than the $T = 1/2$ state in the energy range 50 to 400 MeV. This aspect of the π-nucleon interaction will be discussed later.

The increased interest in the pion as a nuclear probe has led to the building of meson facilities such as LAMPF (the Clinton P. Anderson Meson Physics Facility at the Los Alamos Scientific Laboratory), TRIUMF (the Tri-University Meson Facility in Vancouver, Canada), and SIN (Schweizerisches Institut Für Nuklearforschung in Zurich, Switzerland). The LAMPF machine is an 800 MeV proton linear accelerator with a design average beam current of 1 mA. The TRIUMF machine is a 500 MeV H^- cyclotron and the SIN machine is a 510 MeV proton ring-cyclotron. The TRIUMF and SIN accelerators both have a design average beam current of 100 μA.

Total Cross Section Measurement

The nuclear total cross section σ_{TOT} is defined as the sum of the total nuclear elastic cross section σ_{ne} and the total nuclear reaction cross section σ_r

$$\sigma_{TOT} = \sigma_{ne} + \sigma_r \tag{1}$$

In general it is of physical interest because it readily gives an overall picture of the strength of the interaction. Total cross sections provide constraints on the analysis of elastic scattering data through certain model-independent relations with elastic scattering amplitudes. Through the optical theorem σ_{TOT} is related to the imaginary part of the elastic forward scattering amplitude f by

$$\sigma_{TOT} = \frac{4\pi}{k} \text{Im } f(0°) \tag{2}$$

where k is the pion wave number. Relationships also exist (forward dispersion relations) between the total cross section and the real part of the forward scattering amplitude Re f(0°). These forward dispersion relations[3,4] allow the calculation of Re f(0°) in terms of an integration of Im f(0°) or the total cross section σ_{TOT} over all energies. They can be used with the difference in total cross sections $\Delta\sigma = (\sigma^{-}_{TOT} - \sigma^{+}_{TOT})$, where σ_{TOT} is the $\pi^{\pm}$-nucleus total cross sections, to determine an effective pion nucleus strong coupling constant.[5]

In principle, one of the "easiest" and most precise measurements is the total cross section. It is determined from a transmission or attenuation measurement of a beam of particles through a slab of the nuclei under study. When a new energy range becomes available at a new accelerator, total cross section measurements are among the first to be performed. In the past, this has been highly rewarding, leading to the detection of new resonances or new features of the interaction.

In general, measurements of the total cross section are less sensitive to some effects than would be the measurement of an appropriate partial cross section. However, the simplicity and high precision of total cross section measurements compensate for their lack of sensitivity.

Pion-Nucleon Total Cross Sections

One of the principal reasons for using the pion as a nuclear probe is the strength of the pion-nucleon interaction at energies

below 500 MeV. Below 100 MeV, the pion-nucleon (π-N) total cross section is considerably less than the nucleon-nucleon (N-N) total cross section which means that the π-nucleon interaction is weak and the pion de Broglie wavelength is large compared to the nuclear radius. Between 100 and 300 MeV, the π-N total cross section is dominated by the (3,3) resonance. Above 300 MeV, the π-N cross section is comparable to the N-N cross section which is steadily decreasing as the energy is increasing. At these energies, the pion wavelength is less than the nuclear radius.

The (3,3) resonance gives a large peak in the π-N total cross section occuring at approximately 180 MeV. The resonance derives its name from the fact that it occurs in the angular momentum $J = 3/2$, isospin $T = 3/2$ state. The peak for π^+p is nearly three times larger than the peak for π^-p. This is because π^+p is a pure $T = 3/2$ state while π^-p contains an admixture of the $T = 1/2$ state. The $J = 3/2$ means that this is principally p-wave scattering. From the assumption of charge independence and from isospin considerations, the total cross sections for π^+p (π^-p) and π^-n (π^+n) should be equal. This is of interest in the analysis of π-nucleus scattering.

A good discussion of the properties of the pion and of the pion-nucleon interaction may be found in the text by Lock and Measday.[6]

Pion-Nucleus Total Cross Sections

Prior to 1973, there was little data on π-nucleus total cross sections. Since then systematic data has become available at Rutherford Labs,[7] CERN,[8] BNL,[9] and at LAMPF.

The interest in pion-nucleus total cross sections comes from several sources. First there is the question of whether or not the (3,3) resonance continues to be present at all. Of more interest is the comparison of measured total cross sections to the theoretical optical model predictions. Because the pion-nucleus interaction is a many-body problem, attempts have been made to reduce it to a two-body problem via an optical model. An optical model replaces the various interactions by a single potential between the incident pion and the target nucleus. It contains both a real and an imaginary part to simulate both the elastic and reaction channels. Since an essential requirement of any optical model is that it be able to predict the total cross section, it follows that precise measurements of the total cross section as a function of energy and atomic number will be a stringent test of any optical model. These measurements can find classes of acceptable models and set limits on their energy range of applicability. Unfortunately, as will be seen later, there is some difficulty in this approach. The extraction of a total cross section from the raw data cannot be done in a model-independent way. A deviation from this standard approach has been proposed by M. Cooper and M. Johnson.[10] It is a model-independent analysis leading to an integrated cross section different from the standard total cross

section. This technique was not used in the present work and is mentioned only for completeness.

The large enhancement near resonance of π^+p (π^-n) over π^-p (π^+n) total cross sections suggests using the pion as a probe of the nucleon surface distribution in a nucleus. At the resonant energy, the mean free path of the pion in the nucleus is so small that it only interacts with the surface nucleons. Specifically, it should be possible to look for the neutron halo of neutron-rich nuclei using the proton distribution as determined from electron scattering.

Lastly, it is possible to find Re $f(0°)$ using a phenomenological model for the strong amplitude, valid for scattering angles inside the first minimum of the elastic differential cross section. Inputs for this analysis include the total cross section and elastic differential cross section data for both π^+ and π^-. The resulting Re $f(0°)$ can then be compared to forward dispersion relation calculations in an attempt to verify them experimentally.

There are several good review articles on the pion nucleus interaction such as those by Eisenberg,[11] Koltun,[12] Sternhiem and Silbar,[13] and Hüfner.[14]

Dissertation Experiment

The thrust of this experiment was twofold. The first was to measure the nuclear total cross section for both π^+ and π^- at low energies on a suitable target. Because of the Coulomb problems encountered at low energies, a low Z target, ^{4}He, was chosen. The

total cross sections were measured at pion laboratory kinetic energies of 51, 61, 75, 85, 95 and 105 MeV.

The $\pi^{\pm}$ - ^{4}He total cross sections of this experiment have been compared to the limited number of previous total cross section measurements for ^{4}He. The agreement was found to be reasonably good.

There has been a shortage of low energy data to compare to theoretical models, and the comparisons that have been made have shown extremely poor agreement. As will be discussed later, there has been a growing literature on the subject. The ^{4}He total cross sections of this experiment have been compared to several optical potential models for the π-nucleus interaction. These models contain adjustable parameters and the effect of changing these parameters on the agreement between data and models has been investigated in a limited way.

With the measured ^{4}He total cross sections of this experiment, the previously measured $\pi^{\pm}$ - ^{4}He elastic differential cross sections, and a phenomenological model for the nuclear elastic scattering amplitude, the real part of the forward nuclear elastic scattering amplitude was found at pion laboratory kinetic energies of 51, 60, 68 and 75 MeV. The results were then compared to two dispersion relation calculations of the real part of the forward amplitude as a function of the pion laboratory kinetic energy.

In addition to the ^{4}He cross sections, the nuclear total cross sections for π^{+} and π^{-} were measured for the isotope sets (^{12}C, ^{13}C), (^{16}O, ^{18}O), and (^{40}Ca, ^{44}Ca, ^{48}Ca, with natural Ti) at pion kinetic energies between 85 and 200 MeV and for 18 nuclei with $4 \leq A \leq 208$ at 85 MeV (A is the mass number).

The isotope measurements were made to look for the presence of a neutron halo in those isotopes which are neutron-rich. For the self-conjugate nucleus in each isotope set, presumably the neutron and proton distributions are the same. By comparing the total cross sections for π^+ and π^- on a neutron-rich nucleus and a self-conjugate nucleus in the same isotope set, the presence or absence of the neutron halo should be detectable. The measurements on the 18 nuclei at 85 MeV were made to look for the A-dependence of the total cross section at a fixed energy. The results of these measurements will be discussed elsewhere.

In Chapter II, the general principles of a total cross section measurement will be given while in Chapters III and IV the experimental layout and the data evaluation will be discussed. Chapter V will contain the experimental results, comparisons to theory, and the conclusions. The appendices will contain the details of some of the data correction calculations.

II. PRINCIPLES OF A TOTAL CROSS SECTION MEASUREMENT

Elements of an Ideal Measurement

The usual definition of the total cross section σ_{TOT} is that it is the sum of the total elastic cross section σ_{ne} and total inelastic cross section σ_r. In a measurement of the total cross section, one is measuring the cross section for all interactions to occur between the incident particle and the target nucleus. This is accomplished by measuring the flux of particles incident on the target and by measuring the flux of removed particles into 4π steradians or by measuring the flux of noninteracting particles at zero solid angle. The actual method used is closer to the latter.

Since the total cross section for the strong interaction between pions and nuclear matter is being sought, ideally a beam of π^0 should be used, so that the Coulomb interaction would be absent.

Since it is necessary to have detectors to measure the incoming and outgoing pions, they should be such that they are a hundred per cent efficient, do not disturb the beam, and are of infinitesimal dimensions on a macroscopic scale. In the geometrical limit, the beam should be a pencil beam. That is, it should have a negligible spatial extent perpendicular to the beam axis and the particles should have negligible momentum components in the directions perpendicular to the beam axis. This would eliminate geometrical effects which arise from the use of a beam with a finite size and finite divergence. This geometrical treatment of the beam is adequate if

the de Broglie wavelength of the incident pions is very small on a macroscopic scale as is the case in the energy range covered by this experiment. When the geometrical limit is no longer valid, the beam must be described by quantum mechanics (i.e., the particles in the beam are represented by wave packets of various shapes and sizes).

An experimental arrangement for measuring total cross sections is shown schematically in Figure 1. It consists of three elements. The first is a beam-defining counter, capable of detecting individual pions, to measure the incident flux. The second is a target containing a sufficient number of nuclei to obtain good statistical precision on the number of pions removed. It must also be sufficiently thin so that an incident pion interacts with at most one nucleus. The third is a counter after the target to detect the number of pions that did not undergo an interaction in the target.

The total cross section σ_{TOT} is then calculated as follows. If N_0 is the number of pions incident on the target and N is the number of pions which traverse the entire thickness of the target without having encountered any interaction, then they are related by

$$N = N_0 e^{-nt\sigma_{TOT}} \tag{3}$$

or

$$\sigma_{TOT} = -\frac{1}{nt} \ln \frac{N}{N_0} \tag{4}$$

where t is the target thickness in cm and n is the number of scattering nuclei/cm^3; $n = A/N_a\rho$ where A is the atomic mass of the target in g, N_a is Avogadro's number, and ρ is the target mass density in g/cm^3.

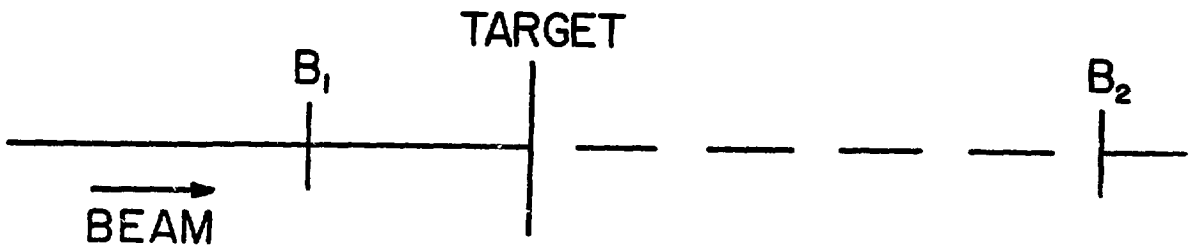

Figure 1. Schematic view of the experimental arrangement used to measure the total cross section. The counters B_1 and B_2 are used to detect the incident and unscattered pions, respectively.

In principle then, the measurement of the total cross section is determined by the attenuation of the pion beam in passing through the target of nt nuclei/cm^2.

Complexities of an Actual Measurement

In this section the complexities of an actual measurement will be discussed briefly, with the detailed discussion of these problems deferred until Chapter IV.

The most serious difficulty in performing a measurement of the total cross section is the inability of an experimenter to remove the effects of the Coulomb interaction through the use of a π^0 beam. This is because of the short mean lifetime (0.84×10^{-16} sec when at rest) of the π^0 before it decays, usually to two gamma rays. The charged pions, when at rest, have a much greater mean lifetime of 2.6×10^{-8} sec before they decay into a muon and a neutrino.

If λ is defined as the decay length in the laboratory, then λ is given by $\lambda = \frac{pc}{mc^2} c\tau$ where pc is the laboratory momentum in MeV, mc^2 is the pion rest energy in MeV, and $c\tau = 780.4$ cm is the mean life, in cm, of the pion at rest.

Table I compares λ for π^0 and $\pi^{\pm}$ at two laboratory kinetic energies. From Table I, it can be seen that only charged pions can be transported over sufficiently long distances to make them useful as strong interaction probes.

The use of $\pi^{\pm}$ beams means that the measured total cross sections are unavoidably composite cross sections (i.e., a mixture of the

Table I. Comparison of λ as a function of the laboratory kinetic energy T_π for π^0 and $\pi^\pm$.

T_π (MeV)	λ_{π^0} (cm)	$\lambda_{\pi^\pm}$ (cm)
50	2.34×10^{-6}	7.17×10^{2}
200	5.68×10^{-6}	1.73×10^{3}

Coulomb and strong interactions). The handling of these Coulomb effects will be discussed in Chapter IV.

As already mentioned, the pion is unstable and decays. The data need to be corrected for this effect since it is a false removal from the flux of incident pions. For example, in Figure 1 an unscattered pion, which decays before being detected by B_2, would be counted as a scattered pion should its decay muon not be detected by B_2. In general, the muon does not continue in the same direction as its parent pion.

The problem of the finite geometry of the detectors and the target, along with the finite size and divergence of real pion beams, can give erroneous removal cross sections. It is not possible to construct detectors for detecting the unscattered pions which subtend zero solid angle at the target. This means that real detectors will count pions that have been scattered at small angles. Thus the measured cross section is less than the "true" cross section. The finite thickness of both the target and the downstream detector create some uncertainty in the solid angle subtended by the detector.

The finite beam size and divergence make it possible for an unscattered pion to miss the detector, which makes the measured cross section too large. The above arguments are oversimplified since there is a replacement effect because of the finite cross sectional area of both the beam and target.

Another difficulty occurs because any detector placed in the beam will act as a target. This is most serious for the upstream beam-defining detector system (this system identifies pions and puts constraints on the beam divergence).

Furthermore, real detectors suffer from inefficiencies, absorption, and accidental counts. These must be accounted for to arrive at the number of pions which should have been detected by a detector.

Lastly, there is multiple Coulomb scattering which will be treated separately from the other Coulomb effects. This process is statistical in nature and results in particles being scattered at small angles. This undesirable effect can be reduced by decreasing the number of scattering centers in the target (i.e., by making the target thinner). Unfortunately, this decreases the number of pions which are scattered by the strong interaction, and some compromise must be reached.

Elements of an Actual Measurement

As in the last section, much of the following discussion will be treated in greater detail later. In this section the aim is to show

how a total cross section can be measured in view of the complexities discussed in the last section.

In the ideal experiment, the incident pions had to be detected individually to obtain the incident flux. In an actual experiment, this is, of course, still true, but with the further complication that the beam is contaminated with muons and electrons. Thus the beam-defining counters must have the capability of distinguishing between different species of charged particles.

In addition, the beam-defining counters, through their geometry, put constraints on the beam. The maximum acceptable divergence of the beam at the target can be fixed by the beam-defining counters. The spatial extent of the beam, perpendicular to the beam axis, is set by the pion channel magnets through which the pion beam comes.

A target cannot be made sufficiently thin that an incident pion interacts with at most one nucleus. Its thickness is chosen to minimize some of the effects discussed in the last section.

The detector, downstream of the target, cannot, of course, be made to subtend zero solid angle at the target, and, even if possible, it would not be desirable since a real pion beam is not a pencil beam. The problem is handled by the use of a circular counter which subtends a solid angle Ω at the target. A circular counter is used to match the roughly circular geometry of the beam.

An attenuation measurement is performed and a cross section is calculated using

$$\sigma(\Omega) = -\frac{1}{nt} \ln\left(\frac{N(\Omega)}{N_0}\right) \qquad (5)$$

This is different from equation (4) because the counter now subtends a solid angle Ω at the target and the number of particles it detects $N(\Omega)$ is a function of Ω. The cross section $\sigma(\Omega)$ is not the total cross section but rather the partial cross section for scattering outside of Ω. The counter is then moved to a new position subtending a new solid angle Ω', and the measurement is repeated yielding a new partial cross section $\sigma(\Omega')$. This is repeated for several solid angles, and an extrapolation to zero solid angle is made, yielding the total cross section.

An alternate procedure, shown schematically in Figure 2, is to use a series of circular coaxial counters of increasing radii so that several partial cross sections may be measured simultaneously. These counters are called transmission counters. Unlike the first method where each $\sigma(\Omega)$ was statistically independent, these $\sigma(\Omega)$ are statistically correlated. Each counter counts the same particles as the smaller counter in front of it plus a little extra. Because of the correlations, the extrapolation to zero solid angle must be done with care.

Data Analysis

In this section, the procedure will be discussed for extracting the strong interaction total cross section from a set of measured partial cross sections.

For each of the transmission counters T_t in Figure 2, a partial or removal cross section $\sigma(\Omega)$ is calculated from equation (5). This

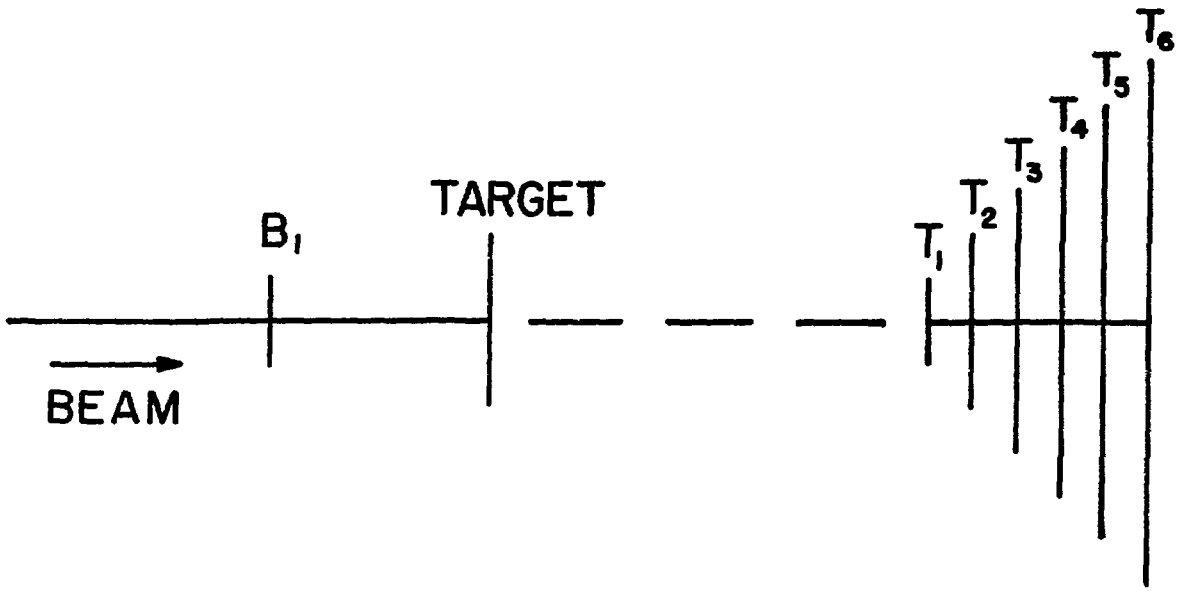

Figure 2. Schematic view of the experimental arrangement used to measure $\sigma(\Omega)$. The B_1 counter is used to detect the incident pions. The T_1 through T_5 counters are used to detect the scattered pions.

$\sigma(\Omega)$ contains many background effects which are handled to first order by comparison of target "in" and target "out" data runs. If T (B) denotes a target (blank) run, then from Allardyce et al.,[15]

$$N_B(\Omega) = N_{B0} \exp(-A) \tag{6}$$

$$N_T(\Omega) = N_{T0} \exp(-A) \exp(-nt\sigma(\Omega)) \ , \tag{7}$$

where A is a measure of the beam attenuation due to all effects which are independent of the target's presence such as absorption in the air and other materials surrounding the target and transmission counters. So $\sigma(\Omega)$ is then given by

$$\sigma(\Omega) = - \frac{1}{nt} \ln \left(\frac{\left(\frac{N_T(\Omega)}{N_{T0}} \right)}{\left(\frac{N_B(\Omega)}{N_{B0}} \right)} \right)$$

or

$$\sigma(\Omega) = \frac{1}{nt} \ln \left(\frac{R_0(\Omega)}{R(\Omega)} \right) \tag{8}$$

where $R(\Omega) = N_T(\Omega)/N_{T0}$ ($R_0(\Omega) = N_B(\Omega)/N_{B0}$) is the fraction of the beam detected by the transmission counter for the target "in" ("out" of) the beam. The partial cross section $\sigma(\Omega)$, $R(\Omega)$, and $R_0(\Omega)$ are written as functions of Ω since each counter subtends a different Ω at the target.

Now $\sigma(\Omega)$, as given in equation (8), still contains effects which are not necessarily the same for both the target and blank runs. These include the efficiencies of the transmission counters along with absorption and accidental coincidences in the counters. There are

also pion decay and multiple Coulomb scattering. All of these effects will be treated in detail in Chapter IV and the appendices.

After $\sigma(\Omega)$ is corrected for the above effects, there remains the question of what is the physical meaning of $\sigma(\Omega)$. The partial cross section $\sigma(\Omega)$, as seen by the i-th transmission counter, measures the cross section for scattering outside the solid angle Ω subtended by the counter at the target. This is

$$\sigma(\Omega) = \int_{\Omega}^{4\pi} \left(\frac{d\sigma}{d\Omega}\right)_{el} d\Omega + \left[\sigma_r - \int_{0}^{\Omega} \left(\frac{d\sigma}{d\Omega}\right)_{inel} d\Omega\right] \tag{9}$$

where $\left(\frac{d\sigma}{d\Omega}\right)_{el}$ is the elastic scattering differential cross section, σ_r is the total reaction cross section, and $\left(\frac{d\sigma}{d\Omega}\right)_{inel}$ is the differential cross section for all inelastic interactions. Now $\left(\frac{d\sigma}{d\Omega}\right)_{el}$ is given by

$$\left(\frac{d\sigma}{d\Omega}\right)_{el} = |f_c + f_n|^2$$

$$= |f_c|^2 + |f_n|^2 + 2\,\mathrm{Re}(f_c^* f_n) \quad , \tag{10}$$

where f_c and f_n are, respectively, the Coulomb and nuclear elastic scattering amplitudes. Also $\left(\frac{d\sigma}{d\Omega}\right)_{el}$ can be written as

$$\left(\frac{d\sigma}{d\Omega}\right)_{el} = \left(\frac{d\sigma}{d\Omega}\right)_{c} + \left(\frac{d\sigma}{d\Omega}\right)_{ne} + \left(\frac{d\sigma}{d\Omega}\right)_{cn} \tag{11}$$

where $\left(\frac{d\sigma}{d\Omega}\right)_{c}$, $\left(\frac{d\sigma}{d\Omega}\right)_{ne}$, and $\left(\frac{d\sigma}{d\Omega}\right)_{cn}$ are the Coulomb, nuclear elastic, and Coulomb-nuclear interference elastic scattering differential cross sections. From equations (10) and (11)

$$\left(\frac{d\sigma}{d\Omega}\right)_{c} = |f_c|^2 \tag{12}$$

$$\left(\frac{d\sigma}{d\Omega}\right)_{ne} = |f_n|^2 \quad , \tag{13}$$

and

$$\left(\frac{d\sigma}{d\Omega}\right)_{cn} = 2\,\mathrm{Re}(f_c^* f_n) \quad . \tag{14}$$

Starting with the definition of the total cross section $\sigma_{TOT} = \sigma_{ne} + \sigma_r$, one can write σ_{TOT} as

$$\sigma_{TOT} = \sigma_r + \int_0^{\Omega} \left(\frac{d\sigma}{d\Omega}\right)_{ne} + \int_{\Omega}^{4\pi} \left(\frac{d\sigma}{d\Omega}\right)_{ne} d\Omega \tag{15}$$

If an equation (15), $\int_{\Omega}^{4\pi} \left(\frac{d\sigma}{d\Omega}\right)_{ne} d\Omega$ is solved for and used along with equations (9) and (11), then $\sigma(\Omega)$ can be written as

$$\sigma(\Omega) = \sigma_{TOT} + \int_{\Omega}^{4\pi} \left(\left(\frac{d\sigma}{d\Omega}\right)_c + \left(\frac{d\sigma}{d\Omega}\right)_{cn} \right) d\Omega$$

$$\int_0^{\Omega} \left(\left(\frac{d\sigma}{d\Omega}\right)_{ne} + \left(\frac{d\sigma}{d\Omega}\right)_{inel} \right) d\Omega \tag{16}$$

or

$$\sigma_{TOT} = \sigma(\Omega) - \int_{\Omega}^{4\pi} \left(\left(\frac{d\sigma}{d\Omega}\right)_c + \left(\frac{d\sigma}{d\Omega}\right)_{cn} \right) d\Omega$$

$$+ \int_0^{\Omega} \left(\left(\frac{d\sigma}{d\Omega}\right)_{ne} + \left(\frac{d\sigma}{d\Omega}\right)_{inel} \right) d\Omega \quad . \tag{17}$$

The usual experimental procedure for obtaining the total cross section σ_{TOT} is to take the measured values of $\sigma(\Omega)$ for each transmission counter and to subtract the first integral on the right-hand side of equation (17). The resulting removal cross sections σ_{rm} are then fitted with a polynomial in Ω, usually linear or quadratic,

using the method of least squares. Sometimes the fit is a polynomial in t, the square of the momentum transfer for elastic scattering; $t = -2p^2(1 - \cos\theta)$ or $t = 1\frac{1}{\pi}p^2\Omega$, where p is the pion center-of-mass momentum and Ω is the center-of-mass scattering angle. An extrapolation to zero Ω or t is then made yielding the total cross section.

The justification for using a polynomial in t (or Ω) is presented by Giacomelli[16] and is based on the assumption that $\left(\frac{d\sigma}{d\Omega}\right)_{ne}$ and $\left(\frac{d\sigma}{d\Omega}\right)_{inel}$ are roughly exponential in t (or Ω) before the first minimum in $\left(\frac{d\sigma}{d\Omega}\right)_{ne}$. This is satisfactory since all of the measured $\sigma(\Omega)$ are at values of t inside the first minimum. Then after subtraction of the Coulomb and Coulomb-nuclear interference terms in equation (16), $\sigma(\Omega)$ is

$$\sigma(\Omega) = \sigma_{TOT} - \int_0^{\Omega}\left(\left(\frac{d\sigma}{d\Omega}\right)_{ne} + \left(\frac{d\sigma}{d\Omega}\right)_{inel}\right)d\Omega \qquad (18)$$

$$= \sigma_{TOT} - \int_0^{\Omega}[ae^{b\Omega} + ce^{d\Omega}]d\Omega$$

$$= \sigma_{TOT} - \left(\frac{a}{b}(e^{b\Omega} - 1) + \frac{c}{d}(e^{d\Omega} - 1)\right) \quad ,$$

where a, b, c, and d are constants. If the exponentials are expanded, then $\sigma(\Omega)$ becomes

$$\sigma(\Omega) = \sigma_{TOT} - (a + c)\Omega - \frac{a}{2}\left(b + \frac{cd}{a}\right)\Omega^2 + \cdots$$

or by renaming the constants

$$\sigma(\Omega) = A + B\Omega + c\Omega^2 + \cdots \qquad (19)$$

or equivalently

$$\sigma(t) = A + B't + C't^2 + \cdots \quad , \tag{20}$$

where $A = \sigma_{TOT}$. Thus the partial cross sections may be approximated by polynomials in Ω or t. To include higher-order terms in t, Allaby, et al.[17] fit the partial cross sections with $\sigma(t) = \exp(A + Bt + Ct^2)$ where $\sigma_{TOT} = \exp(A)$.

The procedure is thus, in principle, quite straightforward. However, because f_n is highly model-dependent, the resulting σ_{TOT} is also model-dependent. Now, even though the Coulomb-nuclear interference correction is model-dependent, it is principally a small-angle effect, typically for angles less than 10°. This is especially true for light nuclei (e.g., ^{4}He and ^{12}C) at energies near the (3,3) resonance. The interference correction increases as Z, the nuclear charge, increases and it also increases as T_π, the pion kinetic energy, decreases. For the large transmission counters subtending angles greater than 10°, this correction is typically 1.5% or less for ^{4}He for T_π in the range 100 to 250 MeV. Below 100 MeV, the interference correction begins to increase going from a 1% correction at 10° and 100 MeV to a 10% correction at 10° and 50 MeV. This correction is roughly model-independent and will be further discussed in Chapters IV and V.

Thus this typical analysis, when applied to the case of ^{4}He with small T_π, yields a σ_{TOT} that is fairly model-independent because Z is small. The model-dependent features contribute an uncertainty of ~±5%.

Finally, a practice which is sometimes adopted is to take a model and calculate the integral over $\left(\frac{d\sigma}{d\Omega}\right)_{ne}$ in equation (18). Then this is added to each partial cross section $\sigma(\Omega)$ before making the extrapolation to $\Omega = 0$. Because this integral goes to zero as Ω goes to zero, it does not affect the extrapolated cross section $\sigma(\Omega=0)$. However, it can serve as a smoothing function to allow the possible use of a lower-order polynomial in the least squares fit to the data.

III. EXPERIMENTAL DESIGN

LAMPF

The experiment was performed at the Clinton P. Anderson Meson Physics Facility (LAMPF) at the Los Alamos Scientific Laboratory. The heart of the facility is the 800 MeV proton linear accelerator with a design average intensity of 1 mA. A layout of LAMPF is shown in Figure 3. Figure 4 shows a detailed layout of Beam Area "A" which is the pion experimental area. For more information on the general facilities of LAMPF, a good reference is the LAMPF Users Handbook.[18]

Pion Beam

The Low Energy Pion Channel (LEP) was used as the source of the experimental pion beam. The channel and its characteristics are described in depth by Amato et al.[19] and Fulton[20] and in less detail in the LAMPF Users Handbook.[18]

The pions were produced at Target A-1 shown in Figure 4. The production target was 1 cm of aluminum, which was in the form of a rotating wheel to reduce local heating effects.

The LEP channel was designed to provide $\pi^{\pm}$ beams in the energy range ~20 MeV to 300 MeV. Thus it spans the energy range of the (3,3) resonance and extends down to low energies. The layout of the channel is shown in Figure 5. It consists of four rectangular bending magnets with two entrance and two exit quadrupole magnets. The

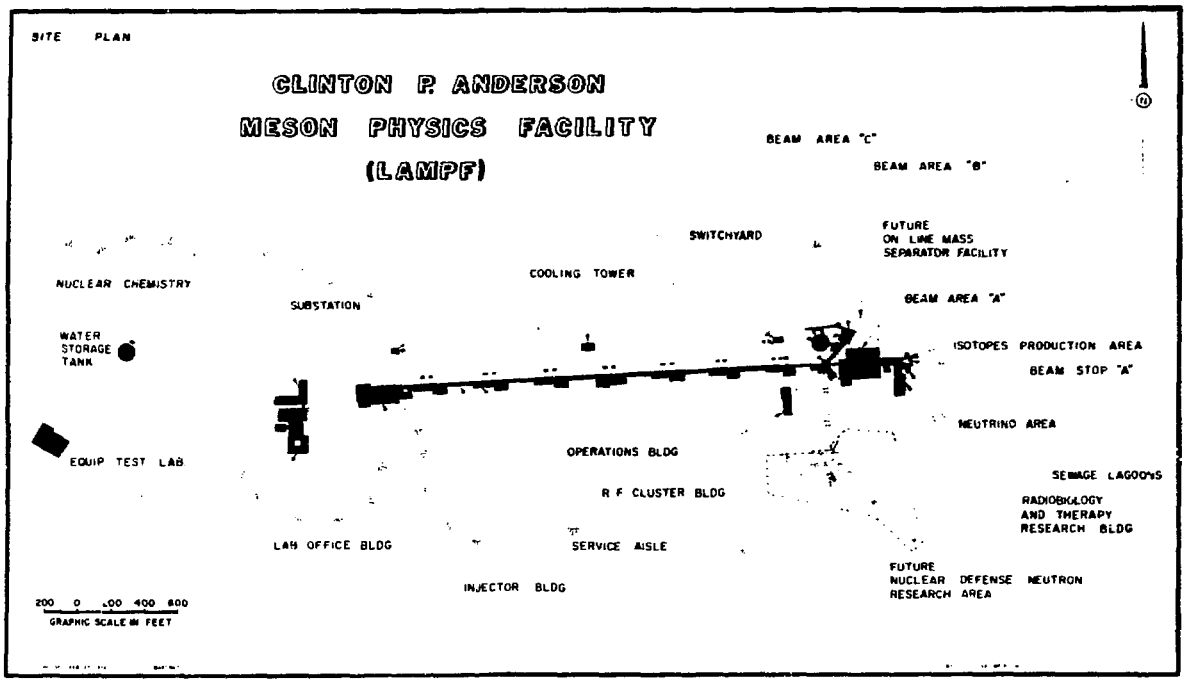

Figure 3. A layout of the Clinton P. Anderson Meson Physics Facility (LAMPF) (courtesy of the Los Alamos Scientific Laboratory).

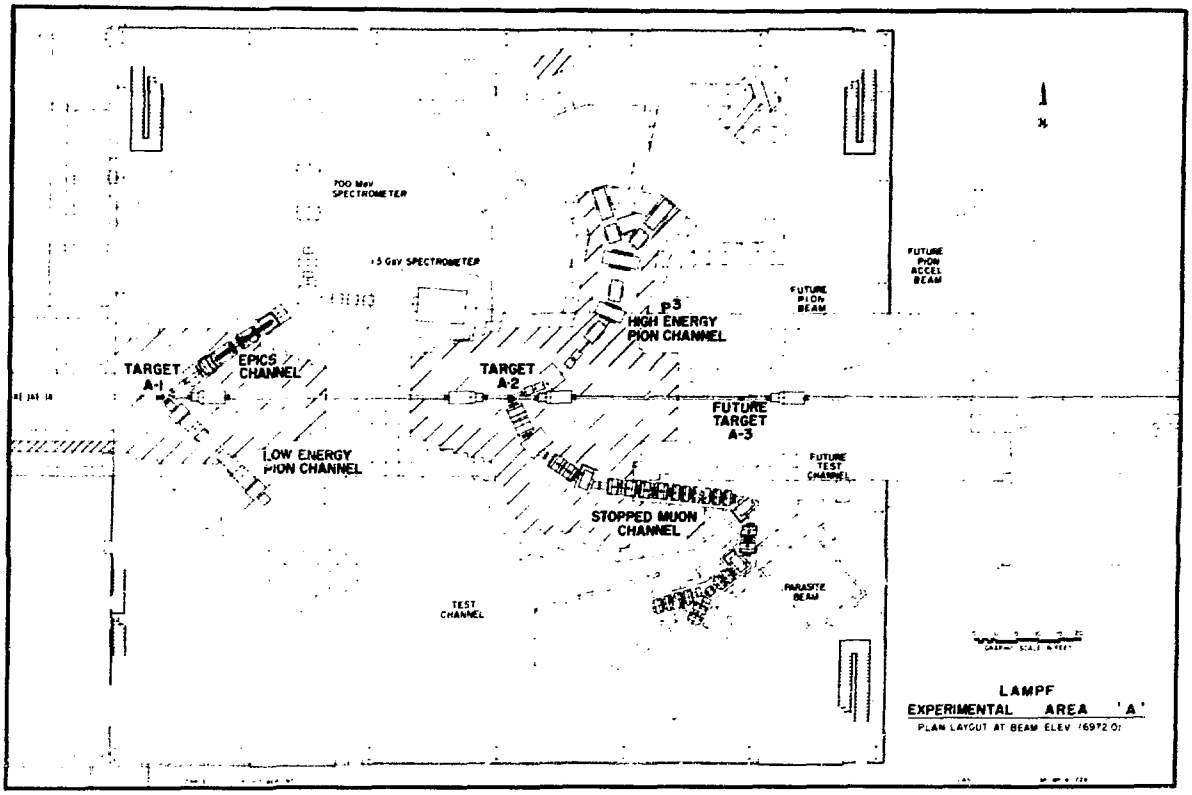

Figure 4. A layout of the pion experimental area, Beam Area "A," at LAMPF (courtesy of the Los Alamos Scientific Laboratory).

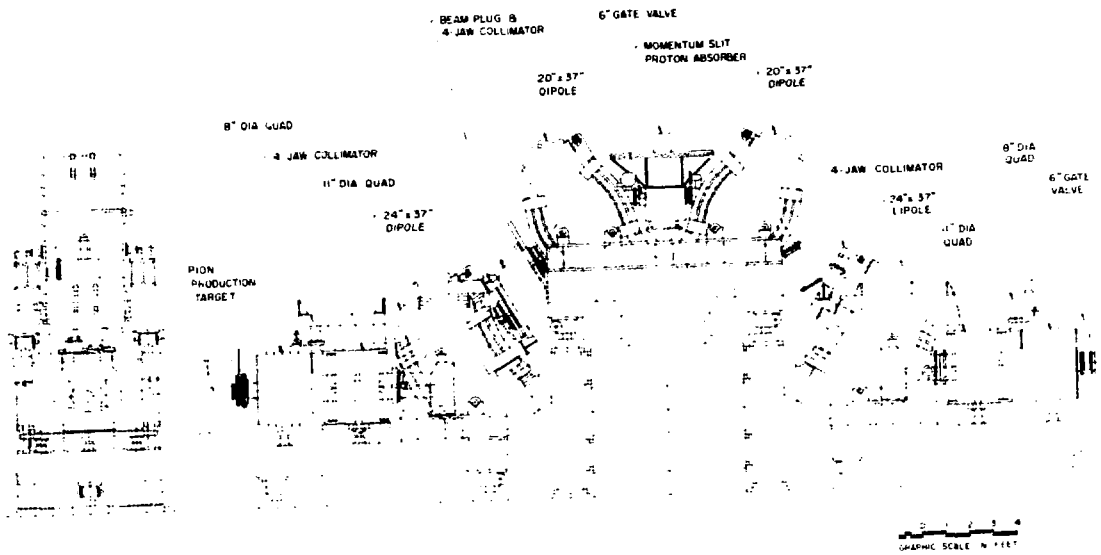

Figure 5. A layout of the Low Energy Pion channel (courtesy of the Los Alamos Scientific Laboratory).

bend plane of the channel is vertical to reduce the effect of the production target length on the momentum resolution of the channel. The channel is symmetric about a plane midway between the second and third bending magnets. Located at the symmetry plane are vertical slits which can be used to select the momentum bite $\Delta p/p$ desired at the channel exit. Immediately after the momentum slits is an absorber to remove protons from the π^+ beam. The flux of particles through the channel can be adjusted by four collimators and also by the momentum slit. The collimators determine the solid angle acceptance and emittance of the channel.

The channel is capable of providing both π^+ and π^- beams with a minimum resolution of $\Delta p/p = 0.05\%$. It is achromatic and isochronous, which means that the position and angle of the exit beam are independent of the momentum and that the channel preserves the 200 MHz pulsed time structure of the beam. The beam size and divergence at the exit can be varied by adjusting the exit quadrupoles. The length of the channel was kept short in design (14 m including a 0.62 m drift space after the last quadrupole) to minimize π decay at low energies.

The beam contamination consists of protons (for π^+), muons, and electrons. In addition, there is a neutron background. The protons, which come from the production target, have the same momentum but much lower energies than the positive pions and have a correspondingly higher stopping power. They were eliminated by an absorber at mid-channel which does not deteriorate the π^+ energy very much.

The neutrons are produced both in the channel and at the production target and come to the experimental area through the shielding.

The magnitude of the background they produce is measured in the accidentals, and, furthermore, their effect largely cancels out in the comparison of target "in" and "out" runs.

The muon contamination, coming from both the production target and from pions decaying at the end of the channel, and the electron contamination, coming from the production target, increase with decreasing energy. They were eliminated by either a time-of-flight system or a DISC Cherenkov counter, both of which will be described in detail in later sections.

Experimental Arrangement

An idealized view of the counter arrangement, for a typical data run, is shown in Figure 6. This shows the three essential elements of the experiment, namely the beam-defining counters, the target, and the transmission counters. The multiwire proportional chambers (MWPC) in the downstream position are part of the transmission counters. They could also be placed upstream between the halo counters and the DISC, where, as part of the beam-defining counters, they gave information on the beam profile at the target.

There was considerable versatility in the setup. The transmission stack and the MWPC box could be moved along a pair of rails on the support table. The MWPC could also be moved along a pair of rails mounted on the MWPC box. The target mechanism, second timing counter, and halo counters could be positioned on either side of the MWPC box. For those pion energies when the DISC was not in use, it

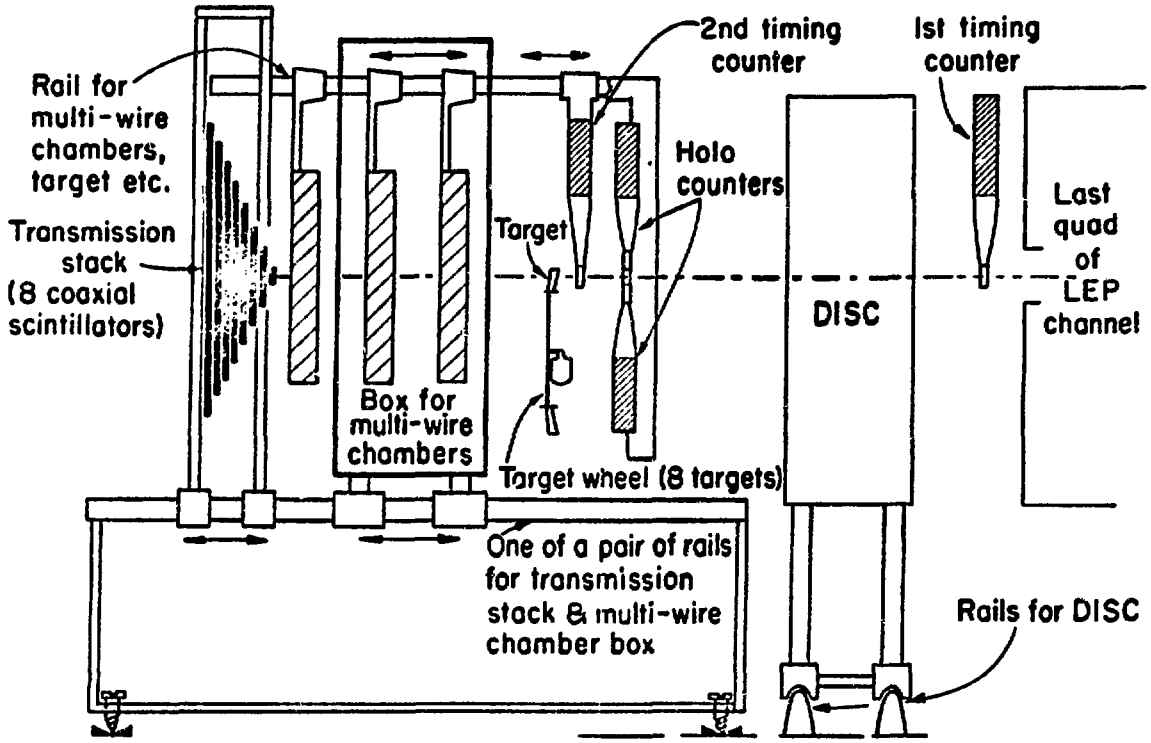

Figure 6. A schematic view of the counter arrangement used in this experiment.

could be rolled out of the beam on rails mounted to the floor.

Beam-defining counters. The beam-defining counters consisted of the two time-of-flight (TOF) counters, the DISC, and a pair of halo counters. When the ^{4}He target was used, a second set of halo counters were placed immediately after the DISC. A description of the TOF, DISC, and halo counters is given below, along with the purpose of each of them.

Time-of-flight. The time-of-flight system was designed, built, and tested by M. Cooper.[21] It consisted of two 1-cm thick Pilot-M (manufactured by Nuclear Enterprises) plastic scintillators. The light was collected by lucite light pipes which illuminated an Amperex 56AVP photomultiplier tube. In the ^{4}He data runs, the separation between the two TOF counters was 113 cm. The diameters of the scintillators were 5.08 cm and 2.54 cm for the first and second TOF counters, respectively (see Figure 6). The small diameters were used to limit the acceptable beam divergence to $\pm 2^\circ$. The diameter of the second TOF counter was less than or equal to the size of the target.

The purpose of the TOF counters was for particle identification (i.e., to remove the muon and electron background). They were used to discriminate against muons and electrons by measuring the time distribution (or spectrum) of particles in the beam, which corresponds to measuring the differences in flight times of the particles between the two counters. By suitably delaying the signal from the first TOF counter by an amount equal to the time-of-flight of the species of particle desired, clean particle identification was achieved. As

the energy of the particles increased, it became necessary to increase the distance between the counters to achieve particle identification. This was not necessary at those energies where the ^{4}He data was taken.

A second mode of operation for the TOF system utilized the 200 MHz rf structure of the proton beam together with the isochronous property of the LEP channel to gain an approximate 14 m of flight path. The timing was then done effectively between the A-1 production target and the second TOF counter, with a flight path of 14.7 m. This would not work at all energies. For muons and pions with a momentum of 195 MeV/c, for example, the flight time of muons over a 15 m path was shorter than the pion by almost exactly one rf period (5 ns). This caused the muon and pion peaks to coincide because of the repetitive nature of the rf signal.

By simultaneously doing timing between the first timing counter TOF1 and the second timing counter TOF2 and between the production target and TOF2, a two-dimensional TOF spectrum may be made. An example of such a spectrum, for 51 MeV π^-, is shown in Figure 7. In this figure, time-of-flight 1 represents time separation between particles covering the flight path (14.7 m) between the production target and TOF2. Time-of-flight 2 represents flight times between TOF1 and TOF2 with a flight path of 113 cm. The scale for both is 200 ps per channel. The major groups shown are: upper right, pions; lower right, electrons; and center left, muons from the production target. The pion, muon, and electron peaks are well separated.

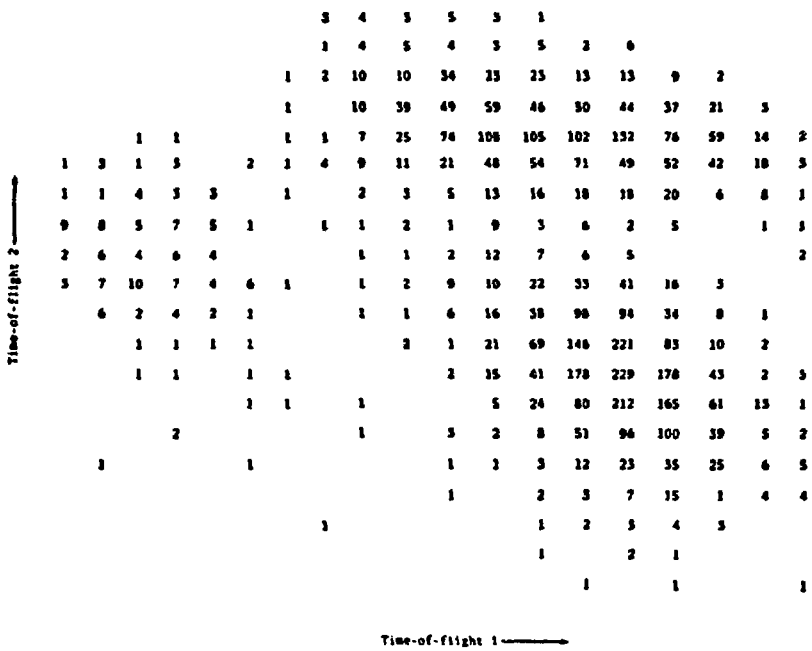

Figure 7. A sample two-dimensional TOF spectrum for 51 MeV π^- coming from LEP. Time of flight 1 represents time separations between particles covering the flight path (14.7 m) between the production target and TOF2. Time of flight 2 represents flight times between TOF1 and TOF2 with a flight path of 113 cm. The scale for both directions is 0.2 ns per channel. The major groups shown are: upper right, pions; lower right, electrons; and center left, muons from the production target

However, the simplest mode of operation of the TOF counters was in conjunction with the DISC. Here they were used to count any charged particle which fulfilled the geometry requirements they imposed on the beam (i.e., no time of flight constraint was imposed to select out a particular species of particle). To identify a pion a three-fold coincidence was required with the DISC and the two timing counters. Pion identification was done in this way for pion kinetic energies above 75 MeV. Below 75 MeV, the DISC would not count pions and the TOF system was used exclusively.

The time resolution of the TOF system was ±1/2 ns, allowing for a clean separation of pions, muons, and electrons. There was less than 1% contamination of muons and electrons. For more details on the capabilities of the TOF system, the paper by M. Cooper[21] should be consulted.

The beam-defining system was kept reasonably short to reduce the number of decays. TOF2 was smaller than the target so that all pions which passed through it would hit the target and miss any surrounding material (e.g., the target holders). However, because of the size of this counter, it was possible for pions to miss it and still hit the target. This could lead to undesirable effects, which were removed by the use of the halo counters. These effects and the halo counters are described in the next section.

Halo counters. The halo counters consisted of two barely overlapping Pilot-M plastic scintillators with an opening left in the center for the beam to pass through. The light from each scintillator was collected by lucite light pipes which illuminated an

EMI 9813B two-inch photomultiplier tube. The halo counters were positioned just upstream of TOF2 (see Figure 6).

As mentioned in the last section, TOF2 was smaller than the target. This made it possible for a pion to miss TOF2 and still hit the target. Such a pion could then scatter backwards into TOF2 and thus be counted as a beam particle. It would appear as a removed pion, since it would not be detected in the transmission stack, so that the measured partial cross sections would be systematically too large.

Another systematic error arises if there are two pions traveling together in time. Suppose one passes through TOF2 and the other does not. Further, suppose the tagged pion interacts in the target and is not detected by the transmission stack, while the untagged pion does not interact in the target and is detected by the stack. This would cause a scattered pion to be counted as an unscattered pion, so that the measured partial cross sections would be too small.

The above effects do not cancel in the comparison of blank and target data runs and must be compensated for in another way. The halo counters were designed to remove these effects by detecting those pions which miss TOF2 (i.e., they detect the beam halo). For example, whenever the DISC and the TOF system identified a particle as a pion, that event would be vetoed if a charged particle was detected at the same time by either of the halo counters.

The opening in the halo counters was centered about the beam axis; it was square and slightly smaller than TOF2. The square opening was used simply because of the ease in construction. The mismatch in geometry did not cause a significant change in count rate.

The shape of the beam was nearly circular, with a radius of 1 cm, so nearly all of the beam passed through the opening in the halo counters.

The halo scintillators had to be kept small, while, at the same time, they had to be large enough to mask the portion of the target extending radially beyond the edge of TOF2. It was necessary for the scintillators to be small because of a new effect created by their presence. It was now possible for a perfectly good pion, identified by the DISC and TOF, to interact in the target and scatter backwards. If the pion hit the halo counters, the event would be vetoed. The measured partial cross sections would be too small because "true" scattered pions would be discarded. To reduce this effect, the halos were made small and placed 152.4 mm upstream from the target to reduce the solid angle they subtended at the target. TOF2 was placed 101.6 mm downstream from the halos. This kept it close to the target in order to minimize the number of tagged pions that decayed between it and the target. It also kept small the solid angle subtended by TOF2 at the target, which reduced the number of backward scattered pions going into TOF2. This type of event could be misconstrued as a new beam pion. This fictitious pion would be recorded as a scattered pion and would lead to the partial cross sections being too large. Lastly, the separation between the halo counters and TOF2 was small enough to prevent a pion with a large divergence from not being detected by either one. Chapter IV contains a discussion of how these effects were tested for.

In the special case of the ^{4}He target, a second set of halo counters was needed since the spatial extent of the ^{4}He target was too large for the original halo counters to mask it. This set was placed as far upstream as possible (i.e., immediately downstream of the DISC).

The halo counters were mounted vertically and scaled separately. A significant increase in counting rate for either counter would indicate a drifting of the beam caused by a drifting of the fields of the bending magnets.

DISC. In addition to the TOF system, a DISC Cherenkov counter was used for particle identification. DISC is an acronym for Differential Isochronous Self-Collimating Cherenkov counter. The general principles of operation will be reviewed below. More detailed information on the design considerations may be found in the papers by Meunier[22] and by Leontic and Teiger.[23] The original design for the DISC used at LAMPF was due to Leontic and Teiger. However, modifications were required for use on the LEP channel.

All Cherenkov counters use the property that whenever a charged particle passes through an optical medium with velocity v, which is greater than that of light in the medium, light is emitted at an angle θ with respect to the particle's trajectory. The angle θ is given by $\cos\theta = 1/n\beta$, where n is the index of refraction of the medium and $\beta = v/c$, where c is the velocity of light in vacuum.

Thus, if a light detection system is built which is sensitive to the angle θ at which the light is emitted, then the detector is able to distinguish between particles with different velocities. In

particular, for beams of particles having the same momentum, it will be able to distinguish between different types of particles, since their masses are different. Since these counters depend on good velocity and angular resolution, they are ideally suited for particle beams with good angular, spatial, and momentum resolution such as the LEP channel.

Now a typical differential Cherenkov counter works as follows. A flat radiator (i.e., a material in which Cherenkov light can be produced) is placed in a beam with its face perpendicular to the beam axis. Cherenkov light is emitted in the radiator in a cone characterized by an angle θ, and the light will emerge at an angle θ', where $\sin\theta' = n \sin\theta$, and n is the index of refraction of the radiator. If this light is collected with a spherical mirror whose optical axis coincides with the beam axis, it will form a ring image in the focal plane of the mirror. The radius of the ring will depend on the velocity β of the particle, and the position of the center of the ring will depend on the angle of the particle's trajectory with respect to the beam axis. Both are independent of the displacement of the particle's trajectory from the beam axis. In a DISC counter the ring is detected by a bank of photomultiplier tubes.

In the design of a differential Cherenkov counter, several problems have to be overcome. One arises from effects which introduce a spread $\Delta\theta$ in the Cherenkov angle θ. This results in a loss of efficiency due to light missing the photomultiplier tubes and a loss in velocity resolution, given by the expression $\frac{\Delta\beta}{\beta} = \Delta\theta(n^2\beta^2 - 1)^{1/2}$

or $\Delta\beta/\beta = \tan\theta\,\Delta\theta$. To find conditions for distinguishing between pions and muons, let $\Delta\beta/\beta = (\beta_\mu - \beta_\pi)/\beta_\pi$ where β_π and β_μ are the pion and muon velocities. This condition puts constraints on the maximum acceptable magnitude of $\Delta\theta$, since if $\Delta\theta$ should exceed this the counter's ability to distinguish these particles could be diminished or even destroyed. Now, contributions to the angular spread $\Delta\theta$ come from multiple scattering in the radiator, beam divergence, momentum spread of the beam, and optical aberrations. Neglecting the latter, which can be corrected for, one has $\Delta\theta = [(\Delta\theta)_s^2 + (\Delta\theta_B)^2 + (\Delta\theta_{\Delta p})^2]^{1/2}$ where $\Delta\theta_s$ is the contribution due to multiple scattering, $\Delta\theta_B$ is that due to beam divergence, and $\Delta\theta_{\Delta p}$ is that due to momentum spread.

The optical aberrations fall into three classes. There are geometrical aberrations in the optical system, variations in the angle of the Cherenkov light due to dispersion in the radiator, and absorption of the UV portion of the Cherenkov spectrum by elements in the optical system.

If $\Delta\theta'$ is the angular width of the photomultiplier tube aperture and $\Delta\theta$ the angular width of the ring image, there is a loss of efficiency when $\Delta\theta' < \Delta\theta$. A particle passing through the radiator with a large angular divergence, or far off the central momentum, or experiencing large multiple scattering will usually not produce a Cherenkov light cone detectable by the phototubes and will be rejected by the counter. This illustrates the self-collimating feature of the DISC. It should be noted that if $\Delta\theta$ is too large, it becomes possible for the light cones of different particle species

to overlap. By making the aperture $\Delta\theta'$ small, it is still possible to get a pure signal but with reduced efficiency.

Another consideration in the design of these counters is the electronic efficiency. If the average number of photoelectrons detectable by all phototubes is $\bar{n}$ and if the electronics is capable of detecting single photoelectrons, then the efficiency ε for a q-fold coincidence arrangement of the phototubes is

$$\varepsilon(q) = (1 - \exp(-\frac{\bar{n}}{q}))^q \quad .$$

It is important for good efficiency that $\bar{n}$ be fairly large. Since $\bar{n}$ is proportional to the radiator thickness ℓ, increasing ℓ increases $\bar{n}$. Unfortunately the multiple scattering increases as $(\ell/\ell_{rad})^{1/2}$, where ℓ_{rad} is the radiation length of the radiator. Therefore, the actual ℓ used is a compromise.

The basic design for the DISC is shown schematically in Figure 8. There were two coaxial circular ports in the center of the counter for the beam entrance and exit. All elements of the counter were coaxial about a line through the center of these ports. When placed in a beam, this line, which defines the optical axis, was made to coincide with the beam axis.

The cell indicated in Figure 8 contained a liquid radiator. Its entrance window was 0.38 mm of Al and its exit window was 2.54 mm of Vycor (quartz). The cell diameter was 12.7 cm, which defined the maximum sensitive region of the DISC. It was mounted in a holder which could be moved along the optical axis by an electrical stepping

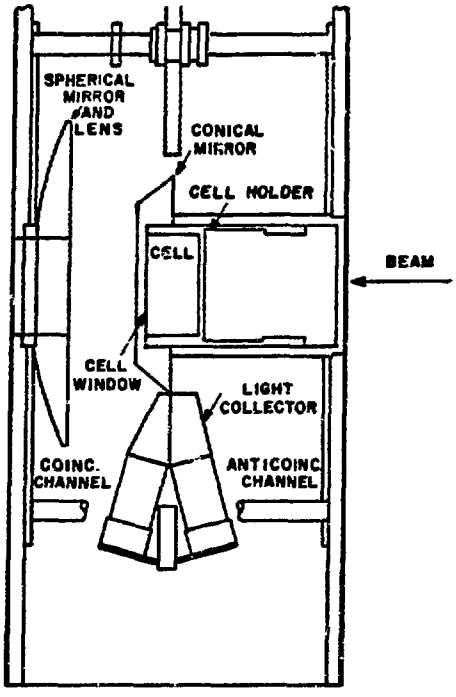

Figure 8. A schematic view of the DISC. The cell contained the liquid radiator. The Cherenkov light from the radiator was collected by the spherical mirror and lens system, focussed on the conical mirror, and detected by the coincidence or anticoincidence channels. The figure was adapted from Ref. 23.

motor. Some of the characteristics of the different liquid radiators used in the DISC are given in Table II. These include the index of refraction, density, radiation length, and thickness. For each radiator there was a characteristic pion velocity range $\Delta\beta_\pi$ for which the DISC would detect pions. This, along with the corresponding kinetic energy range ΔT_π and momentum range ΔP_π, is given in Table II. Muons from the production target have $p_\mu = p_\pi$ and $\Delta p_\mu = \Delta p_\pi$. The velocity range $\Delta\beta_\mu$, corresponding to Δp_π, is also listed. The radiator for each energy range ΔT_π was chosen so that the Cherenkov light, for pions with energies covered by ΔT_π, would be detectable by the DISC's optical system.

The Cherenkov light from particles passing through the radiator formed a ring in the focal plane of the spherical mirror and lens system. The lens was made of lucite and used to correct for dispersion in the radiator. The diameter of the ring was dependent on the particle velocities. To facilitate light collection by the detection system, a conical mirror was employed which projected the focused light rings onto an imaginary cylindrical surface. Therefore by moving the detection system along the optical axis, it can be brought into the position required for a given velocity response of the counter. This light detection system consisted of two groups of nine phototubes (two-inch EMI 9813B photomultiplier tubes). Each tube was connected to a light guide which was mounted on a plate. The detector formed a circle centered about the optical axis and could be moved by a stepping motor along the optical axis.

Table II. Characteristics of the liquid radiators used in the DISC. These include the index of refraction n, the density ρ, the radiation length ℓ_{rad}, and the thickness ℓ. Also given are the pion kinetic energy range ΔT_π, momentum range Δp_π, and velocity range $\Delta\beta_\pi$ in which each radiator was used. Lastly, the muon velocity range $\Delta\beta_\mu$ for muons with $\Delta p_\mu = \Delta p_\pi$ (i.e., these are muons from the production target with $p_\mu = p_\pi$) is listed.

Radiator Material	n	ρ(g/cm^3)	ℓ_{rad}(cm)	ℓ(cm)	ΔT_π(MeV)	ΔP_π(MeV)	$\Delta\beta_\pi$	$\Delta\beta_\mu$
CS_2	1.630	1.266	18.6	2.03	60-75	140-160	0.715-0.760	0.800-0.836
CS_2 & Isopropanol (C_3H_7OH)	1.550	1.188	39.2	2.03	75-90	160-180	0.755-0.795	0.836-0.864
Decahydronapthalene ($C_{10}H_{18}$)	1.476	0.887	52.0	2.03	90-120	180-220	0.790-0.840	0.864-0.902
2,2,4 Trimethylpentane (C_8H_{18})	1.392	0.692	70.7	2.08	115-160	215-265	0.835-0.885	0.899-0.930
Methanol (CH_3OH)	1.331	0.796	54.2	2.08	150-240	255-350	0.875-0.930	0.925-0.958
2,2,2 Trifluroethanol ($C_2F_3OH_3$)	1.291	1.382	25.8	2.10	190-360	300-480	0.905-0.960	0.944-0.977
Freon C-51-12 (C_6F_{12})	1.256	1.672	20.6	2.10	240-670	350-800	0.930-0.985	0.958-0.991

The upstream (downstream) detector group was the anticoincidence (coincidence) ring (see Figure 8). The coincidence ring of phototubes was set to detect Cherenkov light from pions with the proper velocity. Cherenkov light from particles with larger velocities (such as muons) and/or outside the angular acceptance of the DISC (i.e., particles with too great a divergence) was detected by the anticoincidence ring. Any signal from the coincidence ring was vetoed if there was a signal from the anticoincidence ring. To avoid a blind region between the two phototube rings, the two sets of light guides were placed one flush with the other. The opening aperture for the coincidence ring light guides was 1.5 cm which allowed for a maximum beam divergence of approximately ±34.

The logic diagram for the DISC is shown in Figure 9. The nine phototubes in the coincidence ring were broken into three groups of three. The signals for the three tubes in each group were added together, with the combined signal going to a discriminator. The output then went to a coincidence unit where a two-out-of-three coincidence logic identified a pion. The nine anticoincidence tubes were all added together and sent to a discriminator. The output went to the coincidence unit as a veto. The output from the coincidence unit was then required in a two-fold coincidence with a signal from the TOF counters to identify a pion onto the target.

To insure that the DISC worked properly, several tests were made. The first one was to produce a curve similar to the one in Figure 10, which was made by Leontic and Teiger[23] when they tested their DISC in a kaon beam. For these tests, their DISC was placed in a beam

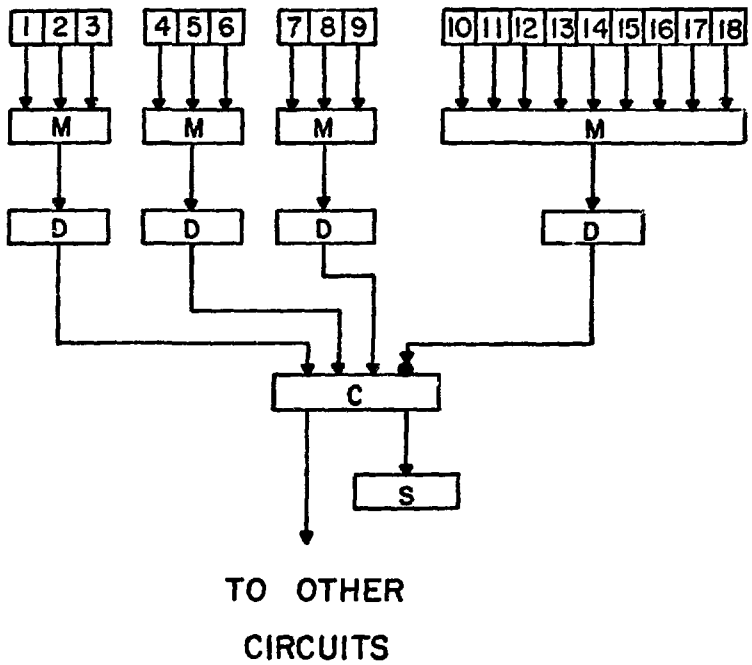

Figure 9. Fast logic diagram for the DISC. The numerals 1 through 9 and 10 through 18 refer to the phototubes in the coincidence and anticoincidence channels, respectively. M, D, C, and S stand for dc mixer, discriminator, coincidence unit, and scalar, respectively.

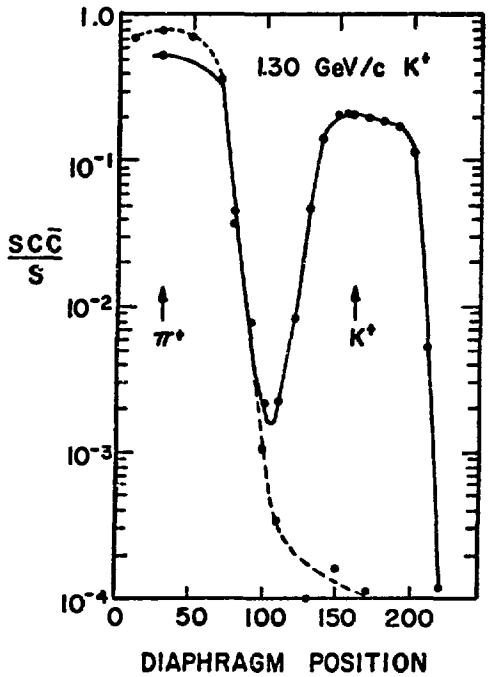

Figure 10. Performance curve for the DISC used in Ref. 23. It shows the π^+ and K^+ peaks as a function of the position of the coincidence channel when their DISC was placed in a 1.30 GeV/c K^+ beam. The curve is described in detail in the text.

along with a scintillation counter telescope S. The number of counts in S and the number of coincidences $S \cdot C \cdot \overline{C}$ were scaled where C and $\overline{C}$ are signals from the coincidence and anticoincidence rings, respectively. Then the ratio $S \cdot C \cdot \overline{C}/S$ was plotted versus the position of the phototube ring (in arbitrary units). The result shows two peaks, due to π^+ and K^+. It should be noted that their coincidence ring was also split into three groups of three tubes each. The signal C was the result of a three-fold coincidence between the three groups.

A similar curve, produced by placing the LAMPF DISC in the LEP channel pion beam, is shown in Figure 11. The test was made for 100 MeV π^+. The number of TOF•DISC coincidences, normalized to the number of TOF counts, was plotted versus phototube ring position in arbitrary units. Note that the TOF counters were not used in their time-of-flight mode. For this test, a three-fold coincidence was required between the three groups of tubes in the coincidence ring. No muon peak was seen, as expected. From Table II, it can be seen that at 100 MeV $\Delta\beta_\pi$ and $\Delta\beta_\mu$ do not overlap and so there should be no muon peak. This was still true at 200 MeV, which was the highest energy at which the DISC was operated.

In addition to the muons from the production target, there are muons from pions decaying after the last bending magnet. Because of the TOF geometry, only backward or forward decay muons could be mistaken for pions. In Table III, the minimum and maximum velocity of the decay muon (corresponding to backward and forward) is given for different pion velocities. The probability that they could be identified as pions is small.

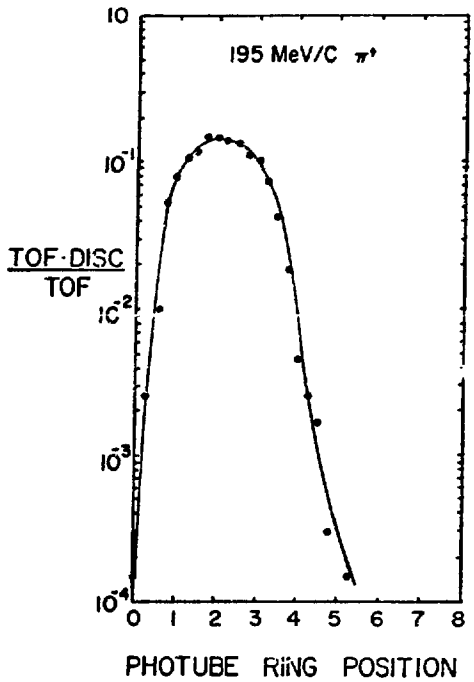

Figure 11 Performance curve for the DISC used in this experiment. It shows the π^+ peak as a function of the position of the coincidence channel. The curve is described in detail in the text.

Table III. Kinematics for π decay ($\pi \rightarrow \mu$). T_π and β_π are the pion kinetic energy and velocity. β_μ is the muon velocity for $p_\mu = p_\pi$ where p_π and p_μ are the pion and muon momentums. T_μ (min) (T_μ (max)) and β_μ (min) (β_μ (max)) are the minimum (maximum) kinetic energy and velocity of the decay muon. All the energies are in MeV.

T_π	β_π	β_μ	T_μ(min)	β_μ(min)	T_μ(max)	β_μ(max)
50	0.677	0.772	17	0.49	71	0.80
100	0.813	0.879	41	0.69	124	0.89
150	0.876	0.923	68	0.80	175	0.93
200	0.912	0.946	95	0.85	227	0.95
250	0.934	0.960	123	0.89	278	0.96
300	0.948	0.969	150	0.91	329	0.97

Electrons, at the energies in Table II, have velocities of $\beta \simeq 1$. Therefore they are not detectable by the DISC. At two energies, 90 and 150 MeV, the TOF counters were set to measure time-of-flight. When the DISC was put into coincidence with the TOF system, the electron and muon peaks disappeared from the time spectrum.

At each energy where the DISC was used a curve such as that in Figure 11 had to be made. For the data run the phototube ring would be positioned on the peak of the curve. However, instead of a three-fold coincidence from the coincidence ring, a two-out-of-three coincidence was used. The effect of this on the curve in Figure 11 was to increase the counting rate on the peak by a factor of three.

The increased counting rate is attributed to the low intensity of the Cherenkov light.

Multiwire proportional chambers. A brief description of the MWPC will be given below. For a general discussion on the design and performance of MWPC, the papers by Charpak[24,25,26] are a good source.

A MWPC is a position-sensitive detector having good spatial resolution (it is essentially an ionization chamber), capable of handling high counting rates. It also has the desirable property of presenting a small amount of mass to a particle passing through it.

Three MWPC were used in this experiment and are shown in their downstream position in Figure 6. When used to measure the beam intensity profile, they were placed between TOF2 and the DISC. In either position, they were centered about and perpendicular to the beam axis.

All three MWPC were identical. The structure of each was like a sandwich with a 6.35 mm spacing between each parallel layer. First there was the entrance window, consisting of 0.05 mm of mylar, then a high-voltage plane, a signal plane, another high-voltage plane, another signal plane, another high voltage plane, and finally the exit window consisting of 0.05 mm of mylar. There was a constant flow of gas throughout the interior of the chamber.

The high-voltage planes consisted of sheets of 0.05 mm mylar aluminized on both sides. A signal plane consisted of a plane of independent wires with a 2 mm spacing. The wires were 0.02 mm

diameter gold-plated tungsten. A constant potential difference of 4300 to 4500 volts was maintained between the high-voltage and signal planes, with the signal planes at ground. The negative high voltage for each chamber was different. The wires in one signal plane were perpendicular to the wires in the other signal plane, so that the wires of the two signal planes, along with the beam axis, formed a rectangular coordinate system. There were 128 vertical wires and 196 horizontal wires in each chamber, which determined the x and y positions of the particle. The spatial resolution of each MWPC was ±1 mm, which was equal to half the wire spacing.

The gas flowing through the MWPC was a mixture of 67% argon, 0.4% freon, 33% isobutane, and a small amount of propanol. The purpose of the mixture of argon, freon, and isobutane was for amplification of the signal. The propanol was for quenching. Gases for MWPC's are discussed in more detail in the papers by Charpak.[24,25,26] Each wire had its own amplifier for further amplification of the signal.

By knowing the x and y coordinates of the pion in each chamber and the z coordinates of the x and y signal planes in each chamber ($z = 0$ is the center of the target), it was possible to fit a straight line in space to the three x coordinates and another one to the three y coordinates. The two straight lines were extrapolated to the target (i.e., to $z = 0$) to give the pion's x and y coordinates there. The slopes of the two straight lines also tell the pion's divergence in both the xz and yz planes. In this way, when the wire

chambers were in their upstream position, they measured the beam profile at the target. The beam profile was found to be roughly gaussian in x and y and in the divergence of the beam in the xz and yz planes.

If more than one x or y wire fired in a chamber then the pion's x or y coordinate was taken from the centroid of the group of wires. Multiple wire firings were accepted up to and including eight wires. If more than eight fired the event was rejected.

Only a small subset of the good events in the chambers was ever recorded. These events were any for which the pion missed counter T_2 in the transmission stack. This criterion was used whether the wire chambers were upstream or downstream of the target. A pion was considered to be a beam or a scattered pion if it missed T_2.

Targets. For completeness, all of the targets used in the total cross section measurements are described here. However, only for the ^{4}He target will a detailed description be given. The results for the other targets will be reported elsewhere.

Solid and liquid targets. In all, there were 17 targets. They are listed in Table IV, along with their thicknesses in g/cm^3. They were all solid, with the exception of the $H_2{}^{16}O$ and the $H_2{}^{18}O$, which were liquids.

All targets were in the form of disks with diameters from 3.175 to 4.445 cm. Because the beam spot on the target was not of uniform distribution, it was important to know the uniformity of the target density. Radiographs were made of the targets, and the densities

Table IV. Targets and target thicknesses. Each target thickness t is in g/cm^3.

Target	t	Target	t	Target	t
Al	1.936	^{48}Ca	1.5561	^{6}Li	0.8944
^{10}B	2.01	CD_2	0.9981	^{7}Li	1.070
^{12}C	0.9321	CH_2	0.8481	Pb	0.297
^{13}C	0.720	Cu	1.776	Sn	1.430
^{40}Ca	1.5113	$H_2{}^{16}O$	0.922	Ti	1.7465
^{44}Ca	1.4591	$H_2{}^{18}O$	1.025		

were found to be uniform to better than 0.1%. A radiograph was made by measuring the transmission of gamma rays through the target material.

The targets were mounted in holders which in turn were mounted on a target wheel along with blanks for target "out" runs, which were identical to the real target except for the absence of the target material. A target wheel could hold a maximum of 8 targets or blanks and could be rotated by remote control to change a target or blank. It was positioned 5.08 cm downstream from TOF2, as shown in Figure 6.

^{4}He target. For measuring the total cross section of $\pi^{\pm}$ on ^{4}He, a thin-walled superfluid ^{4}He target was used. The target was built and tested by H.O. Meyer.[27]

The principal difficulty in designing a ^{4}He target is in knowing accurately the absolute thickness of the target. This is essential in making a precise measurement of the total cross section. This is easily seen from equation (8), which shows the measured partial cross section $\sigma(\Omega)$ to be inversely proportional to the target thickness t.

To achieve this, a cryogenic target was used which was capable of cooling liquid ^{4}He below the λ point (2.19°K) where it makes the phase transition to a superfluid. In the superfluid phase, ^{4}He excludes the formation of small bubbles in the target volume, so that its density can be determined to better than ±0.1% by a rough measurement of the vapor pressure (±1 mm Hg). This is because near the λ point the density is a slowly-varying function of the vapor pressure.

A second uncertainty in the target thickness arises from deformation under pressure of the thin entrance and exit windows, which define the target surface. This uncertainty can be made small by having a cylindrical target whose axis of symmetry is perpendicular to the beam axis, so that the windows form the surface of a cylinder. Meyer[27] determined that, under operating conditions, the stretching of the Kapton windows introduced an uncertainty in the target thickness of less than 0.1%.

On the other hand, a cylindrical target geometry requires knowledge of the intensity distribution of the incident beam over the target. This intensity profile was measured with the MWPC as described above.

A schematic view of the target is shown in Figure 12. The three major elements are the vacuum vessel (4), a liquid nitrogen radiation shield (5), and a ^{4}He vessel (6). The He vapor pressure was monitored with an accuracy of ±0.3 mm Hg.

The target cell is shown in Figure 13. It contains two identically-shaped cavities. The upper one is the target cell, containing the ^{4}He, and the lower one is the dummy target for blank runs. The dummy target is evacuated together with the main vacuum container. The entrance and exit windows consisted of 18 mg/cm^2 Kapton ($C_{22}H_{10}N_2O_5$). The target diameter was 7.6 cm at room temperature.

In order to optically align the cylindrical target with respect to the beam axis, a 0.15 mm diameter steel wire was strung along the central axis of the target cell. It is shown in Figure 13.

During a data run, the ^{4}He target was placed at the position of the target wheel as shown in Figure 6. It was suspended from above by a hoist and was raised and lowered for target "in" and "out" runs. The target could be used for more than 30 hours before being refilled.

Table V gives the target thickness in mg/cm^3 at the λ point as a function of the lateral displacement S from the beam axis. The direction of S is perpendicular to both the beam and the target axis. These thicknesses were folded with the beam profile to calculate the effective target thickness. It was found to be 1085 mg/cm^3 with a systematic error of 0.5%. The details of this calculation will be discussed in Chapter 4.

Transmission detectors. After passing through the target, the transmitted beam was detected by the wire chambers (if placed

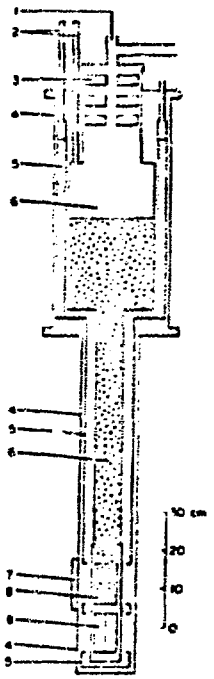

Figure 12. Dewar and target system. As seen in the beam direction the elements are: (1) filling and pumping post for helium volume; (2) vents; (3) radiation shield; (4) outer vacuum container; (5) liquid-nitrogen shield; (6) helium container; (7) side viewport; (8) target cell; (9) dummy target cell. The figure is from Ref. 27.

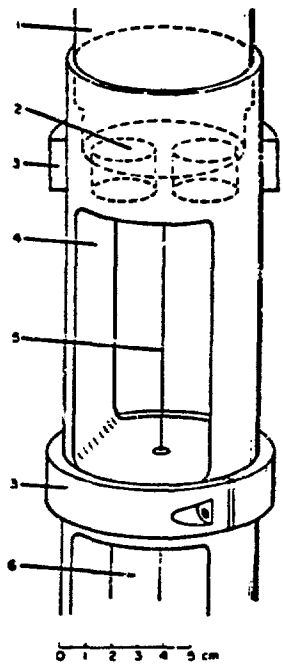

Figure 13. Target cell. The elements are: (1) stainless-steel tube; (2) filling holes; (3) aluminum clamps; (4) side strut of brass target cell; (5) central wire for alignment of target; (6) dummy target cell. The figure is from Ref. 27.

Table V. ^{4}He target thickness t as a function of the displacement S. The direction of S is perpendicular to the beam axis and the target axis.

S(cm)	t(mg/cm^2)	S(cm)	t(mg/cm^2)
0.0	1101.4	1.1	1054.2
0.1	1101.0	1.2	1045.0
0.2	1099.8	1.3	1034.8
0.3	1097.9	1.4	1023.9
0.4	1095.2	1.5	1011.9
0.5	1091.7	1.6	998.99
0.6	1087.5	1.7	985.01
0.7	1082.5	1.8	967.97
0.8	1076.7	1.9	953.82
0.9	1070.0	2.0	936.48
1.0	1062.5		

downstream) and the transmission stack. The wire chambers and transmission stack served as two independent systems for measuring the beam attenuation.

Transmission stack. The transmission stack was the last set of counters encountered by the beam in the counter arrangement shown in Figure 6. The stack consisted of 9 circular coaxial plastic Pilot-M scintillators centered about the beam axis. It could be moved along the beam line.

The counters were labeled sequentially T_1, T_2, $\cdots$, T_8 and E with T_1 and E being the furthest upstream and downstream, respectively. The radii of counters T_1 through T_8, which monotonically increased, are given in Table VI. Each counter was 6.35 mm thick. With the exception of T_1 and T_2, the radii were chosen to correspond to equal steps of t between counters where t is the square of the momentum transfer. The ninth scintillator E was used to monitor the efficiency of counters T_1 through T_8 and was the smallest scintillator.

Half the circumference of each counter was optically coupled to lucite light pipes which transmitted the light to an EMI 9813B two-inch photomultiplier tube.

Ideally the pulse height from each scintillator should be independent of the pion's position in passing through the scintillator. This would assure that the efficiency was uniform throughout the sensitive region of the detector. To test this, a ^{207}Bi gamma source was placed at different positions on the face of each scintillator

Table VI. Radii of the Transmission Counters.

	T_1	T_2	T_3	T_4	T_5	T_6	T_7	T_8	E
Radius (mm)	25.4	50.8	76.2	107.7	132.1	152.4	170.4	186.7	12.7

and the resulting output pulses were observed. By comparing the pulse height as a function of position, the most sensitive region of each counter was found to be that half of the scintillator opposite the photomultiplier tube. This effect was believed to be due to light reflections from the semicircle that was not connected to the light pipes. After this edge was sanded, the pulse height variation across the face of the scintillators was reduced to 25% or less which was felt to be acceptable. The largest variations were found in the largest counters and decreased for the smaller ones.

For a given position of the transmission stack, it was possible to measure seven partial cross sections simultaneously. Counter T_1 was found not to be usable because its diameter was too small. In a blank run, 1/3 of the beam would miss it because of the beam size and divergence.

Multiwire proportional chambers. A general discussion of the multiwire proportional chambers was given above. In this section, a few comments will be made concerning utilizing the wire chambers for measuring the transmitted beam.

As stated earlier, the wire chamber data was acquired only for those events for which the pion was not detected by T_2.

The wire chambers had two distinct advantages over the transmission stack. The first one was the fact that they present a small amount of mass to the pion passing through them as compared to the transmission stack. Therefore they have the ability to detect lower-energy pions than the transmission stack.

To obtain absolute values for the total cross sections, it is necessary to know the absolute efficiencies of the wire chambers and their associated electronics. Unfortunately, it was found that this was not well known, so that it has not been possible to extract total cross sections from the wire chamber data. However, uncertainties in the MWPC efficiencies do not affect their use as a beam profile monitor. All that is necessary is to know the relative beam intensity as a function of the displacement from the beam axis.

Electronics. The electronic system was fairly conventional for a counter experiment. It utilized standard NIM[28] (Nuclear Instrument Modules) modules (i.e., discriminators, D.C. mixers, coincidence units, etc.) for the fast logic circuits and standard CAMAC[29] (i.e., scalers, analog to digital converters (ADC), time-to-digital converters (TDC), etc.) as an interface between the electronics and a PDP-11/45 minicomputer which recorded information on magnetic tape and generally controlled the data acquisition operations. The PDP-11/45 had 24K of memory with the following peripherals: a teletypewriter, CRT display, paper tape reader and punch, two magnetic tape drives, and a RF disk with 256K of storage.

In the electronics for the fast logic, timing pulses of 10 to 15 ns were used with typical discriminator dead times of 10 ns. Coincidences of interest were recorded in scalars capable of handling counting rates of 50 MHz and in a few cases 100 MHz.

The first important coincidence was the determination of a pion to a target. This was accomplished in two ways depending upon whether or not the DISC was used for particle identification. If it

was, the coincidence $Y = TOF1 \cdot TOF2 \cdot DISC \cdot \overline{H}$ defined a pion to target where TOF1 and TOF2 are signals from the two timing counters (without a time-of-flight constraint), DISC is a signal from the DISC, and $\overline{H}$ is a veto signal from either of the halo counters. The logic diagram for this is shown schematically in Figure 14; the logic diagram for the DISC was shown previously in Figure 9.

When particle identification was done without the DISC, then the coincidence $Y = TOF \cdot \overline{H}$ defined a pion to target, where TOF was a three-fold coincidence between the two timing counters and the 200 MHz rf signal from the accelerator. The logic diagram for this is shown schematically in Figure 15. In this case, particle identification was achieved with time-of-flight constraints between TOF1 and TOF2 and between the production target and TOF2. A two-dimensional plot (see the previous discussion of the TOF) was used to select events and to study the rejection of muons and electrons. The TOF system was capable of 1/2 ns time resolution. Not all Y coincidences were due to pions. Some of them were due to accidental coincidences. The source of these accidentals is described in Chapter IV. time, only the measurement of the accidentals will be described.

When the DISC was in use, the accidental coincidences Y_a in Y were monitored by the coincidence $Y_d = TOF1 \cdot TOF2 \cdot DISC \cdot \overline{H}$, where $DISC_d$ is the DISC signal delayed by several rf periods of the beam. When only the TOF system was used, the accidental coincidences Y_a were not measured. However, they are believed to be small, for the following reason. For an accidental to occur in Y, there must first of all be an accidental coincidence between TOF1 and TOF2 and an accidental

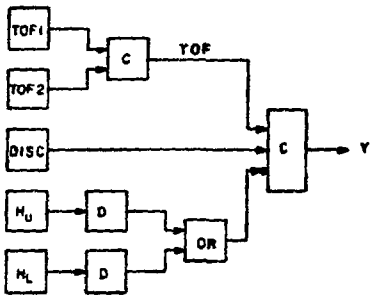

Figure 14. Fast logic diagram for pion identification when the DISC was used. Here, TOF1, TOF2, DISC, H_U, and H_L refer to signals from the first timing counter, second timing counter, DISC, upper halo counter, and lower halo counter, respectively. D, C, and OR stand for discriminator, AND coincidence unit, and OR coincidence unit.

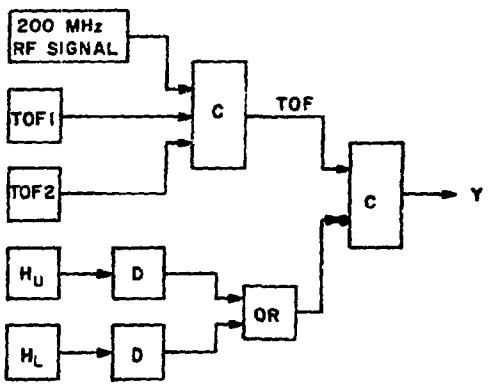

Figure 15. Fast logic diagram for pion identification when the DISC was not used. Here, TOF1, TOF2, H_U, H_L, and 200 MHz rf signal refer to the signals from the first timing counter, second timing counter, and the 200 MHz rf signal from the accelerator, respectively. D, C, and OR stand for discriminator, AND coincidence unit, and OR coincidence unit.

coincidence between the 200 MHz rf signal and TOF2. In addition, these two accidentals must occur within a small time interval in order to be mistaken as a pion in the two-dimensional time-of-flight spectrum.

Whichever way the Y coincidence was formed, it was recorded by a scalar. A typical data run consisted of approximately 10^6 Y events (i.e., beam particles).

Figure 16 indicates schematically the fast logic circuits for the transmission stack and shows the coincidences that were required for the detection of charged particles, the measurement of accidental counts, and the measurement of each counter efficiency.

The detection of a charged particle by the i-th transmission counter was given by the coincidence $Y \cdot T_i$, where T_i was the signal from the i-th counter. The $Y \cdot T_i$ were recorded by scalars.

During the data runs, the efficiency at the center of each transmission counter was continually monitored by the small efficiency counter E at the back of the transmission stack. The efficiency of the i-th counter was given by the ratio of coincidences $E_i = Y \cdot T_i \cdot E$ to $E_T = Y \cdot E$, where E was a signal from the efficiency counter. This efficiency was always better than 99.5%.

To monitor the number of accidental coincidences in $Y \cdot T_i$ due to a stray particle passing through some or all of the transmission counters, the coincidence $Y_d \cdot T_i$ was made. In this coincidence, Y_d is the Y signal delayed by several rf periods of the accelerator.

The coincidence $Y \cdot T_i$ has been the standard way of detecting a charged particle in the i-th transmission counter. However, a better

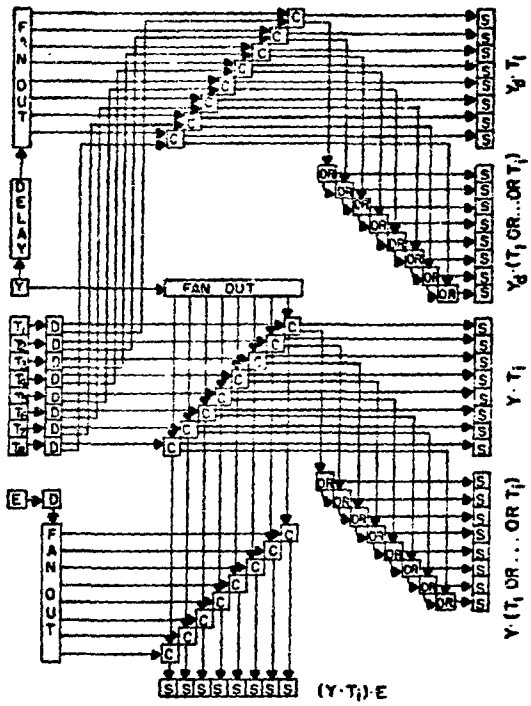

Figure 16. Fast logic diagram for the transmission stack. T_1 through T_8 are the different transmission counter signals, Y is the pion signal. D, C, OR, and S stand for discriminator, AND coincidence unit, OR coincidence unit, and scalar.

way is to use the coincidence $S_i = Y \cdot (T_1 \text{ or } \cdots \text{ or } T_i)$, which was suggested by T. Kycia.[30] This is preferable because it compensates for the loss of pions due to absorption in the transmission stack, which is a fairly large effect at low energies where pions passing through the central region of the stack are absorbed and therefore do not reach the larger counter (e.g., T_7 and T_8). Thus the number of $Y \cdot T_i$ coincidences will not be a true indication of the number of pions that should have been detected. The accidentals in S_i were given by $Y_d \cdot (T_1 \text{ or } \cdots \text{ or } T_i)$.

In each data run, the Y coincidences, Y accidentals, AND coincidences ($Y \cdot T_i$), OR coincidences ($Y \cdot (T_1 \text{ or } \cdots \text{ or } T_i)$), AND accidentals, OR accidentals, and the efficiencies (the $Y \cdot T_i \cdot E$ and $Y \cdot E$ coincidences) were recorded on scalars. The scalar information was then recorded on magnetic tape by the computer.

In addition to these scalar measurements, there was another class of information that was written on magnetic tape. This information came from two types of events. The first were events for which an interaction took place (i.e., there was a scattered pion). Experimentally, a pion was defined to have scattered if there was no $Y \cdot T_2$ coincidence. These were called "good" events. The second were events for which there were no interactions. Only a small subset of these events, triggered at random by the time of flight, were recorded. These were called "random" events. The purpose of the random events was to monitor the beam as well as normalize the scattered event information to the unscattered.

Good events, as well as random events, included information from a coincidence register, two TDC's, and eight ADC's. The good events also included MWPC information, while the random events did not.

The signals from the eight transmission counters were fed directly to eight ADC's to obtain pulse height information. This was done to obtain information on the number of protons reaching the transmission stack.

When the TOF counters were used for the purpose of time-of-flight information, their signals and the 200 MHz rf signal were fed to two TDC's and stored on magnetic tape. The TOF2 signal served as the start pulse for each TDC and the TOF1 pulse and the 200 MHz rf signal were the two respective stop signals. In this way, the time spectrum of the beam particles between TOF1 and TOF2 and between the production target and TOF2 was obtained to allow for particle identification. As discussed before, this information was displayed in a two-dimensional plot to select events and to study muon and electron rejection.

The coincidence register recorded essentially the same information as $Y \cdot T_i$ coincidences, except that it had poorer statistics. Its information was more detailed than the scalars because it could identify which counter was hit first. Also, it could check the consistency of the ADC's. If, according to the coincidence register, T_i did not detect a particle, then the ADC for T_i should be zero. However, the coincidence registers did not operate properly and so this information was unfortunately not available.

The MWPC electronics put out a fast logic signal whenever a signal plane detected a charged particle. A MWPC event was defined

by two coincidences. First there had to be a two-out-of-three coincidence among the three x signal planes, and a two-out-of-three among the three y signal planes. There then had to be a two-fold coincidence between the x and y signals. If there was a two-fold coincidence between the Y and MWPC signals and no $Y \cdot T_2$ coincidence, then the MWPC event was read into the computer and stored on magnetic tape. This event contained information on which wires fired in each of the x and y signal planes. With this information the trajectory of the particle could be constructed, to give such information as the slope of the track and its intersection at the target.

To summarize, for each data run the following information was written on magnetic tape: the ADC's, TDC's, and coincidence register for good and random events; the MWPC events for good events, and the scalars. This task was accomplished by a data acquisition computer program written in MACRO, an assembly language, and FORTRAN. In addition to writing information on magnetic tape, the program handled the transference of data from the CAMAC system to the computer. It also allowed for the monitoring of data runs through histograms and other outputs which were displayed on a CRT. Some of the more useful histograms were the raw MWPC inputs, the raw TDC and ADC inputs, the calculated beam divergences in x and y, and the x and y intercepts of the pion trajectory at the target. The scalar totals and various scalar ratios (e.g., the calculated efficiencies) could also be displayed.

Finally, it should be mentioned that there were some troubles with the computer due to disk failures and hardware failures in the

interface between the computer and the CAMAC system. These troubles resulted in computer crashes (at irregular time intervals) which resulted in some data runs being divided up into several short runs. These were then added together at a later time. Aside from their inconvenience, these crashes did not appear to have any effect on the data.

IV. DATA EVALUATION

In this chapter, the details of the corrections to the data and the statistical treatment of the data will be discussed. In some cases many of the details of a particular correction have been placed in an appendix, to avoid obscuring the principal points of the discussion.

The corrections to the data fall into two classes, with little coupling between them. First, there are those due to the detection system (i.e., systematic effects). These include efficiencies, accidentals, rate effects, geometry of detection system, incorrect identification of pions, absorption, etc. Secondly, there are corrections due to effects caused by interactions of the pion in the target. These include Coulomb effects and knock-out protons in the target and TOF2. Another correction in this class is pion decay. Pions will decay whether the target is "in" or "out." For pion decays before the target, the angular distribution of the muons will be different in the two cases because of the multiple Coulomb scattering of the muons in the target. For pion decays after the target, the angular distributions of the muons will be different in the two cases because of the multiple Coulomb scattering of the muons in the target. For pion decays after the target, the angular distributions of the muons will be different in the two cases because of the energy loss of the pion passing through the target. In a sense, pion decay is a third class of correction, in that the presence of the target modifies the background present in a blank run. From equations (6),

(7), and (8), it was shown that by comparing target and blank data runs, background effects common to both cancel exactly. If the presence of the target modifies this background, then they do not cancel exactly and must be corrected for. All of the classes of corrections are made to the data from each transmission counter before calculating the total cross section itself.

The statistical treatment of the data also falls into two classes. First there is the determination of the statistical error to be assigned to each of the partial cross sections. Then there is the extrapolation of the partial cross sections to zero solid angle. This involves a generalized method of least squares which takes into account the statistical correlations between the counters.

Also in this chapter, there is a discussion of the energy loss calculations which was used to find the pion energy at the center of the target.

Systematic Corrections

To look for systematic effects on the partial cross sections and on the extrapolated total cross section, several tests were made. These will be discussed below.

Positioning of the halo counters and TOF2. The various effects which arise from the presence or absence of the halo counters as well as the relative positioning of these counters and TOF2 with respect to the target have already been discussed.

For a fixed position of TOF2, data runs were made both with and without the halo counters The partial cross sections were found to be systematically larger without the halo counters. With the halos in, the distances between TOF2 and the target and between the halos and the target were varied. The partial cross sections were found to decrease as the separations increased. The final geometry was set with 101.6 mm between the halos and the TOF counter and with 50.8 mm between TOF2 and the target. With these positions, the above systematic errors were felt to be negligibly small. The separation between TOF2 and the target was still small, which helped to keep the number of π decays small.

Positioning of the transmission stack. The effect of different transmission stack positions on the partial cross sections is shown in Figure 17 for π^+ on both Al and Sn at 85 MeV. The error bars on the Al data is the same size as the data points. All corrections have been included in these points except for the Coulomb-nuclear interference correction. These data come from two transmission stack positions, and they are statistically consistent. Therefore it is believed that no systematic effects are introduced by changing the position of the transmission stack. Because of this, for most energies, targets, and pion sign, the data were taken for only one position of the transmission stack. This includes all of the ^{4}He data.

Solid angle. The solid angle covered by each transmission counter was calculated as a mean over the target length $\ell_1 = 76$ mm and counter thickness $\ell_2 = 6.35$ mm, using the expression

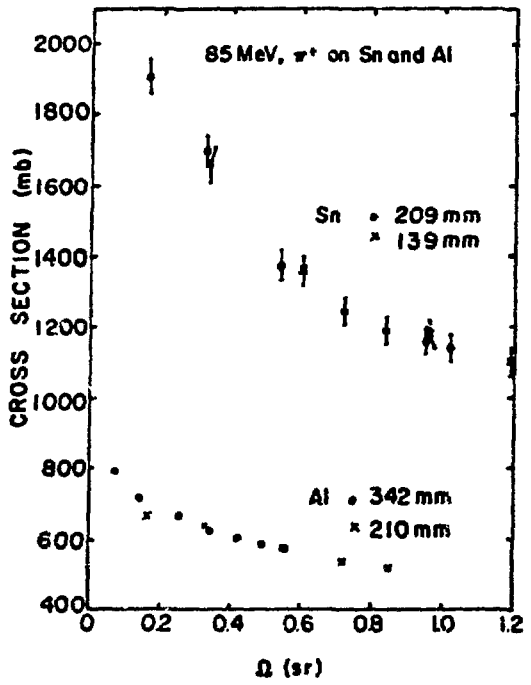

Figure 17. Partial cross sections for two positions of the transmission stack. The data are for 85 MeV π^+ on Al and Sn. They have not been corrected for π-decay and Coulomb-nuclear interference.

$$\bar{\Omega} \simeq \Omega_c \left[1 + \left(\frac{\ell_1 + \ell_2}{2d} \right)^2 \right] \qquad (21)$$

where d is the distance from the center of the transmission counter to the center of the target. The solid angle Ω_c is

$$\Omega_c = 2\pi(1 - \cos\theta_c)$$

$$\simeq \frac{\pi R^2}{d}$$

and

$$\cos\theta_c = d(d^2 + R^2)^{-1/2} \quad ,$$

where R is the radius of the transmission counter. The contributions of ℓ_1 and ℓ_2 to $\bar{\Omega}$ are quite small. For T_1, the transmission counter nearest to the target, d = 770 mm and $\bar{\Omega}$ is only 0.3% larger than Ω_c.

The uncertainty in $\bar{\Omega}$ comes principally from d which was measured to within ±0.4%. By allowing d to vary by ±0.4% in the calculation of the $\bar{\Omega}$'s and by then using these $\bar{\Omega}$'s in the least squares fit to the data, it was found that the uncertainty in d had a negligible effect on the extrapolated total cross section.

In equation (21), the finite beam size was ignored. If the solid angle was calculated as a mean over the cross-sectional area of the beam (it was roughly circular with a radius of 1 cm), while ignoring the target and counter thickness, $\bar{\Omega}$ was found to deviate from Ω_c by less than 0.3%. This calculation assumed that the beam intensity was uniform within the circle and zero outside of it. From the MWPC data, the beam intensity was found not to be uniform as a function of the lateral displacement from the beam axis Rather it was found to be

roughly a gaussian distribution with a standard deviation of ~1 cm. The beam divergence was also found to have approximately a gaussian distribution. If the "true" beam distribution were used, it would have no effect on $\bar{\Omega}$.

Target thickness. Another possible systematic error concerns the target thickness. The measured total cross section should be independent of the thickness.

For a fixed number of incident pions, the thicker the target the greater the number of scattered pions because of the increased number of scattered centers. This is desirable because it increases the statistical accuracy of the data. Unfortunately, increasing the target thickness also increases the magnitude of the single and multiple Coulomb scattering corrections and of the pion decay correction. This is undesirable because it puts greater importance on how well these corrections are made.

This effect was tested for by using ^{12}C targets. With the counter arrangement fixed, two ^{12}C targets with thicknesses of 0.9321 g/cm^2 and 5.467 g/cm^2 were used to measure the total cross section for 145 MeV π^+. The two extrapolated cross sections were 654 ± 13 mb and 659 ± 3 mb for the thinner and thicker targets, respectively (these cross sections do not contain the Coulomb-nuclear interference correction). The smaller error for the thicker target is due to the larger number of scattered centers which resulted in a larger number of scattered pions. The two cross sections are statistically consistent, so there does not appear to be any systematic error due to the

target thickness within the statistical errors. Most of the targets used, including the ^{4}He, had thicknesses of ~1 g/cm .

Rate problems. The consideration of the appropriate counting rate for a data run has several aspects. A high counting rate is desirable to reduce data-taking time. But it can be undesirable if it leads to a loss in particle detection due to dead time effects in the electronics, specifically with the transmission stack electronics.

The dead time was typically 10 ns for the transmission stack discriminators. Thus, if the beam-defining counters identified two pions less than 10 ns apart and neither one was scattered, the second pion would not be detected by the transmission stack; it would be considered as a scattered pion and would systematically give too large a cross section. This could, of course, occur at any counting rate, but the probability for its occurrence increases as the beam intensity increases (i.e., as the counting rate increases).

At high counting rates, the probability increases for two pions to come through the particle-identifying counters together and to be labelled as a single pion. If only one of them scatters, it will not be counted as a scattered pion. This would systematically decrease the measured cross section.

Another effect, which increases at high counting rates, concerns the problem of accidental coincidences in the beam-defining counters. Those accidentals which occur when there is a true pion coincidence do not affect the measured cross section. However, the remaining accidentals create a problem since they indicate an incident pion which

is not detected by the transmission stack. These events can lead to a systematically higher cross section.

During the experiment, the beam intensity was controlled by suitably opening or closing the momentum slits in the LEP channel. The chief source of accidentals was then due to too large a momentum bite in the channel.

To determine whether or not the counting rate was acceptable, the accidentals in the AND coincidences, the OR coincidences, and in the Y coincidences were monitored. If the accidentals in the AND and OR coincidences were less than 1% of the number of AND and OR coincidences for each transmission counter, the measured cross section was found to be rate-independent. This was determined by comparing the total cross sections calculated from ^{4}He data runs with different accidental rates. All data runs with an unacceptable accidental rate (i.e., greater than 1%) were not used to calculate cross sections.

Tests to compare directly the effect of high and low accidental rates on the extrapolated total cross sections were made by using 145 MeV π^- on ^{12}C. For both the target and blank runs, the momentum spread was $\frac{\Delta p}{p} = \pm 0.2\%$ ($\pm 1.0\%$) in the low (high) rate case. The percentage of OR accidental coincidences to OR coincidences monotonically increased from T_1 to T_8, going from 0.37% to 0.96% (1.45% to 2.60%) for the low (high) rates. From the low (high) rate target and blank runs, the extrapolated cross section (it has not been corrected for Coulomb-nuclear interference) was 753 ± 13 mb (781 ± 13 mb) with a reduced χ_R^2 (i.e., the χ^2 per degree of freedom) of 0.1 (5.1). The

high rate data yielded a 4% larger cross section than the low rate data. This is consistent with the dead time effect.

Another test matched the low (high) rate target run with the high (low) rate blank run, giving an extrapolated cross section of 742 ± 13 mb with a reduced χ_R^2 of 2.1 (1.9). This can also be accounted for by the dead time effect as may be seen by considering equation (8). The effect of the dead time at high rates is to decrease the values of R and R_0 from what they would be at a lower counting rate. Using a low (high) rate R and a high (low) rate R , the measured $\sigma(\Omega)$ will be systematically decreased (increased).

The results of these tests are summarized in Table VII.

TABLE VII. Comparison of high- and low-rate data runs for 145 MeV π^- on ^{12}C. The extrapolated cross section σ was obtained from a quadratic fit in Ω to the five largest counters. The reduced χ_R^2 is also given.

Target Rate	Blank Rate	σ(mb)	χ_R^2
low	low	753 ± 13	0.1
high	high	781 ± 13	5.1
low	high	742 ± 13	2.1
high	low	793 ± 13	1.9

It should be noted that Table VII also illustrates the necessity of having the counting rates equal for both the target and the blank

runs. This is important even at low counting rates since this is an effect which will not cancel out in the comparison of target "in" and "out" data runs (see equations (6), (7), and (8)).

Beam profile. Knowledge of the beam profile is important for the ^{4}He target because of its nonuniform thickness. By folding the beam profile with the target geometry, the average target thickness was found to be 1.085 mg/cm^2 with a systematic error of 0.5%. This error was due to an uncertainty in the tails of the beam profile which was roughly gaussian in x and y.

This averaging was accomplished by first making a histogram, using the MWPC data, of the number of particles in both the positive and negative x directions, in 2 mm steps. A weighted average of the target thickness was then made by using the target thickness at each 2 mm step in x (see Table V) weighted by the fraction of the pions in that 2 mm step.

Efficiency, Accidental, and Absorption Corrections

At this time it is appropriate to introduce some notation which will be used here and in the appendices. For the i-th transmission counter T_i, S_i, Ta_i, Sa_i, and E_T are the total number (as recorded on scalers) of AND coincidences, OR coincidences, AND accidentals, OR accidentals, E_i coincidences, and E_T coincidences, respectively. These coincidences were defined in the previous discussion of the electronics. The total number of pions to target is Y, where Y_a is the number of accidental coincidences in Y. Lastly, $E_i = E_i/E$ is taken to be the efficiency of

the i-th transmission counter. A zero subscript on any symbol denotes that quantity for a blank run.

An important point is that only the OR data were used in calculating the partial cross sections. The AND data were used only as an aid in making corrections. The principal reason for this is the effects of the absorption of pions in the transmission stack or the AND data. A pion moving through the central region of the stack may be absorbed before passing through all of the counters. The partial cross sections, for those counters that the π does not reach, would be too large using the AND data. This effect is a function of the pion's energy, increasing (decreasing) as the energy decreases (increases). By using the OR data, the problem is decreased in magnitude as can be seen in Table VIII which gives the raw scalar readings for 51 MeV π^+ on ^{4}He. The absorption of pions in the stack is demonstrated in Table VIII where $S_i > T_i$ and $T_7 > T_8$.

Table VIII. The scalar readings for the AND and OR data. The raw scalar readings are T and S, with S_{ac}, S_e, and S_c being the values of S corrected for accidentals; efficiency; and accidentals, efficiency and absorption; respectively. The numbers are from a data run with 51 MeV π^+ on ^{4}He. The number of beam pions was 1032956.

Counter Number	T	S	S_{ac}	S_e	S_c
2	780412	781849	781259	782750	782162
3	898844	904295	903806	904579	904090
4	931463	941203	940746	941289	940832
5	937442	954973	954529	955027	954583
6	940774	964588	964148	964617	964177
7	942075	972737	972310	972761	972334
8	939623	978370	977951	978387	977969

Another advantage of using the S_i over the T_i is that the OR efficiencies are greater than the AND efficiencies. Even though the OR efficiencies were not measured, they can easily be seen to be nearly 100% by the following argument. Suppose that all of the AND efficiencies for detecting a charged particle were 99.5% (the measured AND efficiencies were always greater than 99.5%). If a charged particle passes through two counters, the probability of (or the efficiency for) being detected is $e = 1 - (1-\varepsilon)(1-\varepsilon)$ where ε is the efficiency of each counter. For $\varepsilon = 0.995$, $e = 0.999975$ for two counters, $e = 0.999999875$ for three, and $e = 0.9999999994$ for four. The value of e is essentially 1 (i.e., the efficiency is 100%) for charged particles passing through two or more counters. For all but the first OR coincidence, most of the particles detected have passed through two or more counters. This becomes especially true for the OR coincidences associated with the larger counters. This means that the efficiency correction should be quite small for S_7 and S_8 and, in fact, it is as can be seen in Table VIII. The details of the efficiency correction will be discussed later.

Accidentals. Accidental counts in Y, T_i, and S_i have several sources. The principal one of these is charged particles (e.g., muons and electrons) associated with the beam; this is dependent on the beam intensity. Other sources of accidentals include cosmic rays, the neutron background (from neutrons produced in the channel and from the production target), and noise pulses in the photomultiplier tubes.

Before using equation (8) to calculate the $\sigma(\Omega)$, the measured R and R_0 need to be corrected for accidentals. To understand how to do this, consider the i-th transmission counter. Let S_t be the true number of counts due to pions and S and S_a be the measured number of counts and accidentals, respectively. Then $R_t = S_t/Y$ is the fraction of pions which are incident on the target and which are detected by the i-th counter. The problem is to relate R_t to the measured ratios $R_m = S/Y$ and $R_a = S_a/Y$. Now R_t is also the probability that a count is due to a pion, R_a is the probability that a count is an accidental, and R_m is the probability that a count is due to either an accidental, or a pion, or both. From probability theory,[31] R_m is given by

$$R_m = R_t + R_a - R_t R_a \tag{22}$$

or

$$S = S_t + S_a - R_t S_a \quad . \tag{23}$$

This can be rewritten as

$$R_t = \frac{R_m - R_a}{1 - R_a} \tag{24}$$

or

$$S_t = Y\left(\frac{S - S_a}{Y - S_a}\right) \quad . \tag{25}$$

Note that in the limit of R_a going to zero, $R_t = R_m$. Equations (22) through (25) hold true for the AND coincidences, with $R_m = T/Y$ and $R_a = T_a/Y$.

To calculate the partial cross sections, equation (23) is applied to both the target "in" and target "out" data. This gives for $\sigma(\Omega)$

$$\sigma(\Omega) = \frac{1}{nt} \ln \left(\left[\frac{R - R_{0a}}{1 - R_{0a}} \right] \left[\frac{1 - R_a}{R - R_a} \right] \right) \quad , \tag{26}$$

where the subscript m has been dropped.

To handle the Y accidentals, an equation similar to equation (23) may be written. To find this, let P be the probability that a Y coincidence is due to a pion. Also let the measured number of pions by Y, the measured number of accidentals be Y_a, and the true number of pions by Y_t. Then

$$Y = Y_t + Y_a - PY_a \quad , \tag{27}$$

where the last term accounts for those accidental counts which occur at the same time as counts due to pions. Solving for Y_t, one obtains from equation (27)

$$Y_t = Y - (1 - P)Y_a \quad . \tag{28}$$

Unfortunately P is an unknown and cannot be determined from the experimental data. However, (1 - P) can be approximated by Y_a/Y, which is an overestimate, since some of the accidental counts occur at the same time as counts due to pions. This then gives for Y_t

$$Y_t \simeq Y - \left(\frac{Y_a}{Y} \right) Y_a \tag{29}$$

Now in all cases where the counting rates were acceptable, it was found that $0.001 \leq Y_a/Y \leq 0.02$. Whether equation (29) or Y were

used in the calculation of the partial cross sections, the total cross section was found to be essentially the same. For example, the total cross sections for 85 MeV and 105 MeV π^+ on ^{4}He decreased by 0.15% and 0.097%, respectively, when equation (29) was used to correct Y.

The problem of accidentals in Y is an effect which cancels out in the comparison of the target and blank runs if $(Y_a/Y) = (Y_{a0}/Y_0)$. To see this, equation (28) is written as

$$Y_t = Y\ 1 - (1-P)\ \frac{Y_a}{Y} \tag{30}$$

and

$$Y_{t0} = Y_0\left[1 - (1-P)\left(\frac{Y_{a0}}{Y_0}\right)\right] \tag{31}$$

for the target and blank runs, respectively. The terms in the square brackets cancel to first order when equations (30) and (31) are substituted into equation (26). Thus, by using only data for which Y_a/Y and Y_{a0}/Y are small and nearly equal, the correction for Y accidentals is unnecessary since it is negligible.

The accidental corrections to the transmission stack data were the only ones that were necessary and they were made using equation (26). The accidental rate in the transmission stack does not cancel in the comparison of the target "in" and "out" data. This is due to the scattering of the beam due to the target, which makes the accidental rate different for the target "in" and "out" data.

Pion losses in the transmission stack. The transmission counter data must be corrected for the inefficiency of the counters and for

pion absorption in the counters. These corrections will be described briefly in this section with the details given in Appendix A. The formalism used here was suggested by G. Burleson.[32]

Let the distribution of particles in the transmission counters be given by N_1, ···, N_7, and N_8, where N_i is the number of particles that hit the i-th counter first. If N_1 start in the first counter, then $\alpha_{12}N_1$ reach the second counter, $\alpha_{13}N_1$ reach the third counter, etc.; and if N_2 start in the second counter, then $\alpha_{23}N_2$ reach the third counter, $\alpha_{24}N_2$ reach the fourth counter, etc. This is shown schematically in Table IX. Each α_{ij} is the probability that a particle starting in the i-th counter will reach the j-th counter.

The pion losses due to nuclear interactions in the counters are dependent upon the thickness of the material the pions pass through. So each $\alpha_{ij}N_i$ should be multiplied by $\beta_i = (\cos\theta_i)^{-1}$, where θ_i is the angle of the particles measured from the z axis to the center of the angular ring defined by the edges of the i-1 and i-th counters.

Table IX. The fractions of N_i starting in the i-th counter and reaching the j-th counter.

Counter Number	1	2	3	4	5	6	7	8
	N_1	$\alpha_{12}N_1$	$\alpha_{13}N_1$	$\alpha_{14}N_1$	$\alpha_{15}N_1$	$\alpha_{16}N_1$	$\alpha_{17}N_1$	$\alpha_{18}N_1$
		N_2	$\alpha_{23}N_2$	$\alpha_{24}N_2$	$\alpha_{25}N_2$	$\alpha_{26}N_2$	$\alpha_{27}N_2$	$\alpha_{28}N_2$
			N_3	$\alpha_{34}N_3$	$\alpha_{35}N_3$	$\alpha_{36}N_3$	$\alpha_{37}N_3$	$\alpha_{38}N_3$
				N_4	$\alpha_{45}N_4$	$\alpha_{46}N_4$	$\alpha_{47}N_4$	$\alpha_{48}N_4$
					N_5	$\alpha_{56}N_5$	$\alpha_{57}N_5$	$\alpha_{58}N_5$
						N_6	$\alpha_{67}N_6$	$\alpha_{68}N_6$
							N_7	$\alpha_{78}N_7$
								N_8

Now the measured T_i and S_i may be expressed in terms of the unknown quantities in Table IX and the measured AND efficiencies ε_i. In order to make the equations tractable it is necessary to make the following assumptions:

$$\alpha_2 \equiv \alpha_{12} = \alpha_{23} = \cdots = \alpha_{78}$$

$$\alpha_3 \equiv \alpha_{13} = \alpha_{24} = \cdots = \alpha_{68}$$

$$\vdots$$

$$\alpha_4 \equiv \alpha_{18}$$

Then α_2, α_3, $\cdots$, α_8 are the probabilities that a pion will not be absorbed in passing through 1, 2, $\cdots$, or 7 transmission counters. The equations for T_1, S_1, T_2, and S_2 are given below:

$$T_1 = \varepsilon_1 N_1 \quad , \tag{32a}$$

$$T_2 = \varepsilon_2 (N_2 + \alpha_2 N_1) \quad , \tag{32b}$$

$$S_1 = T_1 \quad , \tag{33a}$$

$$S_2 = \varepsilon_1 N_1 + \varepsilon_2 N_2 + (1 - \varepsilon_1)\varepsilon_2 \alpha_2 N_1 \quad , \tag{33b}$$

where $(1 - \varepsilon_1)\varepsilon_2\alpha_2$ is the probability that a charged particle will not be absorbed or detected in the first counter but will be detected in the second counter. The equations for T_3 through T_8 and S_3 through S_8 are given in Appendix A. Altogether, there are 15 equations and 15 unknowns, so that the α's and N's can be solved for.

Before calculating the α's and N's, each T_i and S_i was corrected for accidentals using equation (25). Using the corrected T_i's and

S_i's, the N_i's and α_i's were calculated using the results of Appendix A. By knowing the N_i's, the number of particles that should have been detected by each counter were easily calculated. These numbers were then used in equation (8) to calculate the partial cross sections.

The values of α_i's were found to be all about equal. A typical value of α_i was ~.99 even at 51 MeV.

This procedure for correcting the data for counter inefficiencies and pion absorption in the counters has not been used in previous measurements of total cross sections which utilized a transmission stack.[7,8] It is relatively important to the present measurements because low energies are involved. For very low energy (e.g., 20 MeV), this correction could become quite important.

Table VIII gives the raw scalar readings S for 51 MeV π^+ on ^{4}He. It also gives the scalar readings S_e which were corrected for only the counter inefficiency, and the scalar readings S_c which were corrected for counter inefficiency, pion absorption and accidental counts. The S_e were obtained by ignoring accidentals and setting all the α_i's equal to unity. The S_c are less than the raw data because of the accidental correction.

Knockout protons. Another effect which needs to be considered deals with the knockout of protons from the target and TOF2. This could affect the data in two ways. First, protons from the target can be detected by the transmission stack. If they are, a pion which did interact in the target and missed the transmission stack could be counted as a pion that did not interact. Secondly, protons from TOF2 will be detected by the transmission stack in the case of a

blank run but will not in a target run. This is because they are of low energy and will probably stop in the target.

The source of knockout protons is inelastic pion interactions in the target and TOF2. For this reason, it is not necessary to correct the data for any effects due to these protons. This can be seen by considering either equations (16) or (18) in Chapter II. Both of these equations contain a correction term for inelastic events which is given by $\int_{0°}^{\Omega}\left(\frac{d\sigma}{d\Omega}\right)_{inel}d\Omega$, where $\left(\frac{d\sigma}{d\Omega}\right)_{inel}$ is defined to be the differential cross section for all inelastic interactions. Because this correction goes to zero as Ω goes to zero, it does not affect the extrapolated cross section $\sigma(\Omega=0)$. Consequently, it is unnecessary to correct the data for knockout protons.

Statistical Analysis and Extrapolation Procedure

The calculation of the statistical errors on the partial cross sections and the extrapolation procedure used to obtain the total cross sections are the subjects of this section. The statistical correlations between the partial cross sections are included in the extrapolation procedure. This is done using a generalized least squares fit with a polynomial in t, the square of the momentum transfer. This is a technique which has not been employed in previous measurements of the total cross section.[7,8]

Error analysis. In this experiment the following question is asked: What fraction of the pions incident on the target will be

found within the solid angle Ω_i subtended by the i-th transmission counter at the center of the target? The probability distribution which is appropriate for this situation is the binomial distribution. This distribution gives the probability of finding exactly r successes in N independent trials, when the probability of success in each trial is a constant P. In this experiment, the number of independent trials Y and the number of successes S_i are both measured (the effects of accidental counts, pion absorption, and inefficiencies of the counters on S_i are being ignored for the moment). The probability of there being S_i successes is $R = S_i/Y$.

The variance σ^2, where σ is the standard deviation, for the binomial distribution is

$$\sigma^2 = NP(1 - P) \quad . \tag{34}$$

If P is unknown, an unbiased estimate of the variance is given by

$$\sigma^2 = \left(\frac{N}{N-1}\right) N \left(\frac{r}{N}\right)\left(1 - \frac{r}{N}\right)$$

$$= N\left(\frac{r}{N}\right)\left(1 - \frac{r}{N}\right) \tag{35}$$

for large N. In terms of the notation used to describe the present experimental data, equation (35) becomes

$$(\Delta S_i) = Y(R_i)(1 - R_i) \tag{36}$$

or

$$(\Delta S_i)^2 = \left(\frac{S_i}{Y}\right)(Y - S_i) \quad , \tag{37}$$

where ΔS_i, instead of σ, denotes the standard deviation (σ has been used to represent cross sections). Writing equation (36) in terms of ΔR_i, one obtains

$$(\Delta R_i)^2 = \frac{R_i(1 - R_i)}{Y}$$

or

$$\left(\frac{\Delta R_i}{R_i}\right)^2 = \frac{1 - R_i}{R_i Y} \quad . \tag{38}$$

It should be noted that equation (37) is not the error that is sometimes quoted in total cross section papers. In these cases the error is given by

$$(\Delta S_i)^2 = Y - S_i \tag{39}$$

which is appropriate for the normal or Gaussian distribution. Equation (39) approaches equation (37) in the limit that R_i goes to unity.

The partial cross sections $\sigma_i \equiv \alpha(\Omega_i)$ are given by, according to equation (8),

$$\sigma_i = \frac{1}{nt} \ln\left(\frac{R_{0i}}{R_i}\right) \quad .$$

The statistical error $\Delta\sigma_i$ in σ_i is then

$$\Delta\sigma_i = \frac{1}{nt}\left[\left(\frac{\Delta R_{0i}}{R_{0i}}\right)^2 + \left(\frac{\Delta R_i}{R_i}\right)^2\right]^{1/2} \quad . \tag{40}$$

With the use of equation (38), $\Delta\sigma_i$ is then given by

$$\Delta\sigma_i = \frac{1}{nt}\left[\left(\frac{1 - R_{0i}}{R_{0i}Y_0}\right) + \left(\frac{1 - R_i}{R_i Y}\right)\right]^{1/2} \quad . \tag{41}$$

The next matter to be considered is the effect of the statistical errors of the measured efficiencies on the $\Delta\sigma_i$'s. The statistical errors of the AND efficiencies are given by the binomial distribution. Using the definition $\epsilon_i = E_i/E_T$, one obtains the error $\Delta\epsilon_i$ is given by

$$(\Delta\epsilon_i) = \frac{\epsilon_i(1 - \epsilon_i)}{E} \tag{42}$$

or

$$\left(\frac{\Delta\epsilon_i}{\epsilon_i}\right)^2 = \frac{1 - \epsilon_i}{\epsilon_i E} \quad . \tag{43}$$

With $\epsilon_i \geq .995$, $(\Delta\epsilon_i/\epsilon_i)^2$ is negligible compared to $(\Delta R_i/R_i)^2$.

If e_i is the OR efficiency, the Δe_i is also given by the binomial distribution as

$$\left(\frac{\Delta e_i}{e_i}\right)^2 = \frac{1 - e_i}{e_i E} \quad . \tag{44}$$

The e_i's are unknown, except for $e_1 = \epsilon_1$, but they are given approximately by

$$e_i = 1 - (1 - \epsilon_1)(1 - \epsilon_2) \cdots (1 - \epsilon_i) \quad . \tag{45}$$

For the counters four through eight the approximation $e_i = 1$ is quite good, as was discussed earlier. Because $e_i = 1$, $(\Delta e_i/e_i)^2$ is also negligible compared to $(\Delta R_i/R_i)^2$. Consequently, it has a negligible effect on $\Delta\sigma_i$.

The effect of the statistical errors of the accidentals count on $\Delta\sigma_i$ will be considered next. First, it was shown in equation (24) that

$$R_t = \frac{R - R_a}{1 - R_a} \quad .$$

Then R_t/R_t is given by

$$\left(\frac{\Delta R_t}{R_t}\right) = \left[\frac{\Delta(R - R_a)}{(R - R_a)}\right]^2 + \left[\frac{\Delta(1 - R_a)}{(1 - R_a)}\right]^2$$

or

$$\left(\frac{\Delta R_t}{R_t}\right) = \frac{1}{Y}\left[\frac{R(1 - R) + R_a(1 - R_a)}{(R - R_a)^2} + \frac{R_a}{1 - R_a}\right] \quad , \tag{46}$$

where equation (38) has been used in deriving equation (45). With this result, $\Delta\sigma_i$ can be calculated from

$$\Delta\sigma_i = \frac{1}{nt}\left\{\frac{1}{Y}\left[\frac{R_{0i}(1 - R_{0i}) + R_{0ai}(1 - R_{0ai})}{(R_{0i} - R_{ai})} + \frac{R_{0ai}}{1 - R_{0ai}}\right]\right.$$

$$\left. + \frac{1}{Y}\left[\frac{R_i(1 - R_i) + R_{ai}(1 - R_{ai})}{(R_i - R_{ai})^2} + \frac{R_{ai}}{1 - R_{ai}}\right]\right\}^{1/2} . \tag{47}$$

Finally, it should be noted that this expression reduces to equation (41) in the limit of no accidentals.

Fitting the data. The data consists of partial cross sections σ_i (with statistical errors $\Delta\sigma_i$) which were measured at different values of t_i, the square of the momentum transfer. This is illustrated in Figure 18, where the partial cross sections are plotted

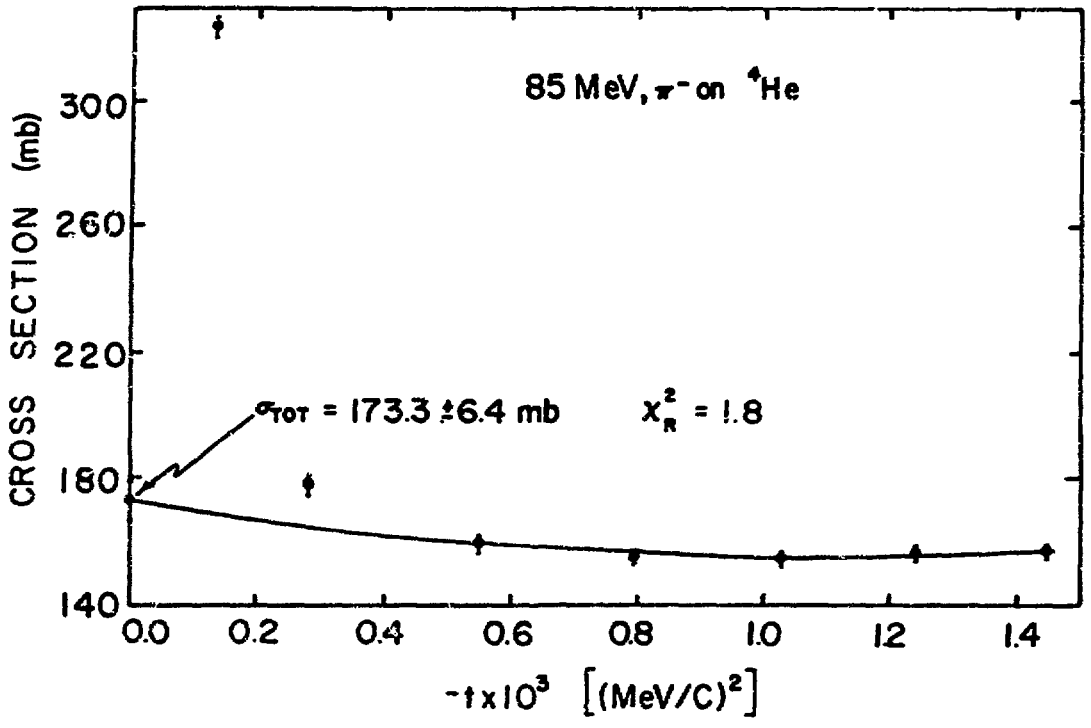

Figure 18. Partial cross sections for π^- on ^{4}He at 85 MeV. The partial cross sections contain all the experimental corrections. The curve is a least-squares quadratic fit to the last five partial cross sections with a reduced χ_R^2 of 1.8. The intercept at $-t = 0$ gives the total cross section $\sigma_{TOT} = 173.3 \pm 6.4$ mb.

versus t for 85 MeV π^- on ^{4}He. The data points contain all the experimental corrections.

The total cross section $\sigma_{TOT} \equiv \sigma(t=0)$ was found from the partial cross sections by fitting an appropriate function to the data and then extrapolating this function to t=0. The curve in Figure 18 was obtained by fitting a second-order polynomial in t to the five points with the largest values of t. Also shown in the figure are the t=0 intercept (i.e., σ_{TOT}) and the reduced χ^2_R. The purpose of this section is to indicate how the data were fit.

In Chapter II, two possible fitting functions were given. These were

$$\sigma(t) = A + Bt + Ct^2 + \cdots \tag{48}$$

and

$$\ln \sigma(t) = A' + B't + C't'^2 \quad . \tag{49}$$

In either case, the fitting function is a polynomial in t so that the following formalism will apply to both.

Consider the polynomial fitting function $\sigma(t_i,a_j) \equiv \sigma_i(a_j)$, where

$$\sigma_i(a_j) = \sum_{j=0}^{N} a_j t_i^j \quad . \tag{50}$$

The a_j's are a set of parameters which define a polynomial of order N. Initially, each a_j is unknown, but it can be found, along with its associated statistical error Δa_j, by the method of least squares.

If the partial cross sections σ_i are statistically uncorrelated, then the a_j's are found by minimizing the function M, defined by

$$M = \sum_{i=1}^{P} \frac{(\sigma_i - \sigma_i(a_j))^2}{(\Delta\sigma_i)^2} \tag{51}$$

with respect to each a_j. In equation (51) P is the number of data points and $\sigma_i(a_j)$ is given by equation (50). The minimizing of M with respect to each a_j, which is

$$\frac{\partial M}{\partial a_j} = 0 \quad , \tag{52}$$

gives N+1 equations which can be solved for the a_j's. The minimum value of M is designated by χ^2, the chi-squared function. The goodness of the fit is determined by the value of χ^2 or the reduced χ_R^2 (i.e., the chi-squared per degree of freedom) defined by

$$\chi_R^2 = \frac{\chi^2}{P - N} \tag{53}$$

where P-N gives the degrees of freedom in the fit. Here, P and N are the number of points and the order of the polynomial, respectively. A useful criterion for a good fit is that $\chi_R^2 \approx 1$. However, the usual procedure is to look up the χ^2 probability in a table of the χ^2 distribution. Note that the condition $(P - N) \geq 1$ must be fulfilled to allow for a statistical error analysis.

The variance $(\Delta a_j)^2$ of the a_j obtained from equation (52) is given by

$$(\Delta a_j)^2 = H_{jj}^{-1} \tag{54}$$

where H is a matrix whose elements are given by

$$H_{ij} = \frac{1}{2} \frac{\partial^2 M}{\partial a_i \partial a_j} \quad . \tag{55}$$

The above treatment of M to find the a_j's is standard and can be found in many texts on statistical analysis.[31,33,34]

What has just been described, however, is not appropriate for fitting the σ_i because they are statistically correlated. Therefore, it is necessary to use the covariance form of the method of least squares,[31] where M is now defined by

$$M = D^T V^{-1} D \quad , \tag{56}$$

where D is a column matrix (or vector) with elements $D_i = \sigma_i = \sigma_i(a_j)$ and V is the covariance matrix for the errors $\Delta\sigma_i$ with elements

$$\begin{aligned} V_{ij} &= \langle (\sigma_i - \langle \sigma_i \rangle)(\sigma_j - \langle \sigma_j \rangle) \rangle \\ &= (\Delta\sigma_{ij})^2 \end{aligned} \tag{57}$$

(note that V is symmetric with diagonal elements $V_{ii} = (\Delta\sigma_i)^2$). Assuming V is known, then the a_j's are found by minimizing M as before and solving the equations

$$\frac{\partial M}{\partial a_j} = 0 \quad .$$

The variance $(\Delta a_j)^2$ of each a_j is again determined by equations (54) and (55) with M given by equation (56). To measure the goodness of fit, M was treated as a generalized χ^2, so that the criterion for a good fit was still $\chi_R^2 \approx 1$.

The difficulty in applying the covariance form of the method of least squares to the σ_i is in finding the covariance matrix V. The

first step is to determine the covariance $(\Delta S_{ij})^2$ of S_i and S_j, which is shown in Appendix B. The result is

$$(\Delta S_{ij})^2 = YR_i(1 - R_j) \quad , \tag{58}$$

where $j \geq i$. Using this result, it is shown in Appendix C that

$$\begin{aligned} V_{ij} &= (\Delta\sigma_{ij})^2 \\ &= (\Delta\sigma_j)^2 \quad , \end{aligned} \tag{59}$$

where $j \geq 1$. Since V is symmetric, $V_{ji} = (\Delta\sigma_j)^2$ also.

The details of how the a_j's are found from equations (56) and (59) are given in Appendix D.

It was found that whether equation (48) or (49) was to fit the partial cross sections, the total cross sections σ_{TOT} (and its statistical error) were essentially the same in the two cases. However, equation (48) was preferred because in general it gave a slightly better χ_R^2. Hence, all of the results presented in Chapter V have been obtained by using equation (48). Furthermore, it was found that in most cases a quadratic fit in t gave the best χ_R^2, so that all of the final results were obtained from a quadratic fit in t.

Finally, the use of the smoothing function $\int_0^{\Omega} \left(\frac{d\sigma}{d\Omega}\right)_{ne} d\Omega$ discussed at the end of Chapter II was tried. It was found to have no effect on the order of polynomial used in the fit. Also, as expected, σ_{TOT} (i.e , $\sigma(t=0)$ was found to be unaffected by the smoothing function. Consequently all of the final results do not include the use of this smoothing function.

Single and Multiple Coulomb Scattering

In addition to the corrections for accidental counts, counter inefficiency, and pion absorption in the counter, each measured partial cross section $\sigma(\Omega)$ was also corrected for those pions which were scattered outside the solid angle Ω by multiple and single Coulomb scattering. If $\sigma_m(\Omega)$ and $\sigma_c(\Omega)$ are the cross sections for a pion to undergo multiple scattering and single Coulomb scattering outside the solid angle Ω, respectively, then the corrected partial cross section $\sigma'(\Omega)$ is given by

$$\sigma'(\Omega) = \sigma(\Omega) - \sigma_m(\Omega) - \sigma_c(\Omega) \quad . \tag{60}$$

Two approaches have been adopted in making single and multiple Coulomb scattering corrections. The first was to ignore all finite geometrical effects of the beam. For this assumption the corrections could be done analytically. The second approach folded in the beam geometry to see what effect it had on the corrections. This was handled through the use of a Monte Carlo computer program. Both approaches will be explained in detail.

Multiple Coulomb scattering. Multiple Coulomb scattering arises from the many successive Coulomb scatterings of the pion as it passes through the target. Because of the very large cross section for Coulomb scattering at small angles and the high velocity for even a 51 MeV pion (51 MeV was the lowest energy at which the total cross sections were measured), the probability for pions to scatter at small angles is large. Furthermore, a pion undergoing very small

angle scatterings will generally emerge from the target at a small angle relative to its original trajectory. This small angle is the cumulative statistical superposition of a large number of deflections.

Because of its statistical nature, it is useful to treat multiple scattering in terms of probability. If dP is the probability for a pion incident on a target to be scattered between θ and $(\theta + d\theta)$ (see Figure 19), it is given by

$$\begin{aligned} dP &= f(\theta)\, d\Omega \\ &= 2\pi\, f(\theta) \sin\theta\, d\theta \\ &\simeq 2\pi\, f(\theta)\, \theta\, d\theta \quad , \end{aligned} \tag{61}$$

where $d\Omega$ is the solid angle subtended by the angular ring shown in Figure 19 at the target. The function $f(\theta)$ is the multiple scattering angular distribution, and the approximation $\sin\theta \simeq \theta$ is adequate for small-angle scattering.

The standard representation of $f(\theta)$ is due to Moliere[35] and is given by

$$f(\theta) = \frac{1}{\chi_c^2 B}\left[f_0(\theta) + \frac{1}{B} f_1(\theta) + \frac{1}{2B^2} f_2(\theta) + \cdots\right] , \tag{62}$$

where usually only the first three terms are used. The $f_k(\theta)$ are defined by

$$f_k(\theta) = k! \int_0^\infty u J_0\left(\frac{u\theta}{\chi_c B^{1/2}}\right) \exp\left(\frac{u^2}{4}\right)\left(\frac{u^2}{4}\ln\left(\frac{u^2}{4}\right)\right)^k \tag{63}$$

with $k = 0, 1, 2$ and where $f_0(\theta)$ is the well-known Gaussian

$$f_0(\theta) = 2\exp\left(\frac{-\theta^2}{\chi_c^2 B}\right) \quad . \tag{64}$$

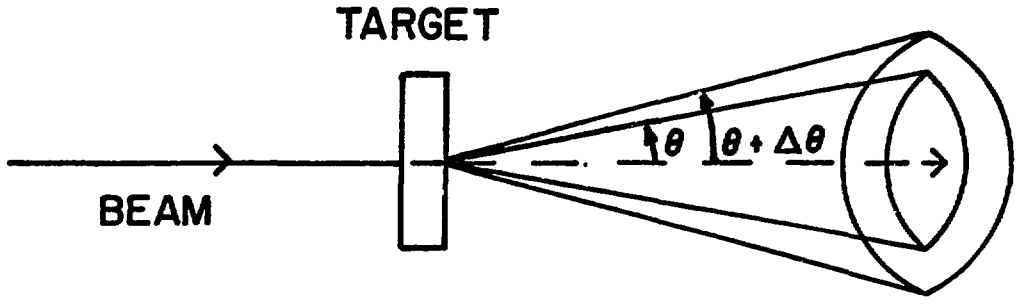

Figure 19 The effect of multiple Coulomb scattering on the incident beam. Here, θ is the multiple Coulomb scattering angle.

There are slight variations in the definitions of χ_c and B; those of Marion and Zimmerman[36] were adopted, so that χ_c^2 is given by

$$\chi_c^2 = 0.1569 \left(\frac{z_1(z_1 + 1)z_2^2}{A} \frac{t}{pv^2} \right) \quad , \tag{65}$$

where z_1 is the atomic number of the target, z_2 is the atomic number of the pion ($z_2 = \pm 1$), A (in g) is the atomic weight of the target, t (in g/cm^2) is the target thickness, and p (in MeV/c) and v are the momentum and velocity of the pion in the center of mass frame, respectively. The quantity B is defined by

$$B - \ln B = b \quad , \tag{66}$$

where

$$b = \ln \left(\frac{2730(z_1 + 1)z_1^{1/3} z_2^2 t}{A\beta^2} \right) - 0.1544 \quad . \tag{67}$$

For small θ the Gaussian term $f_0(\theta)$ is the dominant term in the series. For large θ the dominant term is $f_1(\theta)$, and $f_2(\theta)$ is significant only for a small range of intermediate values of θ.

Using the expression for $f(\theta)$, one can correct the measured partial cross sections $\sigma(\Omega)$ for multiple Coulomb scattering. If $\sigma_m(\Omega)$ is the cross section for a pion to multiple scatter outside Ω, then the probability $P(\Omega)$ for the pion to be found within Ω is

$$P(\Omega) = \exp(-nt\sigma_m(\Omega)) \quad , \tag{68}$$

where n is the number of nuclei/cm^3 and t is the target thickness in cm. This gives

$$\sigma_m(\Omega) = -\frac{1}{nt} \ln P(\Omega) \tag{69}$$

as the correction for multiple Coulomb scattering. To make the correction the $\sigma_m(\Omega)$ are subtracted from each partial cross section $\sigma(\Omega)$, as shown in equation (60). The probability $P(\Omega)$ is, with the use of equation (61),

$$P(\Omega) = 2\pi \int_0^{\theta} f(\theta)\, \theta\, d\theta \tag{70}$$

or

$$P(\Omega) = 1 - 2\pi \int_{\theta}^{\infty} f(\theta)\, \theta\, d\theta \quad . \tag{71}$$

The last step follows from the normalization of $f(\theta)$, which is

$$\int_0^{\infty} f(\theta)\, 2\pi\theta\, d\theta = 1 \tag{72}$$

Finally, $\sigma_m(\Omega)$ is given by

$$\sigma_m(\Omega) = -\frac{1}{nt} \ln\left(1 - 2\pi \int_{\theta}^{\infty} f(\theta)\, \theta\, d\theta\right) \quad . \tag{73}$$

In using equation (73), $f(\theta)$ is approximated by the first term in equation (62), which is a good approximation for small angles, where $f_0(\theta)$ is the dominant term (the validity of this approximation for larger θ will be discussed later). By using the approximation

$$f(\theta) \approx \frac{1}{\chi_c^{\,2B}} f_0(\theta) \quad ,$$

one can write equation (72) as

$$\theta_m(\Omega) = -\frac{1}{nt} \ln\left(1 - \frac{4\pi}{\chi_c^{\,2B}} \int_{\theta}^{\infty} \exp\left(\frac{-\theta'^2}{\chi_c^{\,2B}}\right) \theta'\, d\theta'\right)$$

$$= -\frac{1}{nt} \ln\left(1 - 2\pi \int_{u}^{\infty} \exp(-u')\, du'\right) \quad , \tag{74}$$

where $u = \frac{\theta^2}{\chi_c^2 B}$. The integral in equation (74) is the incomplete gamma function. For the energy range spanned by the ^{4}He data (i.e., 51 to 105 MeV), the correction given by equation (74) to the measured partial cross sections $\sigma(\Omega)$ was large for counter number one, very small for counter number two, and zero for counters three through eight. Since only counters four through eight were used in obtaining the total cross section (the reason for this will be explained later), the multiple scattering correction given by equation (74) had no effect on the total cross section.

Equation (74) does not include the multiple scattering of pions by the atomic electrons. This effect may be taken into account by changing the parameter B as shown by Fano.[37] However, in the case of the ^{4}He data, this had no effect on the total cross sections.

So far, the finite beam size and beam divergence have not been considered. To do so, one needs to consider the effect on the beam of multiple scattering in TOF2. Note that because the MWPC were positioned upstream of TOF2, they only gave information on the beam size and divergence at TOF2.

It is not possible to handle the beam size and divergence analytically, but they can be handled by Monte Carlo methods with a computer. This is a technique which uses random numbers to simulate statistical processes such as multiple scattering. The process of simulation involves setting up a computer model of the physical effect by performing operations which represent the motions and

interactions of the real particles. The physical effects must be directly represented by probability distributions so that the use of random numbers allows sampling from these distributions in order to simulate the physical effect.

The details of the multiple scattering Monte Carlo program are discussed in Appendix E. The program starts with an individual pion at the upstream face of TOF2 and follows its history until it hits or misses the transmission stack. It repeats this process thousands of times for both the target "in" and target "out" situations. The program then gives $r(\Omega)$ ($r_0(\Omega)$) the fraction of pions starting at TOF2 and hitting the i-th transmission counter when the target is "in" ("out"). For nt nuclei/cm^2, the correction $\sigma_m(\Omega)$ is

$$\sigma_m(\Omega) = \frac{1}{nt} \ln\left[\frac{r_0(\Omega)}{r(\Omega)}\right] \tag{75}$$

and it is subtracted from each $\sigma(\Omega)$.

It was found that $\sigma_m(\Omega)$ as obtained from equation (75) was insensitive to the finite beam size but was quite sensitive to the beam divergence. Because there were uncertainties in the tails of the pion angular distribution in the xz and yz planes, a check was made to see what effect the tails had on $\sigma_m(\Omega)$. For 51 MeV pions, where the multiple scattering correction was the largest, the corrections $\sigma_m(\Omega)$ for counters one through three were found to vary considerably, depending upon what assumptions were made on the form of the tails. For counter four, $\sigma_m(\Omega)$ was always very small or zero, and for counters five through eight $\sigma_m(\Omega)$ was always zero. Consequently, only counters four through eight were used to obtain

the total cross section. The price paid for this is a larger statistical error on the total cross section. This is necessary in view of the difficulties in correcting the small angle counters. This problem will reappear in the discussions of single Coulomb scattering and pion decay. Its effect is shown rather dramatically in Figure 17, where $\sigma(\Omega)$ is plotted versus -t (only counters two through eight were plotted). The data points have been corrected for all effects, yet $\sigma(\Omega)$ for counter two is considerably larger than the other partial cross sections.

Because of the expense in running Monte Carlo computer programs, equation (74) was used to correct for multiple Coulomb scattering. In the case of ^{4}He, this makes no difference in the final total cross sections. However, it could make a difference for targets such as Sn and Pb. It was felt that so long as equation (74) gave a small correction for counters two and three, the corrections for counters four through eight were negligible.

Single Coulomb scattering. The measured partial cross sections $\sigma(\Omega)$ are corrected for single Coulomb scattering by subtracting

$$\sigma_c(\Omega) = \int_{\Omega}^{4\pi} \left(\frac{d\sigma}{d\Omega}\right)_c d\Omega \qquad (76)$$

from each $\sigma(\Omega)$, as in equations (17) or (60).

For nonrelativistic pions, $\left(\frac{d\sigma}{d\Omega}\right)_c$ is given by the celebrated Rutherford scattering formula, given in cgs units, by

$$\left(\frac{d\sigma}{d\Omega}\right)_c = \frac{1}{4}\left(\frac{ze^2}{m_\pi v^2}\right)\left(\sin\frac{\theta}{2}\right)^{-4} , \qquad (77)$$

where m_π is the pion's rest mass, z is the atomic number of the target, e is the unit of charge, and v and θ are the pion velocity and scattering angle in the center of mass, respectively. Equation (77) is valid for both the classical calculation of or the quantum mechanical treatment of Coulomb scattering (for spinless particles).

The relativistic generalization of equation (77) for spinless particles is the Mott scattering formula,[38] given in cgs units, by

$$\left(\frac{d\sigma}{d\Omega}\right)_c = \frac{1}{4}\frac{ze^2}{m_\pi v^2}(1-\beta^2)\left(\sin\frac{\theta}{2}\right)^{-4} \tag{78}$$

where $\beta = v/c$. Using the kinematic relations $E = m_\pi c^2(1-\beta^2)^{-1/2}$ and $\beta = pc/E$, where E and p are the total energy and momentum of the pion in the center of mass, one can write equation (78) as

$$\left(\frac{d\sigma}{d\Omega}\right)_c = \frac{1}{4}\left(\frac{ze\ E}{c^2p^2}\right)^2\left(\sin\frac{\theta}{2}\right)^{-4}$$

or

$$\left(\frac{d\sigma}{d\Omega}\right)_c = 4\left(\frac{ze^2E}{c^2}\right)^2\left(\frac{1}{t^2}\right) \quad , \tag{79}$$

where

$$t = 4p^2\sin^2\frac{\theta}{2}$$

$$= -2p^2(1-\cos\theta)$$

$$= -\frac{1}{\pi}p^2\Omega \quad ,$$

since $\Omega = 2\pi(1-\cos\theta)$. With the use of

$$\left(\frac{d\sigma}{dt}\right)_c = \left(\frac{d\sigma}{d\Omega}\right)_c\frac{d\Omega}{dt} \quad ,$$

one can write

$$\left(\frac{d\sigma}{dt}\right)_c = 4\pi\left(\frac{ze^2E}{c^2p}\right)^2\left(\frac{1}{t^2}\right)$$

or

$$\left(\frac{d\sigma}{dt}\right)_c = 40\pi\left(\frac{z\alpha}{\beta}\right)^2\left(\frac{\hbar c}{t}\right)^2 \quad , \tag{80}$$

where h is Plank's constant and α is the fine structure constant. If in equation (80), $\hbar c = 197.33$ MeV fm and t is in $(MeV/c)^2$, $\left(\frac{d\sigma}{dt}\right)_c$ will have units of $mb/(MeV/c)^2$.

In equation (80) it is assumed that both the pion and the ^{4}He nucleus are point charges. If the finite charge distributions of the pion and the ^{4}He nucleus are taken into account, equation (80) becomes

$$\left(\frac{d\sigma}{dt}\right)_c = -40\pi\left(\frac{z\alpha}{\beta}\right)^2\left(\frac{\hbar c}{t}\right)^2\left(F_\pi(t)F_{He}(t)\right)^2 \quad , \tag{81}$$

where $F_\pi(t)$ and $F_{He}(t)$ are the charge form factors for the pion and ^{4}He nucleus, respectively. The form factors were assumed to be Gaussian, so that

$$F_\pi(t) = \exp\left(\frac{-R_\pi^2|t|}{6\hbar c}\right) \tag{82}$$

and

$$F_{He}(t) = \exp\left(\frac{-R_c^2|t|}{6\hbar c}\right) \tag{83}$$

where $|t|$ is the absolute value of t in $(MeV/c)^2$, $\hbar c = 197.33$ MeV fm, and $R_\pi = 0.8$ fm and $R_c = 1.63$ fm are the charge radii of the pion[8,39] and the ^{4}He nucleus[40]. Combining equations (81), (82), and (83), one obtains

$$\left(\frac{d\sigma}{dt}\right)_c = -40\pi\left(\frac{z\alpha}{\beta}\right)^2\left(\frac{\hbar c}{t}\right)^2 \exp\left(\frac{-(R + R_c)|t|}{3\hbar c}\right) \qquad (84)$$

In terms of $\left(\frac{d\sigma}{dt}\right)_c$, the Coulomb correction given by equation (76) becomes

$$\sigma_c(t) = \int_t^{t_{max}} \left(\frac{d\sigma}{dt'}\right)_c dt' \quad , \qquad (85)$$

where t_{max} is the maximum t that is kinematically possible. For ease of computation, t_{max} was assumed to be infinite. This introduces a negligible error, since $\left(\frac{d\sigma}{dt}\right)_c$ is very small for large t. If equation (84) is substituted in equation (85), the result is

$$\sigma_c(t) = -40\pi\left(\frac{\alpha}{\beta}\right)^2 (\hbar c)^2 \int_t^{\infty} \frac{1}{t'} \exp\left(\frac{-(R_\pi^2 + R_c^2)|t'|}{3\hbar c}\right) dt' \qquad (86)$$

Integrating by parts, one obtains the following expression for $\sigma_c(t)$ (in mb):

$$\sigma_c(t) = -40\pi\left(\frac{z\alpha}{\beta}\right)^2 \frac{\hbar c}{t}\left[\exp\left(\frac{-(R_\pi^2 + R_c^2)|t|}{3\hbar c}\right) - \frac{(R_\pi^2 + R_c^2)|t|}{3\hbar c} E_1\left(\frac{(R_\pi^2 + R_c)|t|}{3\hbar c}\right)\right] \qquad (87)$$

where $E_1(z)$ is the exponential integral

$$E_1(z) = \int_z^{\infty} \frac{e^{-x}}{x} dx \quad .$$

The inclusion of the finite charge distributions of the pion and ^{4}He nucleus in equation (87) is a small correction to the result obtained with point charges. The point charge limit is reached as the quantity in square brackets in equation (87) goes to unity.

Equation (87) does not include any effects due to the finite size or beam divergence. To find their effedts on $\sigma_c(\Omega)$, a Monte Carlo computer program was used. The details of this calculation are given in Appendix E. This program calculates the probability $P_c(\Omega)$ for a pion to single Coulomb scatter within the solid angle Ω. Then $\sigma_c(\Omega)$ is given by

$$\sigma_c(\Omega) = -\frac{1}{nt} \ln P_c(\Omega) \tag{88}$$

For 51 MeV pions, where the single Coulomb scattering correction was the largest, equation (88) was found to be insensitive to the beam size, but sensitive to the beam divergence. The corrections $\sigma_c(\Omega)$ as calculated from equation (88) and (87) were different for counters one through three but essentially the same for counters four through eight. Furthermore, it was found that the corrections for counters one through three depended on the assumptions made about the form of the tails of the angular distribution of the pions. Consequently, the Coulomb corrections were made using equation (87), since only counters four through eight were used to obtain the total cross section. The size of the Coulomb effect on the total cross section monatomically decreased from a ~10% correction at 51 MeV to ~1.5% correction at 105 MeV.

Pion Decay

For Y beam particles, the i-th transmission counter measures S_i counts. Because of pion decay, S_i contains a certain

number of muons designated by S_i^{μ}. These muons give effects that must be corrected for. For example, muons from the decay of pions upstream of the target give some apparent additional scattering from the target. For muons from the decay of pions downstream of the target the problem is somewhat different. If the decay muon always hit the same transmission counter that the parent pion would have hit if it had not decayed, then there would be no need for a correction. However, this does not always happen, so the partial cross sections σ_i need to be corrected for this effect.

The effect of muons from the decay of pions upstream of the target will be considered first. If it were not for the presence of the target, the distribution of muons hitting the transmission stack would, in principle, be the same for target "in" and "out." Consequently, these muons would form a background common to both the target "in" and "out" runs and would cancel out according to equations (6), (7), and (8). However, the distributions of muons at the transmission stack will be different depending on whether the target is "in" or "out" because the muons undergo multiple and single Coulomb scattering in the target.

It is difficult to make this correction because the angular distribution of the beam is not known very well. Nevertheless, the correction is believed to be small, if not zero, for the partial corrections σ_4 through σ_8, which are the only ones used to obtain the total cross section. In the first place, the number of muons relative to the number of pions is small, and secondly, because the muon mass $m_{\mu} = 105.66$ MeV is comparable to the pion mass $m_{\pi} = 139.57$,

the multiple and (to a lesser degree) single Coulomb scattering corrections are appreciable only for the partial cross sections σ_1, σ_2, and σ_3. However, these three σ_i's are not used to obtain σ_{TOT}.

The number of muons is small because of the effect of using the DISC and the time-of-flight counters. The principal source of muons is pions decaying slightly upstream of TOF2 and between TOF2 and the target. For 51 MeV pions, where the number of decaying pions is the largest, all muons from pion decays within 4 cm of the upstream face of TOF2 could be identified as pions. Furthermore, there is another 5.08 cm between TOF2 and the target where pions could decay. The probability of a 51 MeV pion decaying in this 9.08 cm is approximately 1%, which decreases at higher energies.

As a result of these considerations, no corrections were made to the σ_i for upstream pion decays.

Next, consider the effect of muons from pions decaying downstream of the target. They do not always hit the same transmission counter that their parent pion would have hit had it not decayed. This makes the measured partial cross section for that counter too large. This effect would cancel in the comparison between target "in" and "out" runs if there were no energy loss of scattering of pions in the target. The effect of energy loss on the angular distribution of the decay muons may be seen from the expression for the maximum decay angle θ_{max} (as measured from the pion's trajectory) in the laboratory frame

$$\tan\theta_{max} = \left[\frac{1-\beta_\pi^2}{\left(\frac{\beta_\pi^2}{\beta_\mu^2}\right)-1}\right]^{\frac{1}{2}} , \qquad (89)$$

where β_π and β_μ are the pion velocity (as measured in the laboratory) and muon velocity (as measured in the pion's rest frame), respectively. If $\beta_{0\pi}$ (β_π) and θ_{0max} (θ_{max}) are for a blank (target) run then $\beta_{0\pi} > \beta_\pi$ and $\theta_{0max} < \theta_{max}$.

The formalism used to treat the pion decay correction was due to and developed by G. Burleson.[41] It starts by considering the i-th transmission counter, which measures S_i counts of which S_i^μ counts are due to muons. If S_i^μ can be calculated or measured then the number of pions detected is $S_i^\pi = S_i - S_i^\mu$. This number must be corrected for the number of pions that decayed before reaching the i-th counter. To do this, consider a single pion which travels a distance x before reaching the transmission stack. The probability that it did not decay is $\exp(-x/\lambda)$, where λ is the decay length. For the j-th pion traveling a distance x_{ij} before reaching the i-th transmission counter, the probability that it will not decay is $\exp(-x_{ij}/\lambda)$. To correct S_i^π for those pions that decayed, it should be divided by $\langle\exp(-x_{ij}/\lambda)\rangle$, the average probability that a pion will not decay before reaching the i-th counter. The average is taken over the x_{ij}/λ for the sample of pions S_i^π.

If S_i^μ was known, then the partial cross section σ_i would be given by

$$\sigma_i = \frac{1}{nt}\ln\left[\left(\frac{S_{i0} - S_{i0}^\mu - S_{i0}^\nu}{S_i - S_i^\mu - S_i^\nu}\right)\left(\frac{Y}{Y_0}\right)\left(\frac{\left\langle\exp\left(\frac{-x_{ij}}{\lambda_0}\right)\right\rangle}{\left\langle\exp\left(\frac{-x_{ij}}{\lambda}\right)\right\rangle}\right)\right] , \qquad (90)$$

where S_i^{ν} is the number of muons from pions decaying upstream of the target. Since $S_i^{\nu} \ll S_i^{\mu}$, equation (90) may be written as

$$\sigma_i = \frac{1}{nt} \ln \left[\frac{\left(\frac{S_{i0}}{Y_0} \right)}{\left(\frac{S_i}{Y} \right)} \right] + \frac{1}{nt} \ln \left[\left(\frac{\left(1 - \frac{S_{i0}^{\mu}}{S_{i0}} \right)}{\left(1 - \frac{S_i^{\mu}}{S_i} \right)} \right) \left(\frac{\left\langle \exp\left(\frac{-x_{ij}}{\lambda_0} \right) \right\rangle}{\left\langle \exp\left(\frac{-x_{ij}}{\lambda} \right) \right\rangle} \right) \right] . \quad (91)$$

The first term in equation (91) is the partial cross section calculated from the measured S_i and S_{i0} and the second term is the correction for decay σ_{Di}

$$\sigma_{Di} = \frac{1}{nt} \ln \left[\left(\frac{1 - \frac{S_{i0}^{\mu}}{S_{i0}}}{1 - \frac{S_i^{\mu}}{S_i}} \right) \left(\frac{\left\langle \exp\left(\frac{-x_{ij}}{\lambda_0} \right) \right\rangle}{\left\langle \exp\left(\frac{-x_{ij}}{\lambda} \right) \right\rangle} \right) \right] . \quad (92)$$

A Monte Carlo computer program was used to calculate S_{i0}^{μ}, S_i^{μ}, $\left\langle \exp\left(\frac{-x_{ij}}{\lambda_0} \right) \right\rangle$, and $\left\langle \exp\left(\frac{-x_{ij}}{\lambda} \right) \right\rangle$. The calculation is discussed in Appendix E. However, it should be noted that the effects of the finite beam size and divergence are included in this calculation. Furthermore, the downstream decays come from both scattered and unscattered pions when the target is "in" or "out" (when the target is "out" pions still scatter in TOF2). Since the distribution of scattered pions was not known, the observed distribution (which included both pions and muons) was used to approximate it.

The downstream pion decay correction varied from ~12% correction at 51 and 61 MeV to ~4% correction at 105 MeV. This correction could vary by as much as ±3% at 51 and 61 MeV and by ±1% at 105 MeV, depending upon the assumed form of the tails of the angular

distribution at the target. In addition, an estimate of the statistical error in the calculation was made with the use of the binomial and normal distributions. This error was added in quadrature to the statistical errors $\Delta\sigma_i$ of the σ_i before extrapolating to t=0. The statistical error in the decay corrections σ_{Di} was between 1/4 and 1/3 of the statistical error in σ_i.

Coulomb-Nuclear Interference

The next correction to be considered is the interference of the Coulomb and nuclear elastic amplitudes. The $\sigma(\Omega)$ are corrected for this effect by subtracting $\int_{\Omega}^{4\pi} \left(\frac{d\sigma}{d\Omega}\right)_{cn} d\Omega$ from $\sigma(\Omega)$ as shown in equation (17), where $\left(\frac{d\sigma}{d\Omega}\right)_{cn}$ is given by equation (14) to be

$$\left(\frac{d\sigma}{d\Omega}\right)_{cn} = 2[\mathrm{Re}\, f_n \,\mathrm{Re}\, f_c + \mathrm{Im}\, f_n \,\mathrm{Im}\, f_c] \quad . \tag{93}$$

Because it contains the nuclear amplitude f_n, this correction is model-dependent. It could be made model-independent by measuring the Coulomb-nuclear interference directly. This has been done for ^{12}C by Binon et al.[42] and Scott et al.[43] and for ^{16}O by Mutchler et al.[44] at a few energies, but no data exist for ^{4}He. To measure the interference effect, the elastic differential cross section needs to be measured at small angles, where the two amplitudes f_n and f_c become comparable in magnitude.

An alternate approach for self-conjugate nuclei is to calculate the average cross section $\bar{\sigma} = \frac{1}{2}(\sigma_{TOT}^{-} + \sigma_{TOT}^{+})$ and the cross section

difference $\Delta\sigma = (\sigma^-_{TOT} + \sigma^+_{TOT})$ without making the interference correction, where σ^-_{TOT} and σ^+_{TOT} are the σ^- and σ^+ total nuclear cross sections, respectively. To first order, $\bar{\sigma}$ is independent of the Coulomb-nuclear interference correction and can give a reasonable estimate of the strong total cross section. The difference $\Delta\sigma$ is independent of the pure Coulomb correction and shows the combined effects of Coulomb distortion and Coulomb-nuclear interference. Finally, if some reasonable estimate of the interference correction could be made to σ^-_{TOT} and σ^+_{TOT}, then the ratio $\Delta\sigma/\sigma$ could yield information concerning the Coulomb distortion effects.

To see why $\bar{\sigma}$ is nearly independent of the interference correction for low-Z self-conjugate nuclei, consider equation (93). The Coulomb amplitude f_c is mostly real (i.e., $\mathrm{Re}\, f_c \gg \mathrm{Im}\, f_c$), so that

$$\left(\frac{d\sigma}{d\Omega}\right)_{cn} = 2\,\mathrm{Re}\, f_c\, \mathrm{Re}\, f_n \quad .$$

The sign of $\mathrm{Re}\, f_c$ is negative (positive) for π^+ (π^-) and $\mathrm{Re}\, f_n$ has the same sign for both π^+ and π^-, being positive (negative) for energies below (above) the (3,3) resonance. This means that the interference corrections for π^+ and π^- are nearly equal in magnitude and of opposite sign.

Models may be invoked to calculate the Coulomb-nuclear interference correction. Those that were used in this work belong to the class of complex optical potentials. In this type of model,

the many-body problem of the pion-nucleus interaction is turned into a two-body problem of the pion interacting with a potential. The various interactions between the pion and the nucleons in the nucleus are replaced by a potential V, between the pion and the nucleus, which has both a real and an imaginary part to account for both elastic and inelastic processes.

The calculations were made using a computer program called PIRK, which is documented in papers by Eisenstein and Miller[45] and by Cooper and Eisenstein.[46] PIRK solves the problem of a relativistic spinless particle interacting with a complex potential. It numerically integrates the Klein-Gordorn equation

$$[-(\hbar c\nabla_r)^2 + \frac{c^2\hat{L}^2}{r^2} + (m_0c^2)^2]\psi = [E - 2V_c^2 - 2EV_N]\psi \ , \quad (94)$$

where ∇_r is the radial part of the gradient operator, $\hat{L}^2$ is the operator for the square of the orbital angular momentum, m_0 is the rest mass of the pion, ψ is the pion wave function, E is the total energy, V_c is the Coulomb potential energy, and V_N is the complex optical nuclear potential. The Klein-Gordon equation is numerically integrated for each partial wave from the origin outwards to a predetermined match point where the "internal" logarithmic derivative is compared to the "external" or asymptotic Coulomb wave function for that particular partial wave. The phase shifts are obtained for each partial wave and are used to calculate the scattering amplitude, the differential elastic cross section, the interference between f_c and f_n, and the total cross section. The equations used are

$$\frac{d\sigma}{d\Omega} = |f_c(\theta) + f_n(\theta)|^2 \quad , \tag{95}$$

$$f_c(\theta) = \eta[2p \sin \frac{\theta}{2}]^{-1} e^{2i(\sigma_0 - \eta \ln(\sin \theta/2))} \quad , \tag{96}$$

$$\eta = \frac{z_\pi z_N \alpha E}{p} \quad ,$$

$$f_N(\theta) = \frac{i}{2k} \sum_\ell (2\ell + 1) S_{c\ell} (1 - S_{N\ell}) P_\ell(\cos \theta) \quad , \tag{97}$$

$$S_{c\ell} = e^{2i\sigma_\ell} \quad , \tag{98}$$

$$S_{N\ell} = e^{2i\delta_{N\ell}} \quad , \tag{99}$$

and

$$\sigma_{TOT} = \frac{2\pi}{k^2} \sum_\ell (2\ell + 1) \, \mathrm{Re}(1 - S_{N\ell}) \quad , \tag{100}$$

where θ, E, p, and k are the center-of-mass scattering angle, total energy, momentum, and wave number of the pion, δ_ℓ is the nuclear phase shift for the ℓ-th partial wave in the presence of the Coulomb field, σ_ℓ is the point charge Coulomb phase shift of the ℓ-th partial wave, and α is the fine structure constant.

Using equations (96) through (99), the interference correction was found by numerically integrating equation (14) from Ω_i to 4π, where Ω_i is the solid angle subtended by the i-th transmission counter.

The optical potentials used in the Klein-Gordorn equation were the Kisslinger and Laplacian potentials, which are given by

$$V_N\psi = -A[b_0k^2\rho\psi - b_1\nabla\cdot(\rho\nabla\psi)] \tag{101}$$

and

$$V_N\psi = -A[(b_0 + b_1)k^2\rho\psi + \tfrac{1}{2}b_1(\nabla^2\rho)\psi] \quad , \tag{102}$$

respectively. In equations (101) and (102), A is the nuclear mass, k is the pion wave number in the π-nucleus center-of-mass frame, ρ is the nuclear density, and b_0 and b_1 are complex parameters. The models are discussed in the papers by Kisslinger[47] and in the papers by Lee and McNanus,[48] Faldt,[49] and Kock and Fernheim.[50]

Both of these models are attempts to describe the (3,3) resonance with essentially only the S- and P-waves contributing to the interaction. The parameters b_0 and b_1 give the strength of the S- and P-wave contributions to the interaction, respectively. One major difference between the two potentials is that the Laplacian potential is local (i.e., it is a function of only the position operator), whereas the Kisslinger potential is nonlocal. This difference arises from the assumed form of the off-shell pion-nucleon scattering matrix, which is not unique.

In solving the Klein-Gordorn equation, a Gaussian charge distribution was used to calculate the Coulomb potential. It was given by

$$\rho_c(r) = \frac{2e^2}{(\pi R_c)^3}\, e^{-(r/R_c)^2} \tag{103}$$

for $r < R_c$, where R_c is the charge radius of the nucleus divided by $A^{1/3}$. The corresponding potential at some point $R > R_c$ is

$$\phi(R) = \frac{ze^2}{R} \operatorname{erf}\left(\frac{-r^2}{R_c}\right) \quad . \tag{104}$$

The nuclear matter distribution used in equations (101) and (102) was also Gaussian and was given by

$$\rho_N(r) = \frac{2}{z(\pi w)^3} e^{-(r/w)^2} \quad , \tag{105}$$

where z is the charge of the nucleus and w is the width parameter for the nuclear matter density.

It is desired to apply these models to the total cross section data for $\pi^{\pm}$ - ^{4}He in an energy range where they are not expected to work especially well. This was demonstrated by Cooper and Eisenstein[51] when they used the Kisslinger and Laplacian models to analyze data from π^+ elastic scattering on ^{12}C and both π^+ and π^- elastic scattering on ^{4}He at 50 MeV. They allowed the complex parameters b_0 and b_1 to vary in both the Kisslinger and Laplacian potentials to obtain good fits to the data. The fits they obtained were found to be unsatisfactory because the resulting potentials either violated unitarity (by causing one or more scattering matrix elements to have magnitude greater than unity) or produced pions in an unphysical way in some regions of the nucleus. However, there are few options, since at present there do not exist any models which have been shown to be applicable in this energy regime.

As a limited check of the sensitivity of the models to the parameters b_0 and b_1, they were chosen in two different ways. In one case they were an interpolation or extrapolation of the values obtained by Crowe et al.[52] which were obtained by treating them

as free parameters to obtain the best fit of the Kisslinger potential to the elastic differential cross sections for π^+ and π^- on ^{4}He (at 51, 60, 68, and 75 MeV). In the other case, the values of b_0 and b_1 were obtained from a fit to the free pion-nucleon phase shifts by Saloman.[53] Both sets of b_0 and b_1 are given in Table X as a function of the pion kinetic energy T_π.

As can be seen from Table X, there is a considerable difference in the two sets of parameters. Also, as was expected, the Coulomb-nuclear interference correction and, consequently, the total cross section are dependent both on the model used and on the parameters b_0 and b_1. The variation in the size of the correction at 51 MeV and 105 MeV is shown in Table XI. The total cross sections obtained from the two models and two sets of parameters will be given in Chapter V.

Table X. The parameters b_0 and b_1, as a function of the pion kinetic energy T_π, from the fits by Crowe et al. (Ref. 52) and Saloman (Ref. 53).

	Crowe et al.				Saloman			
T_π (MeV)	Re b_0	Im b_0	Re b_1	Im b_1	Re b_0	Im b_0	Re b_1	Im b_1
51	-2.8739	0.0788	5.8342	0.0443	-1.1303	0.6007	7.5302	0.9448
71	-2.5558	0.2054	6.0012	0.2808	-1.0704	0.5467	7.7425	1.3156
75	-2.1296	0.5864	6.2250	0.5979	-1.0094	0.4946	8.0334	1.9516
85	-1.8083	0.8736	6.3936	0.8368	-0.9721	0.4657	8.2329	2.5611
95	-1.4861	1.1616	6.5628	1.0765	-0.9395	0.4430	8.3811	3.3075
105	-1.1584	1.4544	6.7348	1.3202	-0.9095	0.4247	8.4267	4.2216
144	-0.0890	2.5692	7.3897	2.2479	-0.8091	0.3815	6.1695	8.5663

Table XI. The size of the Coulomb-nuclear interference correction for 51 and 105 MeV pions. The abbreviations KC and LC refer to the Kisslinger and Laplacian potentials using the parameters b_0 and b_1 as obtained from the work of Crowe et al. (Ref. 52) and KS and LS refer to the same two models using values of b_0 and b_1 obtained from the work of Saloman (Ref. 53).

Model	T = 51 MeV	T = 105 MeV
	% Correction	% Correction
KC	7.1	6.2
LC	7.9	7.2
KS	9.5	1.9
LS	14.1	6.5

Energy of the Pion Beam

The pion kinetic energies quoted in this work are the mean kinetic energies of the pion beam at the center of the target. They were determined by calculating the mean energy loss of the pion beam along its path from the exit of the LEP channel to the center of the target.

The mechanism for energy loss is the excitation and ionization of the atoms and molecules in the different materials along the flight path of the pions. The energy loss per unit length (or stopping power) $\frac{1}{\rho}\frac{dT}{dX}$ for each material was calculated from the relativistic Bethe formula[54]

$$\frac{1}{\rho}\frac{dT}{dX} = \frac{2\pi N_0 z_1^2 e^4}{mc^2\beta^2}\ \frac{z_2}{A}\left[\ln\left(\frac{2mc^2\ W}{I_{adj}^2(1-\beta^2)}\right) - 2\beta^2 - 2\left(\frac{\Sigma C_i}{z_2}\right) - \Delta\right] \tag{106}$$

where W is the maximum kinetic energy which can be transferred to an electron (initially at rest) and is given by

$$W = \left(\frac{2mc^2\beta^2}{1-\beta^2}\right)\left(1 + \frac{2m}{M(1-\beta^2)} + \left(\frac{m}{M}\right)\right)^{-1} \qquad (107)$$

In equations (106) and (107), the meanings of the symbols are as follows:

ρ = mass density of the stopping material,

T = pion kinetic energy,

X = thickness of the stopping material in mass per unit area,

z_1 = charge of the pion,

c = velocity of light in vacuum,

e = electronic charge in esu,

m = electron rest mass,

A = atomic weight of the stopping material,

N_0 = Avogadro's number,

z_2 = charge of the stopping material,

I_{adj} = adjusted ionization of the stopping material,

β = velocity of the incident pion,

ΣC_i = sum of the effects of shell corrections on the stopping power,

Δ = polarization effect correction term,

and

M = pion rest mass.

The polarization effect Δ is the perturbation of the field of the passing pion, which is caused by the electric polarization of the

surrounding atoms. This results in a reduction of the energy loss by the pion. This was assumed to be small, and Δ was set equal to zero. The $\sum_i C_i$ contains the effects of nonparticipating inner shell electrons. It was also assumed to be small and was set equal to zero.

The principal uncertainty in the kinetic energy of the pion was due to the momentum bite $\Delta P/P$ of the LEP channel. This was typically $\pm 1\%$ or $\pm 2\%$.

Summary of Data Corrections

Table XII lists all of the major data corrections, with the approximate size of each. The remaining corrections to the data were estimated to be less than 1%. These include multiple Coulomb scattering, pion decay (upstream), effects due to the geometry of

Table XII. The major corrections to the data with the size of each.

Correction	Size of Correction
Accidentals	0.1 to 3.0%
Efficiencies and Absorption	0.1 to 0.5%
Single Coulomb	1.5 to 10.0%
Pion Decay (Downstream)	4.0 to 12.0%
Coulomb-Nuclear Interference	6.2 to 14.1%

the detection system (i.e , positioning of the transmission stack, TOF2, and the halo counters), effects due to the target thickness, effects due to the finite beam size and divergence, knock-out protons, and effects due to the incorrect identification of pions by the DISC and time-of-flight system.

V. RESULTS AND DISCUSSION

The $\pi^{\pm}$-^{4}He total cross sections measured in this experiment will be presented in this chapter, along with previous measurements made in the same energy region. A discussion of how the measured total cross section is related to the imaginary part of the forward elastic scattering amplitude through a modified optical theorem will also be given. The real part of the forward scattering amplitude is obtained with the use of a phenomenological model and is compared to forward dispersion relation calculations. The measured total cross sections are compared to the predictions of several optical model calculations. Lastly, the chapter is concluded by a summary of what has been found and what could be done in the future to extend this work.

Pion-^{4}He Total Cross Section

In measuring the strong interaction total cross section for pion-^{4}He scattering, the emphasis was on low-energy data with small statistical errors for both positively- and negatively-charged pions. Here, low energy means pion laboratory kinetic energies below 100 MeV. It is desirable to have both π^+ and π^- data in order to have a better means of studying the Coulomb problems discussed in Chapter IV.

There is a scarcity of low-energy data for the π-nucleus total and elastic differential cross sections. This scarcity of data is attributable to the low-intensity pion beams that have been available at low energies. The data which does exist is for the nuclei ^{12}C and

^{4}He. The choice of these low Z targets is due to the Coulomb problems which are increasing as the energy is decreasing. Only the ^{4}He data will be considered in the present work.

The $\pi^{\pm}$-^{4}He elastic differential cross section $d\sigma/d\Omega$ comes from three experiments. Crowe et al.[52] measured $d\sigma/d\Omega$ for both $\pi^{\pm}$ at energies of 51, 60, 68, and 75 MeV. Nordberg and Kinsey[55] measured $d\sigma/d\Omega$ for both $\pi^{\pm}$ at 24 MeV. These two experiments were counter experiments. The third measurement was a bubble chamber experiment by Bloch et al.[56] who also measured the total cross section. They obtained data for both $\pi^{\pm}$ at 50, 58, and 65 MeV. Their quoted energies are the mean values of the three energy intervals into which their experiment was divided. These three energy regions were: (a) 45 to 55 MeV, (b) 55 to 62 MeV, and (c) 62 to 69 MeV. Consequently their energy resolution was not particularly good. The total cross section data of Bloch et al.[56] is presented in Table XIII. The table gives the π^+-^{4}He total cross section σ^+_{TOT}, the π^--^{4}He total

Table XIII. The $\pi^{\pm}$-^{4}He total cross section data of Bloch et al. (Ref. 56).

T_π(MeV)	σ^+_{TOT} (mb)	σ^-_{TOT} (mb)	$\Delta\sigma$ (mb)	$\bar{\sigma}$ (mb)	$\frac{\Delta\sigma}{\sigma}$
51	79.2 ± 3.4	91.1 ± 4.7	11.9 ± 5.8	85.2 ± 2.9	0.14 ± 0.07
58	80.1 ± 3.0	109.2 ± 4.5	29.1 ± 5.4	94.7 ± 2.7	0.31 ± 0.06
65	106.8 ± 4.4	127.6 ± 5.8	20.8 ± 7.3	117.2 ± 3.6	0.18 ± 0.06

cross section σ_{TOT}^{-}, the cross section difference $\Delta\sigma = \sigma_{TOT}^{-} - \sigma_{TOT}^{+}$, the average cross section $\bar{\sigma} = \frac{1}{2}(\sigma_{TOT}^{-} + \sigma_{TOT}^{+})$, and the ratio $\Delta\sigma/\sigma$ as a function of the pion laboratory kinetic energy T_{π}.

Finally, Fowler et al.[57] measured the average total cross section $\bar{\sigma}$ at 60 and 105 MeV in a ^{4}He diffusion cloud-chamber experiment. At 60 and 105 MeV $\bar{\sigma}$ was 89 ± 18 mb and 207 ± 27 mb, respectively. The 60 MeV data was an average of data taken at 53 and 68 MeV.

These experiments were all attempts to measure the rms electromagnetic radius of the pion. The results on the magnitude of this radius were all greater than those obtained from experiments involving the scattering of pions from atomic electrons.[39] The analysis of the π-^{4}He data was based upon the use of π-nucleus optical potentials to fit the data. As will be seen later, there is very poor agreement between the different optical potentials and both their experimental data and the results of this experiment. Consequently, until such time as there is an improved agreement between theory and experiment, $\pi^{\pm}$-^{4}He scattering experiments are unlikely to yield reasonable values for the rms electromagnetic radius of the pion.

Recently, Alexandrov et al.[58] measured the elastic differential cross section for $\pi^{\pm}$ on ^{4}He and ^{3}He at nine energies with the lowest two being 68 and 98 MeV. In addition, Binon et al.[59] in a counter experiment measured the π^{-}-^{4}He total cross section at eleven energies and the π^{+}-^{4}He total cross section at one energy. Only three of these energies (67, 85, and 110 MeV) are in the energy region of interest here. Lastly, Wilkin et al.[8] measured the average $\pi^{\pm}$-^{4}He total cross section $\bar{\sigma}$ at five energies, with the lowest being 110 MeV.

The motivation for this experiment was a desire to improve on the earlier $\pi^{\pm}$-^{4}He total cross section data and to examine the poor agreement in π-nucleus scattering between theory and experiment in the low-energy region. A discussion of the discrepancy between theory and experiment will be given later, along with a survey of the growing literature on the problem. The present experiment measured $\pi^{\pm}$-^{4}He total cross sections in the energy range 50 to 105 MeV, in steps of approximately 10 MeV.

This experiment is an improvement over the earlier σ_{TOT} experiments of Bloch et al.[56] and Fowler et al.,[57] in that it has better energy or momentum resolution (i.e., $\Delta P/P$, where P is the momentum, was typically ±1% or ±2%). The final statistical errors were between 3 and 6%, which are comparable to those of Bloch et al.[56] and considerably smaller than those of Fowler et al.[57] Furthermore, this experiment covered a wider energy range than the two previous measurements of σ_{TOT}.

The π^+-^{4}He and π^--^{4}He total cross sections (σ^+_{TOT} and σ^-_{TOT}, respectively) measured in this experiment are presented with their statistical errors in Table XIV as a function of the mean pion laboratory kinetic energy T_π at the center of the target. These total cross sections were obtained, as discussed earlier, by the following procedure: (1) The measured partial cross sections $\sigma(\Omega)$ were corrected for those effects discussed in Chapter IV (i.e., pion decay, single Coulomb scattering, Coulomb-nuclear interference, etc.); (2) The corrected partial cross sections were then fitted with a

Table XIV. The $\pi^{\pm}$-^{4}He total cross sections of this experiment as a function of T_π, the pion laboratory kinetic energy. The reduced chi-squared χ_R^2 is also given. The cross sections are in mb and T_π is in MeV. The errors are the statistical errors. Fitted parameters and free parameters refer to the values of b_0 and b_1 obtained from the fits of Crowe et al. (Ref. 52) and Saloman (Ref. 53) (see Table X).

No Coulomb-Nuclear Interference Correction

T_π	σ^+_{TOT}	χ_R^2	σ^-_{TOT}	χ_R^2
51	95.6±5.9	1.0	125.5±6.1	1.8
61	86.0±6.0	2.0	127.6±6.3	0.3
75	124.2±7.5	1.4	162.2±7.0	1.8
85	127.1±6.4	0.7	185.4±6.4	1.9
95	161.3±6.4	0.1	210.2±6.4	3.1
105	187.1±5.7	0.3	223.9±6.1	1.1
144	295.3±4.0	0.2		

Interference Correction Using Kisslinger Model

	Fitted Parameters				Free Parameters			
T_π	σ^+_{TOT}	χ_R^2	σ^-_{TOT}	χ_R^2	σ^+_{TOT}	χ_R^2	σ^-_{TOT}	χ_R^2
51	105.1±5.9	1.1	114.8±6.1	1.7	109.2±5.9	1.1	112.4±6.1	1.6
61	95.8±6.0	2.0	117.1±6.3	0.2	98.0±6.0	2.1	116.4±6.3	0.2
75	135.1±7.5	1.4	150.9±7.0	1.9	133.8±7.5	1.4	153.5±7.0	1.9
85	138.9±6.4	0.8	173.3±6.4	1.8	134.9±6.4	0.8	178.4±6.4	1.9
95	173.9±6.4	0.1	197.4±6.4	2.9	167.3±6.4	0.1	204.9±6.4	3.0
105	200.3±5.7	0.3	210.8±6.1	1.0	191.5±5.7	0.3	220.2±6.1	1.1
144	305.0±4.0	0.2			293.9±4.0	0.2		

Interference Correction Using Laplacian Model

	Fitted Parameters				Free Parameters			
T	σ^+_{TOT}	χ_R^2	σ^-_{TOT}	χ_R^2	σ^+_{TOT}	χ_R^2	σ^-_{TOT}	χ_R^2
51	106.8±5.9	1.1	114.4±6.1	1.7	115.7±5.9	1.2	105.7±6.1	1.6
61	97.5±6.0	2.1	116.1±6.3	0.2	105.2±6.0	2.1	108.7±6.3	0.2
75	136.5±7.5	1.4	150.0±7.0	1.9	142.2±7.5	1.5	144.6±7.0	1.9
85	140.1±6.4	0.8	172.1±6.4	1.4	144.0±6.4	0.8	168.8±6.4	1.8
95	175.3±6.4	0.1	196.0±6.4	2.9	176.8±6.4	0.1	194.9±6.4	2.9
105	202.3±5.7	0.3	208.4±6.1	1.0	201.0±5.7	0.3	210.1±6.1	1.0
144	316.4±4.0	0.3			300.1±4.0	0.2		

quadratic polynomial in t (i.e., the square of the momentum transfer) using the correlated least-squares method; and (3) The fitted quadratic polynomial was then extrapolated to t=0 to obtain the total cross section. Only data from the five largest transmission counters were used in the fitting procedure. Data from the three smaller counters were omitted because of the uncertainties in correcting them for pion decay and single and multiple Coulomb scattering. For the fitting, the second-order polynomial in t (as opposed polynomials of the other order) in general had the smallest value of the reduced chi-squared χ_R^2 (i.e., the value of chi-squared per degree of freedom). For this reason the total cross sections were obtained using a quadratic polynomial in t as the fitting function. The χ_R^2 of the fit used to find each cross section is also given in Table IV. In Table XV, the cross section difference $\Delta\sigma$, the average cross section $\bar{\sigma}$, and the ratio $\Delta\sigma/\sigma$ are given as a function of the mean pion laboratory kinetic energy T_π at the center of the target.

It should be noted that in Tables XIV and XV there appear five sets of cross sections These contain all of the corrections to the data described in Chapter IV, with the exception of the first set which gives the results without the Coulomb-nuclear interference correction. The remaining four sets contain an interference correction, which was calculated with the use of both the Kisslinger and the Laplacian optical potentials. These were both discussed in some detail in Chapter IV along with the procedure used to calculate the Coulomb-nuclear interference. In both of these models, there are two parameters b_0 and b_1 which give the strengths of the S- and

Table XV. The difference $\Delta\sigma$ in and average $\bar{\sigma}$ of σ^{+}_{TOT} and σ^{-}_{TOT} as function of T_π, the pion laboratory kinetic energy. The cross sections are in mb and T_π is in MeV. The errors are the statistical errors. Fitted parameters and free parameters refer to the values of b_0 and b_1 obtained from the fits of Crowe et al. (Ref. 52) and Saloman (Ref. 53).

No Coulomb-Nuclear Interference Correction

T_π	$\Delta\sigma$	$\bar{\sigma}$	$\Delta\sigma/\bar{\sigma}$
51	30.0± 8.5	110.5±4.3	0.27±0.08
61	41.6± 8.7	106.8±4.3	0.39±0.08
75	38.0±10.3	143.2±5.2	0.27±0.07
85	58.3± 9.1	156.2±4.5	0.37±0.06
95	49.0± 9.1	185.7±4.5	0.26±0.05
105	36.8± 8.3	205.5±4.2	0.18±0.04

Interference Correction Using Kisslinger Model

	Fitted Parameters			Free Parameters		
T_π	$\Delta\sigma$	$\bar{\sigma}$	$\Delta\sigma/\bar{\sigma}$	$\Delta\sigma$	$\bar{\sigma}$	$\Delta\sigma/\bar{\sigma}$
51	9.7± 8.5	110.0±4.3	0.09±0.08	3.2± 8.5	110.8±4.3	0.03±0.08
61	21.3± 8.7	106.5±4.3	0.20±0.08	18.4± 8.7	107.2±4.3	0.17±0.08
75	15.8±10.3	143.0±5.2	0.11±0.07	19.7±10.3	143.7±5.2	0.14±0.07
85	34.4± 9.1	156.1±4.5	0.22±0.06	43.5± 9.1	156.7±4.5	0.28±0.06
95	23.5± 9.1	185.7±4.5	0.13±0.05	37.6± 9.1	186.1±4.5	0.20±0.05
105	10.5± 8.3	205.6±4.2	0.06±0.04	28.7± 8.3	205.8±4.2	0.14±0.04

Interference Correction Using Laplacian Model

	Fitted Parameters			Free Parameters		
T_π	$\Delta\sigma$	$\bar{\sigma}$	$\Delta\sigma/\bar{\sigma}$	$\Delta\sigma$	$\bar{\sigma}$	$\Delta\sigma/\bar{\sigma}$
51	7.6± 8.5	110.6±4.3	0.07±0.08	-10.0± 8.5	110.7±4.3	-0.09±0.08
61	18.7± 8.7	106.8±4.3	0.18±0.08	3.6± 8.7	107.0±4.3	0.03±0.08
75	13.5±10.3	143.2±5.2	0.09±0.07	2.5±10.3	143.4±5.2	0.02±0.07
85	31.9± 9.1	156.1±4.5	0.21±0.06	24.9± 9.1	156.4±4.5	0.16±0.06
95	20.7± 9.1	185.6±4.5	0.11±0.05	18.1± 9.1	185.9±4.5	0.10±0.05
105	6.1± 8.3	205.3±4.2	0.03±0.04	9.1± 8.3	205.6±4.2	0.05±0.04

P-wave contributions to the pion-nucleus interaction. As a limited check of the sensitivity of these two optical potentials to b_0 and b_1 two sets of b_0 and b_1 were used in calculating the interference correction. As described in the discussion of the interference correction in Chapter IV, the first set used was the parameters obtained from the fits of Crowe et al.[52] and the second set was the free parameters derived from a fit to the free π-nucleon phase shifts made by Saloman.[53] Both sets of parameters were given in Table X. Of the four sets of cross sections in Tables XIV and XV with the interference correction, the first (second) two correspond to the use of the Kisslinger (Laplacian) optical potential with the fitted and free parameters.

To compare the results of this experiment to those of Bloch et al.,[56] Binon et al.,[59] and Wilkin et al.,[8] $\bar{\sigma}$, σ^{+}_{TOT}, and σ^{-}_{TOT} are plotted as a function of T_π in Figure 20, 21, and 22. The smooth curve in Figure 20 through the data from this experiment (i.e., the LAMPF data) is drawn to guide the eye.

The agreement among the data of the four experiments is not as good as one would like. In the case of $\bar{\sigma}$, there seems to be poor agreement among the 110 MeV data of Wilkin et al.,[8] and the 110 MeV and 105 MeV data of Binon et al.,[59] and the data of the present experiment, as well as between the 51 MeV data of Bloch et al.[56] and that of the present experiment (i.e., the systematic errors appear larger than the statistical errors). Although the data of Fowler et al.[57] was not included in Figure 20 because of its large statistical errors, it nevertheless agrees well with the data of this

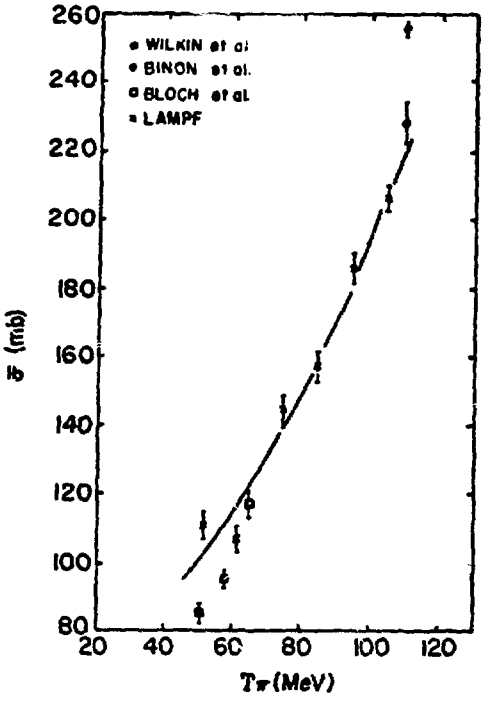

Figure 20. The average π-^{4}He total cross section $\bar{\sigma}$ versus the pion laboratory kinetic energy T_π. The data are from this experiment (LAMPF), Wilkin et al. (Ref. 8), Bloch et al. (Ref. 56), and Binon et al. (Ref. 59).

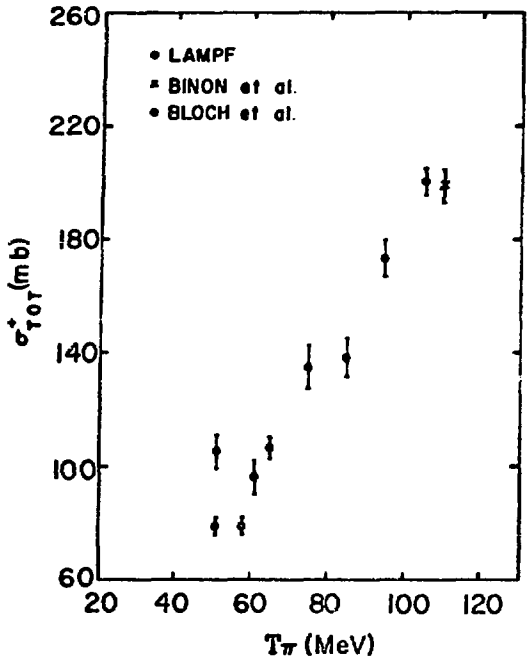

Figure 21. The π^+-^{4}He total cross section σ^+_{TOT} versus the pion laboratory kinetic energy T_π. The data are from this experiment (LAMPF), Bloch et al. (Ref. 56), and Binon et al. (Ref. 59).

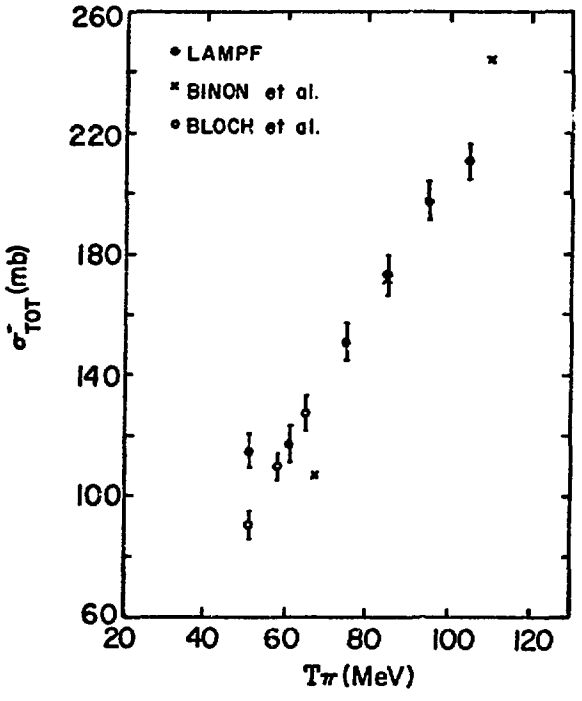

Figure 22. The π^--^{4}He total cross section σ^-_{TOT} versus the pion laboratory kinetic energy T_π. The data are from this experiment (LAMPF), Bloch et al. (Ref. 56), and Binon et al. (Ref. 59).

experiment. In the case of σ^{+}_{TOT} and σ^{-}_{TOT} the discrepancy in the data at low energies appear worse. This is indicative of the difficulty in measuring total cross sections at low energies. Many of the corrections to the data increase rapidly at these low energies.

It is preferable to compare the values of $\bar{\sigma}$ obtained from different experiments rather than the values of σ^{+}_{TOT} and σ^{-}_{TOT} because to first order $\bar{\sigma}$ is independent of the Coulomb-nuclear interference correction (this was discussed in Chapter IV.) This is important since the four experiments whose data are presented in Figures 21 and 22 have handled the interference correction in four different ways. The values of σ_{TOT} of this experiment shown in Figures 21 and 22 were corrected for Coulomb-nuclear interference by using the Kisslinger potential with the parameters b_0 and b_1 obtained from the work of Crowe et al.[52] This was felt to be the best combination of model and parameters to be used in the interference correction (at least in the energy region spanned by this experiment) since Crowe et al.[52] used the Kisslinger potential to fit their elastic differential cross sections in order to find b_0 and b_1.

The previous statement that $\bar{\sigma}$ is nearly independent of the Coulomb-nuclear interference correction is verified by the results of Table XV. In fact, $\bar{\sigma}$ is essentially the same whether or not the interference correction is made. When it is made, $\bar{\sigma}$ is independent of which optical potential is used or which set of b_0 and b_1 parameters is used. This is a stringent test of this independence from the interference correction since the Kisslinger and Laplacian are quite different, as are the two sets of parameters b_0 and b_1. In

comparison, the values of σ^{+}_{TOT} and σ^{-}_{TOT} vary by a few percent, depending upon the choice of parameters and model used for the interference correction, as may be seen in Table XIV. Thus σ^{+}_{TOT} and σ^{-}_{TOT} are much more model-dependent than $\bar{\sigma}$.

The total cross section σ^{+}_{TOT} was measured at 144 MeV to compare with the data from total cross section measurements at higher energies. To make this comparison, a Coulomb-nuclear interference correction must be made. Because this energy is so much greater than those in the experiment of Crowe et al.,[52] the values of b_0 and b_1 extrapolated from their work are probably not too reliable. The value of σ^{+}_{TOT} obtained using the Kisslinger model with the free parameters to calculate the interference correction was felt to be the best. The Laplacian model with the free parameters was considered less reliable than the Kisslinger model since it led to σ^{+}_{TOT} being greater than σ^{-}_{TOT} at 51 MeV. Aside from disagreeing with the data of Bloch et al.,[56] this was contrary to what is expected. According to an argument due to Faldt and Pilkuhn[60,61] one should have $\sigma^{+}_{TOT} < \sigma^{-}_{TOT}$. This is because a π^{+} (π^{-}) will be repelled (attracted) by the Coulomb field of the nucleus. Hence a π^{-} will have a greater probability than a π^{+} of strongly interacting with the nucleus because of its smaller impact parameter and higher energy, and therefore will have a larger cross section. This effect will be discussed later in greater detail. At any rate, the 144 MeV result of $\sigma^{+}_{TOT} = 293.9 \pm 4.0$ mb is consistent with σ^{-}_{TOT} results of Binon et al.[59] at 130 and 150 MeV, which are 292 and 320 mb, respectively. However, it agrees poorly with $\bar{\sigma} = 336 \pm 1$ mb at 146 MeV from the work of Wilken et al.[8]

The data from Bloch et al.,[56] Binon et al.[59] (at 110 MeV), and the present experiment all show $\sigma_{TOT}^{-} > \sigma_{TOT}^{+}$ for ^{4}He. This result has also been seen for the self-conjugate nucleus ^{12}C both in this experiment and in the experiments of Clough et al.[62] and of Carroll et al.[9] The data for ^{12}C were taken principally at energies greater than 100 MeV.

The data from this experiment will be compared to the predictions of several models in a later section in this chapter.

Discussion of the Optical Theorem

The nuclear total cross section $\sigma_{TOT}^{'}$ and the imaginary part of the forward nuclear elastic scattering amplitude Im f'(0°) are related through the optical theorem. This relationship is given by

$$\sigma_{TOT}^{'} = \frac{4\pi}{k} \text{Im } f'(0°) \quad , \tag{108}$$

where k is the pion wave number. The optical theorem is independent of any assumptions about the particular model used to describe the strong interaction.[63,64] This makes it useful because through it the measured total cross section provides a constraint on the analysis of elastic scattering data.

If, in pion-nucleus scattering experiments, one could use π^{0} rather than π^{+} or π^{-}, then the Coulomb interaction would be absent and $\sigma_{TOT}^{'}$ would be directly measurable as would the nuclear elastic differential cross section $d\sigma'/d\Omega = |f'(\theta)|^{2}$. With the assumption that the nuclear interaction can be represented by a spherically

symmetric potential, the nuclear elastic scattering amplitude $f'(\theta)$ has the following partial wave expansion

$$f'(\theta) = \frac{1}{2ik} \sum_{\ell=0}^{\infty} (2\ell + 1) \left[e^{2i\delta_\ell'} - 1 \right] P_\ell(\cos\theta) \qquad (109)$$

$$= \frac{1}{2ik} \sum_{\ell=0}^{\infty} (2\ell + 1)(S_\ell' - 1) p_\ell(\cos\theta) \quad , \qquad (110)$$

where δ_ℓ' are the complex nuclear phase shifts, P_ℓ are the Legendre polynomials of order ℓ, and $S_\ell' = \exp(2i\delta_\ell')$ are the matrix elements of the scattering matrix. Without invoking the optical theorem, one can write the total cross section σ_{TOT}' as

$$\sigma_{TOT}' = \frac{2\pi}{k^2} \sum_{\ell=0}^{\infty} (2\ell + 1)(1 - \mathrm{Re}\, S_\ell') \quad . \qquad (111)$$

Equations (110) and (111) satisfy the optical theorem.

If the pion-nucleus total cross section and elastic differential cross section are measured using charged pions, then one does not obtain σ_{TOT}' and $\frac{d\sigma'}{d\Omega}$. Instead, one obtains σ_{TOT} and $\left(\frac{d\sigma}{d\Omega}\right)_{el}$ which are determined by both the Coulomb and nuclear interactions. The full elastic scattering amplitude is not $f'(\theta)$, but rather $f(\theta)$, where

$$f(\theta) = f_c(\theta) + f_n(\theta) \quad . \qquad (112)$$

Here, $f_c(\theta)$ is the pure Coulomb elastic scattering amplitude and the residual amplitude $f_n(\theta)$ is the Coulomb distorted nuclear elastic scattering amplitude. In equations (13) and (15), $\left(\frac{d\sigma}{d\Omega}\right)_{ne}$ and σ_{TOT} were defined to be

$$\left(\frac{d\sigma}{d\Omega}\right)_{ne} = |f_n(\theta)|^2$$

and

$$\sigma_{TOT} = \sigma_r + \int_0^{4\pi} |f_n(\theta)|\, d\theta \quad ,$$

where σ_r was the total nuclear reaction cross section.

Unlike σ'_{TOT} and $f'(\theta)$, which are related by the optical theorem, σ_{TOT} and $f_n(\theta)$ are not related by an optical theorem, as will be shown below. The purpose of this section is to find the appropriate elastic scattering amplitude which will be related to σ_{TOT} through an optical theorem. The formalism was originated and developed by M. Cooper.

If the nuclear interaction is assumed to be represented by a spherically-symmetric potential, then a partial wave expansion of $f(\theta)$ can be made,[46,65]

$$f(\theta) = \frac{i}{2k} \sum_{\ell=0}^{\infty} (2\ell + 1) \left(1 - e^{2i(\sigma_\ell + \delta_\ell)}\right) P_\ell(\cos\theta) \qquad (113)$$

or

$$f(\theta) = \frac{i}{2k} \sum_{\ell=0}^{\infty} (2\ell + 1) \left(\left(1 - e^{2i\sigma_\ell}\right) + e^{2i\sigma_\ell}\left(1 - e^{2i\delta_\ell}\right) P_\ell(\cos\theta)\right) , \qquad (114)$$

where σ_ℓ are the real Coulomb phase shifts and δ_ℓ are the complex nuclear phase shifts in the presence of the Coulomb field. It is important to note that the δ_ℓ are not equal to the δ_ℓ' phase shifts that would be obtained in the absence of the Coulomb field. The Coulomb amplitude $f_c(\theta)$ may also be expanded in terms of partial waves:

$$f_c(\theta) = \frac{i}{2k} \sum_{\ell=0}^{\infty} (2\ell + 1) \left(1 - e^{2i\sigma_\ell}\right) P_\ell(\cos\theta) \qquad (115)$$

From equations (115) and (113), the partial wave expansion of $f_n(\theta)$ is

$$f_n(\theta) = \frac{i}{2k} \sum_{\ell=0}^{\infty} (2\ell + 1) e^{2i\sigma_\ell} \left(1 - e^{2i\delta_\ell}\right) P_\ell(\cos\theta)$$

$$= \frac{i}{2k} \sum_{\ell=0}^{\infty} (2\ell + 1) e^{2i\sigma_\ell} (1 - S_\ell) P_\ell(\cos\theta) \quad , \tag{116}$$

where $S_\ell = \exp(2i\delta_\ell)$. With equations (115) and (116), σ_{TOT} can be written as

$$\sigma_{TOT} = \sigma_r + \frac{\pi}{k^2} \sum_{\ell=0}^{\infty} (2\ell + 1) |1 - S_\ell|^2 \quad . \tag{117}$$

It can be shown by using the conservation of the probability current density that σ_r is given by[64]

$$\sigma_r = \frac{\pi}{k^2} \sum_{\ell=0}^{\infty} (2\ell + 1)(1 - |S_\ell|^2) \quad , \tag{118}$$

so that

$$\sigma_{TOT} = \frac{\pi}{k^2} \sum_{\ell=0}^{\infty} (2\ell + 1)(1 - |S_\ell|^2 + |1 - S_\ell|^2)$$

$$= \frac{\pi}{k^2} \sum_{\ell=0}^{\infty} (2\ell + 1)(1 - \mathrm{Re}\, S_\ell) \quad . \tag{119}$$

From an examination of equations (116) and (119) one can see that

$$\sigma_{TOT} \neq \frac{4\pi}{k} \mathrm{Im}\, f_n(0^\circ) \quad . \tag{120}$$

If a new amplitude $\tilde{f}_n(\theta)$ is defined by

$$\tilde{f}_n(\theta) = \frac{i}{2k} \sum_{\ell=0}^{\infty} (2\ell + 1) \left(1 - e^{2i\delta_\ell}\right) P_\ell(\cos\theta)$$

or

$$\tilde{f}_n(\theta) = \frac{i}{2k} \sum_{\ell=0}^{\infty} (2\ell + 1)(1 - S_\ell)P_\ell(\cos\theta) \quad , \tag{121}$$

then it can be seen from this definition and equation (119) that σ_{TOT} and $\tilde{f}_n(\theta)$ satisfy an optical theorem

$$\sigma_{TOT} = \frac{4\pi}{k} \operatorname{Im} \tilde{f}_n(\theta) \quad . \tag{122}$$

Also, since σ_ℓ is real, then

$$\int_0^{4\pi} |f_n(\theta)|^2 \, d\Omega = \int_0^{4\pi} |f_n(\theta)|^2 \, d\Omega \tag{123}$$

so that

$$\sigma_{TOT} = \sigma_r + \int_0^{4\pi} |\tilde{f}_n(\theta)|^2 \, d\Omega \quad . \tag{124}$$

The $\pi^{\pm}$-nucleus total cross section σ_{TOT} does not satisfy an optical theorem with $f_n(\theta)$ but it does with the new amplitude $\tilde{f}_n(\theta)$. Unlike $f_n(\theta)$ which contributes to the measured pion-nucleus elastic differential cross section

$$\left(\frac{d\sigma}{d\Omega}\right)_{el} = |f_c(\theta) + f_n(\theta)|^2 \quad ,$$

$\tilde{f}_n(\theta)$ does not. However, the amplitude $\tilde{f}_n(\theta)$ should be calculable from any model of the nuclear interaction so that equation (122) provides a link between the models and σ_{TOT}.

Real Part of the Forward Nuclear Elastic Scattering Amplitude

In the last few years several attempts have been made to verify experimentally the forward dispersion relation calculations of the real part of the forward nuclear elastic scattering amplitude for pion-nucleon and pion-nucleus scattering. For pion-nucleon scattering, this work has been done principally by Foley et al.[66] and, for pion-nucleus scattering, the work has been done by Scott et al.,[43] Mutchler et al.,[44] and Binon et al.[42,59] To date the nuclei investigated include ^{12}C, ^{16}O, and ^{4}He (in the case of ^{4}He only π^- data has been used). In this work, the real part of the forward scattering amplitude for $\pi^{\pm}$-^{4}He scattering at 51, 60, 68, and 75 MeV is determined from experimental data using a phenomenological model. The results are compared to the predictions of two forward dispersion relation calculations.

These experiments are usually performed by measuring the elastic differential cross section $\left(\frac{d\sigma}{d\Omega}\right)_{el}$ in the angular region where the Coulomb-nuclear interference is appreciable. The ratio of the real to imaginary parts of the forward nuclear elastic scattering amplitude α is obtained by fitting the data with a phenomenological model of the strong amplitude f_s. This model contains two adjustable parameters α and R_s, where α is the above ratio and R_s is the radius of the strong interaction (it is believed that R_s is not too different from the charge radius R_c, which is known from electron scattering). The imaginary part of the forward scattering amplitude $\mathrm{Im}\, f_s(0°)$ is obtained from the measured total cross section σ_{TOT}. As shown in the

last section this is not strictly true for charged pions; however the discrepancy should be small for a low-Z nucleus like ^{4}He. Hence, by knowing α and $\mathrm{Im}\, f_s(0°)$, one can calculate $\mathrm{Re}\, f_s(0°)$.

The data are analyzed by assuming that the elastic differential cross section $\left(\frac{d\sigma}{d\Omega}\right)_{el}$ is given by equation (10),

$$\left(\frac{d\sigma}{d\Omega}\right)_{el} = |f_c + f_n|^2 \quad .$$

Next, the Coulomb distorted nuclear amplitude f_n is assumed to be given by

$$f_n = f_s \exp(-2i\phi) \quad , \tag{125}$$

where f_s is the strong amplitude and 2ϕ is a phase which includes the pure Coulomb phase and the relative phase between the two scattering amplitudes f_c and f_s. The pure Coulomb amplitude may be written as

$$f_c(t) = -2\eta \frac{k}{|t|} G(t) \quad , \tag{126}$$

with

$$\eta = \frac{z_\pi z \alpha}{\beta} \quad , \tag{127}$$

where k is the pion wave number (in fm $^{-1}$), t is the square of the momentum transfer (in fm^{-2}), η is the effective Coulomb coupling constant, z_π is the charge of the pion, z is the charge of the target nucleus, α is the fine structure constant, and $\beta = v/c$ is the velocity of the pion. Here, k and β are center-of-mass quantities. The charge form factor G(t) is assumed to be Gaussian and is given by

$$G(t) = \exp\left[-\frac{1}{6}(R_c^2 + R_\pi^2)|t|\right] \quad , \tag{128}$$

where $R_\pi = 0.8$ fm[8,39] and $R_c = 1.63$ fm[40] are the charge radii of the pion and the ^{4}He nucleus, respectively. The standard approach is to represent the strong amplitude $f_s(t)$ by a phenomenological model[42-44,66,71]

$$f_s = \frac{k\sigma_s}{4\pi}(i + \alpha(0°))\exp\left[-\frac{1}{6}R_s^2|t|\right] \tag{129}$$

$$= \mathrm{Im}\, f_s(t)(i + \alpha(0°)) \quad ,$$

where σ_s is the total cross section for the strong interaction, R_s is the strong interaction radius, and

$$\alpha(0°) = \frac{\mathrm{Re}\, f_s(0°)}{\mathrm{Im}\, f_s(0°)} \tag{130}$$

Some time ago, an estimate for the phase 2ϕ was made by Bethe.[67] This was later improved upon by West and Yennie[68] to be

$$2\phi = -2\eta \ln(\sin\tfrac{\theta}{2}) - \eta\int_{-4k^2}^{0}\frac{dt'}{|t' - t|}\left[1 - \frac{f_s(t')}{f_s(t)}\right] \quad , \tag{131}$$

where θ is the center-of-mass scattering angle. Equation (131) may be expanded as a power series in t, as done by Binon et al.:[59]

$$2\phi = -\eta\left[2\ln(\sin\tfrac{\theta}{2}) + c + \ln(4k^2\rho) - \sum_{n=1}^{\infty}\frac{(\rho|t|)^2}{n(n!)}\right] \quad , \tag{132}$$

where $c = 0.5772$ (Euler's constant) and ρ is given by

$$\rho = \frac{1}{6}(R_s^2 + R_\pi^2 + R_c^2) \quad . \tag{133}$$

The phase 2ϕ is small, being ~1° for the ^{4}He data analyzed in the present work. With equations (10), (125), (126), and (129), one can write

$$\left(\frac{d\sigma}{d\Omega}\right)^{\pm}_{el} = \left|\pm|\eta|\,\frac{2k}{|t|}G(t) + \frac{k\sigma_s}{4\pi}(i+\alpha)\exp\left(-\frac{1}{6}R_s^2|t|\right)\exp(-2i\phi^{\pm})\right|^2 \tag{134}$$

where $\left(\frac{d\sigma}{d\Omega}\right)^{\pm}_{el}$ refers to the $\pi^{\pm}$-nucleus elastic differential cross section.

Equation (134) is the basic equation which Scott et al.[43] used in fitting their π^+-^{12}C data, which Binon et al.[42,59] used in fitting their π^--^{4}He and π^--^{12}C data, and which Mutchler et al.[44] used in fitting their $\pi^{\pm}$-O^{16} data (they also used the cross section difference $D = \left(\frac{d\sigma}{d\Omega}\right)^{-}_{el} - \left(\frac{d\sigma}{d\Omega}\right)^{+}_{el}$ to fit their data). If one has both π^+ and π^- data that, rather than use equation (134) to fit the π^+ and π^- data separately, it is preferable to fit the ratio D/A where D is the cross section difference defined above and $A = \frac{1}{2}\left\{\left(\frac{d\sigma}{d\Omega}\right)^{-}_{el} + \left(\frac{d\sigma}{d\Omega}\right)^{+}_{el}\right\}$ is the average cross section. The advantages of doing this are that, first of all, D/A as calculated from the data will be independent of those experimental corrections that are common to both π^+ and π^-. Secondly, D/A, as calculated from equation (134), will be sensitive to $\alpha(0°)$ and at the same time insensitive to R_s. To see this, consider the expression for D and A obtained from equation (134)

$$D = \frac{2\alpha|\eta|k^2\sigma_s\cos 2\phi}{\pi|t|}\exp\left(-\frac{1}{6}(R_c^2 + R_\pi^2 + R_s^2)|t|\right), \tag{135}$$

or

$$D = 4f_c \cos 2\phi \, \mathrm{Re}\, f_s \tag{136}$$

and

$$A = \frac{2|\eta|k^2}{|t|} \exp\left(-\frac{1}{3}(R_c^2 + R_\pi^2)|t|\right) + \frac{k\sigma_s^2}{4\pi}(1+\alpha^2) \exp\left(-\frac{1}{3}R_s^2|t|\right) \tag{137}$$

or

$$A = |f_c|^2 + |f_s|^2 \quad . \tag{138}$$

Using equations (135) and (136), one can write

$$\frac{D}{A} = \frac{\dfrac{2\alpha|\eta|k^2\sigma_s \cos 2\phi}{\pi|t|} \exp\left(-\frac{1}{6}(R_c^2 + R_\pi^2 + R_s^2)|t|\right)}{\dfrac{2|\eta|k^2}{|t|} \exp\left(-\frac{1}{3}(R_c^2 + R_\pi^2)|t|\right) + \dfrac{k\sigma_s}{4\pi}(1+\alpha^2) \exp\left(-\frac{1}{3}R_s^2|t|\right)} \tag{139}$$

or

$$\frac{D}{A} = \frac{4f_c \cos 2\phi \, \mathrm{Re}\, f_s}{|f_c|^2 + |f_s|^2} \quad . \tag{140}$$

From equations (137) and (135) it can be seen that D is directly proportional to α while D/A is not. However, because R_s and R_c are not very different, D/A has a very weak dependence on R_s. This is desirable, since the fitting function D/A has essentially only the one adjustable parameter α which is the only parameter of interest in this work. For small $|t|$, D/A goes like $1/\alpha$. Lastly, it should

be noted that D/A is also sensitive to σ_s so that the quality of the fit is dependent on how well the total cross section is measured.

In the analysis presented here for ^{4}He, the ratio D/A was used to fit the $\pi^{\pm}$-^{4}He elastic differential cross sections instead of the expressions for $\left(\frac{d\sigma}{d\Omega}\right)^{\pm}_{el}$ given in equation (134). Unlike the previous work on ^{4}He, data for both π^+ and π^- will be included in the analysis. The differential cross section data were taken from the work of Crowe et al.,[52] who measured both $\left(\frac{d\sigma}{d\Omega}\right)^{+}_{el}$ and $\left(\frac{d\sigma}{d\Omega}\right)^{-}_{el}$ at laboratory kinetic energies of 51, 60, 68, and 75 MeV. The total cross sections (which are needed for equation (139) and to calculate Im $f_s(0°)$) for these energies were interpolated from the results of the present experiment.

It is known that the expression for $\left(\frac{d\sigma}{d\Omega}\right)_{el}$ in equation (134) does not account for everything. The evidence for this comes from this and previous experiments[9,62] on self-conjugate nuclei. It has been found that the ratio $\Delta\sigma/\bar{\sigma}$ (where $\Delta\sigma = \sigma^{-}_{TOT} - \sigma^{+}_{TOT}$ and $\bar{\sigma} = \frac{1}{2}(\sigma^{-}_{TOT} + \sigma^{+}_{TOT})$) which was expected to be zero for a self-conjugate nucleus is of the order of several percent (about 15% in the case of the ^{4}He data of this experiment), for the reasons discussed above.

The standard assumption that is usually made is that the force experienced by the pion is of sufficiently short range that to a good approximation the pion has a straight-line trajectory. However, this becomes doubtful in the presence of the Coulomb field of the nucleus. Consider a pion incident on a nucleus with an impact parameter b close to the nuclear radius R_s. A π^- will be

dragged in and may disappear, assuming strong absorption. A π^+ will be repelled, miss the nucleus and, consequently, give little contribution to the absorption cross section. Thus the measured σ^-_{TOT} will be greater than the measured σ^+_{TOT} due to this Coulomb distortion of the pion trajectory.

These two effects, the distortion and energy shift, have been estimated by Fäldt and Pilkuhn[60,61] using a semiclassical model in which the pion trajectories are taken to be hyperbolic trajectories rather than straight line trajectories. In their first paper,[60] the nucleus was treated as a completely-absorbing sphere of radius R. This was later generalized in their second paper,[61] to describe scattering by gray nuclei. This model was used by Mutcher et al.[44] in the analysis of their ^{16}O data.

Before showing how this model modifies equation (134), it is necessary to introduce some notations. If k, E, and t are the asymptotic values of the pion wave number (in f_π^{-1}), the total energy, and the square of the momentum transfer in the center-of-mass frame, and k_R, E_E, and t_R are the same quantities evaluated at the nuclear surface, they are related by

$$k_R = \frac{k}{1+\delta} \quad , \tag{141}$$

$$E_R = E - \frac{Z_\pi Z\alpha hc}{R_s} \quad , \tag{142}$$

$$t_R = \frac{t}{1+\delta} \quad , \tag{143}$$

and

$$\delta = \frac{Z_\pi Z\beta}{kR_s} \quad , \tag{144}$$

where $Z_\pi (Z)$ is the pion (nuclear) charge, β is the pion velocity, and R_s is defined by $\sigma_s = 2\pi R_s^2$, which is only meaningful if $R_s \simeq$ nuclear radius. This definition of R_s is reasonable for energies around the (3,3) resonance where the nucleus is essentially black for pions. At lower energies the nucleus becomes more transparent to pions and the definition is less adequate.

The model relates the measured total cross section to the strong interaction total cross section evaluated at the energy of the pion at the nuclear surface, but corrected by a flux factor. The flux factor arises from the attraction (repulsion) of σ^- (σ^+) and, consequently, the nucleus appears to have a radius $R^\pm$ given by

$$R^\pm = \frac{R_s}{1 \pm |\delta|} \tag{145}$$

If σ_{TOT} and σ_s are the measured and strong interaction total cross sections, respectively, then according to the model

$$\sigma_{TOT} = \frac{\sigma_s}{(1+\delta)^2} \tag{146}$$

As a result of this, the strong amplitude f_s is modified to give a new amplitude $\tilde{f}_s$, where

$$\tilde{f}_s = \left(\frac{1}{1+\delta}\right) f_s \quad . \tag{147}$$

The differential cross section evaluated at the nuclear surface is now

$$\left(\frac{d\sigma}{d\Omega}\right)_{el} = \left| f_c(k_R, t_R) + \left(\frac{1}{1+\delta}\right) f_s(k_R, t_R) e^{-2i\phi} \right|^2 \quad , \tag{148}$$

or

$$\left(\frac{d\sigma}{d\Omega}\right)_{el} = \left| -\eta \frac{2k_R}{|t_R|} G(t_R) + \frac{k_R \sigma_s}{(1+\delta)4\pi} (i+\alpha) e^{-\frac{1}{6} R_s^2 |t_R|} e^{-2i\phi} \right|^2 \tag{149}$$

In terms of the asymtotic values of k and t,

$$\frac{d\sigma}{d\Omega} = \left| -\eta \frac{2k(1+\delta)}{|t|} e^{-\frac{1}{6}(R_c^2 + R_\pi^2)\frac{|t|}{(1+\delta)^2}} + \frac{k\sigma_s(i+\alpha)}{(1+\delta)^2 4\pi} e^{-\frac{1}{6} R_s^2 \frac{|t|}{(1+\delta)^2}} e^{-2i\phi} \right| \tag{150}$$

By using equation (150) to calculate D/A, one can compare the result to equations (139) or (140) to see the effect of the Fäldt and Pilkuhn[60,61] model. First, equation (148) is expanded to first order in δ. That this is reasonable may be seen from Table XVI, where $\delta << 1$. In the exponentials, the δ is dropped completely, since the exponential nearly cancels out in the ratio D/A as shown earlier. Now $\left(\frac{d\sigma}{d\Omega}\right)_{el}$ becomes

$$\left(\frac{d\sigma}{d\Omega}\right)_{el} = \left| (1+\delta) f_c(k,t) + \left(\frac{1}{1+\delta}\right)^2 f_s(k,t) e^{-2i\phi} \right|^2 \tag{151}$$

Table XVI. The values of δ as a function of the pion kinetic energy T_π. Two values of δ are given which correspond to $R_S = 1.63$ fm, both of which are reasonable values for R_S.

T_π (MeV)	$\delta(R_S = 1.63$ fm)	$\delta(R_S = 1.42$ fm)
51	0.0200	0.0229
60	0.0173	0.0199
68	0.0155	0.0178
75	0.0143	0.0164

$$= (1+\delta)^2|f_c|^2 + \left(\frac{1}{1+\delta}\right)|f_s|^2 + \left(\frac{2}{1+\delta}\right)f_c \mathrm{Re}(f_s e^{-2i\phi}) \quad (152)$$

$$\approx (1+s\delta)|f_c|^2 + (1-4\delta)|f_s|^2 + 2(1-\delta)f_c \mathrm{Re}(f_s e^{-2i\phi}) \quad (153)$$

Using the fact that

$$f_s^{\pm} = f_s \quad ,$$

$$-f_c^{+} = f_c^{-} = f_c \quad ,$$

and

$$\phi^{+} = -\phi^{-} = \phi$$

one can write the cross section difference D and the average cross section A as

$$D = (1-2|\delta|)|f_c^{-}|^2 + (1+4|\delta|)|f_s|^2 + 2(1+|\delta|)f_c^{-}\mathrm{Re}(f_s e^{2i\phi})$$
$$- (1+2|\delta|)|f_c^{+}|^2 - (1-4|\delta|)|f_s|^2$$
$$- 2(1-|\delta|)f_c^{+}\mathrm{Re}(f_s e^{-2i\phi}) \quad (154)$$

$$= -4|\delta||f_c|^2 + 8|\delta||f_s|^2 + 4f_c \cos 2\phi \, \mathrm{Re}\, f_s$$
$$- 4|\delta| f_c \sin 2\phi \, \mathrm{Im}\, f_s \qquad (155)$$

$$= 4f_c \cos 2\phi \, \mathrm{Re}\, f_s + \Delta_1 \quad , \qquad (156)$$

where

$$\Delta_1 = -4|\delta||f_c|^2 + 8|\delta||f_s|^2 - 4|\delta| f_c \sin 2\phi \, \mathrm{Im}\, f_s \qquad (157)$$

and

$$A = \frac{1}{2}[(1 - 2|\delta|)|f_c^-|^2 + (1 + 4|\delta|)|f_s|^2$$
$$+ 2(1 + |\delta|) f_c^- \mathrm{Re}(f_s e^{2i\phi}) + (1 + 2|\delta|)|f_c^+|^2$$
$$+ (1 - 4|\delta|)|f_s|^2 + 2(1 - |\delta|) f_c^+ \mathrm{Re}(f_s e^{-2i\phi})] \qquad (158)$$

$$= |f_c|^2 + |f_s|^2 + 4|\delta| f_c \cos 2\phi \, \mathrm{Re}\, f_s - 4f_c \sin 2\phi \, \mathrm{Im}\, f_s \qquad (159)$$

$$= |f_c|^2 + |f_s|^2 + \Delta_2 \quad , \qquad (160)$$

where

$$\Delta_2 = 4|\delta| f_c \cos 2\phi \, \mathrm{Re}\, f_s - 4f_c \sin 2\phi \, \mathrm{Im}\, f_s \quad . \qquad (161)$$

The ratio of the difference to the average is then

$$\frac{D}{A} = \frac{4f_c \cos 2\phi \, \mathrm{Re}\, f_s + \Delta_1}{|f_c|^2 + |f_s|^2 + \Delta_2} \quad , \qquad (162)$$

which is much like equation (140) except for the small corrections Δ_1 and Δ_2 in the numerator and denominator. As with equation (140), the R_s dependence is small because of cancellation of the exponential factors. However, some R_s dependence has reappeared via $|\delta|$, but

it is small for the energies being considered here, since $|\delta|$ is small as shown in Table XVI. Consequently, the ratio of the difference to average differential cross section is still essentially only sensitive to α.

In making the actual fit to the data, it was found that equation (162) gave a better fit than equation (140). Furthermore, the approximations made in deriving equation (162) were not used, and the complete expression for $\left(\frac{d\sigma}{d\Omega}\right)_{el}$ (equation (150)) was used in a computer code to calculate D/A.

To find α, the elastic $\pi^{\pm}$-^{4}He differential cross sections from Crowe et al.[52] were used. This data covered the center of mass angular region from 31° to 152°. However, only scattering angles before the first minimum in $\left(\frac{d\sigma}{d\Omega}\right)_{el}$ were used since the phenomenological model is valid only in this angular interval. The $\left(\frac{d\sigma}{d\Omega}\right)_{el}$ data are given in Table XVII as a function of T_π and the center-of-mass scattering angle, θ_{CM}. The total cross sections σ_s at 51, 60, 68, and 75 MeV were interpolated from Figure 20 where $\bar{\sigma}$ is plotted as a function of the laboratory kinetic energy T_π. They are given in Table XVIII. That it is reasonable to set $\sigma_s = \bar{\sigma}$ follows from the previous arguments that the average of the measured total cross sections σ^+_{TOT} and σ^-_{TOT} is independent of the Coulomb-nuclear interference correction. Also, $\bar{\sigma}$ is independent to first order of the flux correction of Fäldt and Pilkuhn. This can be seen from

$$\bar{\sigma} = \frac{1}{2}(\sigma^-_{TOT} + \sigma^+_{TOT})$$

Table XVII. The elastic $\pi^{\pm}$ - ^{4}He differential cross sections from Crowe et al. (Ref. 52). All cross sections are in mb, T_π is in MeV, and θ_{CM} is in degrees. The errors are the statistical errors.

T_π	θ_{CM}	$\frac{d\sigma^+}{d\Omega}$	$\frac{d\sigma^-}{d\Omega}$	$\frac{D}{A}$
51	31.5	1.516 ± 0.140	5.192 ± 0.254	1.096 ± 0.098
	36.7	1.611 ± 0.136	3.969 ± 0.166	0.845 ± 0.083
	41.9	1.223 ± 0.093	2.978 ± 0.145	0.835 ± 0.088
	47.1	1.131 ± 0.093	2.033 ± 0.107	0.570 ± 0.092
	62.5	0.434 ± 0.024	0.560 ± 1.025	0.254 ± 0.069
	67.6	0.266 ± 0.023	0.371 ± 0.020	0.329 ± 0.095
60	31.5	2.661 ± 0.075	6.712 ± 0.146	0.864 ± 0.038
	36.7	2.634 ± 0.071	5.033 ± 0.106	0.626 ± 0.035
	41.9	2.327 ± 0.052	3.854 ± 0.076	0.494 ± 0.031
	47.1	1.663 ± 0.046	2.835 ± 0.062	0.521 ± 0.035
	62.6	0.534 ± 0.010	0.747 ± 0.013	0.332 ± 0.025
	67.7	0.366 ± 0.009	0.436 ± 0.009	0.175 ± 0.033
68	31.6	4.031 ± 0.190	7.299 ± 0.273	0.577 ± 0.061
	36.8	3.612 ± 0.176	5.312 ± 0.361	0.381 ± 0.092
	42.0	3.247 ± 0.135	4.494 ± 0.164	0.322 ± 0.055
	47.2	2.651 ± 0.126	3.082 ± 0.223	0.150 ± 0.089
	62.7	0.722 ± 0.025	0.925 ± 0.034	0.246 ± 0.051
	67.8	0.437 ± 0.020	0.512 ± 0.026	0.158 ± 0.070
75	31.6	5.940 ± 0.205	9.394 ± 0.236	0.451 ± 0.042
	36.9	5.252 ± 0.167	7.080 ± 0.215	0.296 ± 0.045
	42.1	4.268 ± 0.141	5.858 ± 0.132	0.314 ± 0.039
	47.3	3.006 ± 0.104	3.979 ± 0.127	0.279 ± 0.047
	62.8	0.960 ± 0.025	1.119 ± 0.023	0.153 ± 0.033
	67.9	0.623 ± 0.019	0.667 ± 0.017	0.068 ± 0.030

Table XVIII. Total cross section σ_s as a function of the pion laboratory kinetic energy T_π.

T_π (MeV)	σ_s (mb)
51	102
60	115
68	127
75	139

$$\bar{\sigma} = \frac{1}{2}\left(\frac{\sigma_s}{(1-|\delta|)^2} + \frac{\sigma_s}{(1+|\delta|)^2}\right)$$

$$\simeq \frac{1}{2}(\sigma_s(1+2|\delta|) + \sigma_s(1-2|\delta|))$$

$$= \sigma_s \quad .$$

by using equation (146).

Given the experimental data for σ_s, $\left(\frac{d\sigma}{d\Omega}\right)^+_{el}$, and $\left(\frac{d\sigma}{d\Omega}\right)^-_{el}$ and the theoretical expression for D/A, the next problem was to find $\alpha(0°)$. This was accomplished by choosing at a fixed energy a pair of values for α and R_s and then by calculating the quantity

$$F(\alpha, R_s, \theta_i) \equiv \frac{D}{A} \tag{163}$$

(where equation (150) was used to calculate D/A) for each of the six center of mass scattering angles θ_i. The next step was to calculate the experimental ratio

$$\sigma(\theta_i) \equiv \frac{D(\theta_i)}{A(\theta_i)} \tag{164}$$

for each θ_i. This was then compared to F by calculating the value of chi-squared,

$$\chi^2 = \sum_{i=1}^{6} \left[\frac{\sigma(\theta_i) - F(\alpha,R_s,\theta_i)}{\Delta\sigma(\theta_i)}\right]^2 , \tag{165}$$

where $\Delta\sigma(\theta_i)$ is the error in $\sigma(\theta_i)$. The calculation was repeated for many pairs of α and R_s. The pair which gave the minimum value of χ^2 gave the best fit of $F(\alpha,R_s,\ )$ to the data $\sigma(\theta)$ and the best values of α and R_s. The whole procedure was handled by a computer code.

As was expected, the goodness of fit of $F(\alpha,R_s,\theta)$ to $\sigma(\theta)$ was insensitive to R_s. Consequently, R_s was set equal to the charge radius $R_c = 1.63$ fm and α was allowed to vary. Since only one parameter was determined from the six data points at each energy, there were five degrees of freedom.

The best fit values of α are given in Table XIX, along with $\mathrm{Im}\, f_s(0°)$ calculated from the optical theorem $\sigma_s = \frac{4\pi}{k}\mathrm{Im}\, f_s(0°)$, $\mathrm{Re}\, f_s(0°)$, and the chi-squared per degree of freedom, χ_R^2.

Table XIX. The best values of α, $\mathrm{Im}\, f_s(0°)$, and $\mathrm{Re}\, f_s(0°)$. T_π, $\mathrm{Im}\, f_s(0°)$, and $\mathrm{Re}\, f_s(0°)$ are in units of MeV, fm, and fm.

T_π	α	$\mathrm{Im}\, f(0°)$	$\mathrm{Re}\, f(0°)$	χ_R^2
51	1.10 ± .25	0.534	0.587 ± 0.133	2.7
60	1.05 ± .15	0.662	0.728 ± 0.099	7.8
68	1.05 ± .43	0.787	0.826 ± 0.338	0.9
75	1.03 ± .30	0.914	0.941 ± 0.274	1.7

The error $\Delta\alpha$ on α was obtained by keeping $R_s = R_c$ and allowing to vary until the chi-squared $\chi^2 = 5\chi_R^2$ increased by one unit. The new α' was then one standard deviation from the best fit value of α, so that $\Delta\alpha = |\alpha' - \alpha|$. This is a standard procedure for obtaining the error on a fitted parameter and is described in detail by Bevington.[33]

The large errors on the α are probably due to the fact that the Crowe et al.[52] differential cross sections are not in the small-angle interference region. Consequently, D is small with large errors, 10% or greater except at 60 MeV (see Table XVII). Data in the small-angle region with small statistical errors would be very desirable in trying to extract Re $f_s(0°)$. The large value of χ_R^2 for the 60 MeV data is due to the small statistical errors.

Having obtained the experimental values of Re $f(0°)$, the aim of this work was to compare these results to the forward dispersion relation calculations of Re $f(0°)$ by Wilkin et al.[8] and by Batty, Squier, and Turner.[4] Some basic features of forward dispersion relations will be discussed in Appendix F. A more detailed account may be found in the paper by Ericson and Locker[3] and in the text by Taylor.[63]

In Figure 23, the Re $f_s(0°)$ is plotted versus T_π. The data points from 110 to 260 MeV are from Binon et al.[59] and the curves are dispersion relation calculations by Wilkin et al.[8] (dashed curve) and by Batty, Squier, and Turner[4] (solid curve). The data points labeled by LAMPF refer to the results of this experiment.

The values of Re $f_s(0°)$ at 51, 60, 68, and 75 MeV are consistent with both theoretical curves. Even without the large error

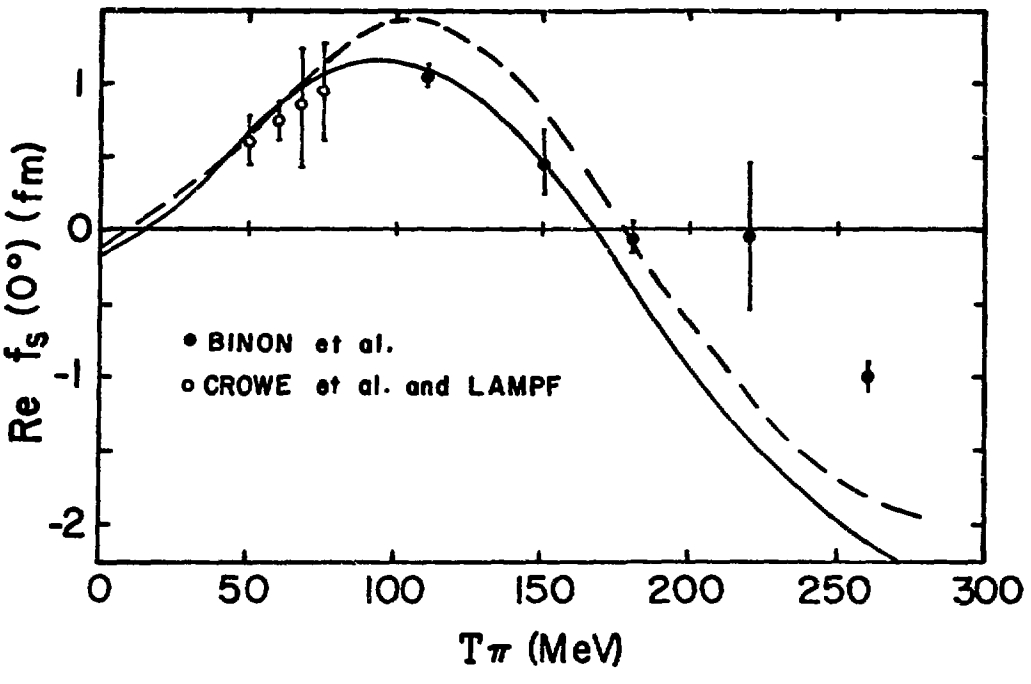

Figure 23 The real part of the forward π-^{4}He nuclear scattering amplitude Re $f_S(0°)$ versus the pion laboratory kinetic energy T_π. The data are from Binon et al. (Ref. 59) and Crowe et al. (Ref. 52) and this experiment (LAMPF). The curves are forward dispersion relation calculations. The solid curve is from Ref. 4 and the dashed curve is from Ref. 8.

bars the data are not in the right energy range to allow for a discrimination between the two calculations. The data are also slightly larger than the values obtained by Binon et al.[59] when they analyzed the data of Crowe et al.[52] using their measured σ_{TOT}^{-}. However, they do not quote any errors for their results, so that it is not clear how consistent the two analyses are. Furthermore, their analysis differed from the present one in several respects. They chose to fit $\left(\frac{d\sigma}{d\Omega}\right)_{el}^{-}$ rather than D/A, only π^- total cross section data were used and they did not include the flux correction of Fäldt and Pilkuhn.[60,61] Lastly, the phenomenological model they used for f_s contains a modification for the dips in $\left(\frac{d\sigma}{d\Omega}\right)_{el}$ which introduced another complex parameter to be determined by the data.

Optical Model Calculations

In this section, the measured $\pi^{\pm}$-^{4}He total cross sections will be compared to different optical model calculations.

The optical model reduces the complex many-body problem of π-nucleus scattering to an effective two-body problem. One method of calculating the optical potential utilizes a multiple-scattering series.[11,13,69,70] Using this approach (the details of the calculation are given in the references), the lowest-order optical potential in momentum space is given by

$$\langle \underset{\sim}{k}' | V | \underset{\sim}{k} \rangle = A\rho(\underset{\sim}{k} - \underset{\sim}{k}') \langle \underset{\sim}{k}' | t | \underset{\sim}{k} \rangle \quad . \tag{166}$$

In equation (166), $\underset{\sim}{k}$ and $\underset{\sim}{k}'$ are the initial and final pion momentum in the π-nucleus center-of-mass frame, A is the nuclear mass, $\rho(\underset{\sim}{k} - \underset{\sim}{k}')$ is the Fourier transform or form factor of the nuclear

matter density $\rho(R)$, $\langle \underset{\sim}{k}' | t | \underset{\sim}{k} \rangle$ is the off-shell π-nucleon scattering matrix, and $\langle \underset{\sim}{k}' | V | \underset{\sim}{k} \rangle$ is the lowest-order optical potential. By taking the Fourier transform of equation (166), one obtains the optical potential in coordinate space,

$$\langle \underset{\sim}{r}' | V | \underset{\sim}{r} \rangle = A \iint d^3k d^3k' e^{-i\underset{\sim}{k}' \cdot \underset{\sim}{r}'} \rho(\underset{\sim}{k} - \underset{\sim}{k}') \langle \underset{\sim}{k}' | t | \underset{\sim}{k} \rangle e^{i\underset{\sim}{k} \cdot \underset{\sim}{r}} \quad . \tag{167}$$

Equations (166) and (167) are the starting points for the comparison of the optical potential to the data.

The different optical potentials that were compared to the data come about from different assumptions as to the form of $\langle \underset{\sim}{k}' | t | \underset{\sim}{k} \rangle$. In order to account for the dominance of the (3,3) resonance, Kisslinger[47] assumed that

$$\langle \underset{\sim}{k}' | t | \underset{\sim}{k} \rangle = b_0 + b_1 \underset{\sim}{k}' \cdot \underset{\sim}{k} \tag{168}$$

where b_0 and b_1 give the strengths of the S- and P-wave amplitudes. This led to the Kisslinger potential in coordinate space

$$V_K \psi = -Ab_0 k^2 \rho \psi + Ab_1 \nabla \cdot (\rho \nabla \psi) \quad . \tag{169}$$

It is nonlocal since it contains momentum operators, and it has a strong sensitivity to π scattering in the nuclear surface because of the $\nabla\rho$ term.

Another possible form of the off-shell π-nucleon scattering matrix[48-50] is given by

$$\langle \underset{\sim}{k}' | t | \underset{\sim}{k} \rangle = b_0 + b_1 (k^2 - \tfrac{1}{2} q^2) \tag{170}$$

where $\underset{\sim}{q} = \underset{\sim}{k}' - k$ and $k_0 = |\underset{\sim}{k}'| = |\underset{\sim}{k}|$ (for on-shell). This comes from $\underset{\sim}{k}' \cdot \underset{\sim}{k} = \frac{1}{2}(k^2 + k'^2) - \frac{1}{2}q^2$. Equation (170) leads to the Laplacian potential in coordinate space

$$V_L\psi = -A(b_0 + b_1)k^2\rho\psi - \frac{1}{2}Ab_1(\nabla^2\rho)\psi \quad . \tag{171}$$

It is local since it is a function of only the position operator and, through the $\nabla^2\rho$ term, it is sensitive to π scattering in the nuclei surface.

A simple optical model without the derivatives of the nuclear density can also accommodate the P-wave π-nucleon interaction through an energy-dependent effective radius. Such a model was derived by Silbar and Steinheim.[71] They assumed

$$\langle \underset{\sim}{k}' | t | \underset{\sim}{k} \rangle = b_1(k^2 - q^2) \tag{172}$$

and derived

$$V_{ER}\psi = -Ab_1k^2\rho_{R^*}(r)\psi \quad . \tag{173}$$

If the nuclear charge density $\rho(r)$ is characterized by R*, where

$$R^{*2} = R^2 + \frac{3}{k^2} \quad . \tag{174}$$

and R is the nuclear radius, their model is called the "effective radius" model. If R is used in place of R* in equation (174), then V_{ER} becomes the "matter-radius" model, given by

$$V_{MR}\psi = -Ab_1k^2\rho_R(r)\psi \quad . \tag{175}$$

The "effective-radius" model can also be generalized. If the ℓ-th partial wave dominates, then R* is modified to become

$$R^{*2} = R^2 + \frac{3\ell(\ell+1)}{2k^2} \tag{176}$$

The off-shell π-nucleon scattering matrix used in equation (166) is a function of momenta and energies which are evaluated in the π-nucleus center-of-mass systems. However, the π-nucleon scattering amplitude is usually determined in the π-nucleon center-of-mass system. The necessary transformation of the π-nucleon scattering matrix from the π-nucleon to the π-nucleus center-of-mass system leads to ambiguities. One choice among them leads to a "modified" Kisslinger potential,[72-74] given by

$$V_{MK}\psi = -Ab_0k^2\rho(r)\psi + Ab_1\nabla\cdot\rho\nabla\psi - \frac{1}{2}A\frac{E_c + m_\pi}{m}b_1(\nabla^2\rho)\psi \quad . \tag{177}$$

In equation (177), m_π is the pion mass, m is the nucleon mass, and E_c is the kinetic energy of the π in the π-nucleus center-of-mass system.

The last optical model that was considered was based on a separable π-nucleon scattering matrix given for each eigenchannel $n = (\ell, I, j)$ by

$$\langle \underset{\sim}{k}' | t | \underset{\sim}{k} \rangle = \frac{\langle k_0 | t_n | k_0 \rangle g_n(k') g_n(k)}{g_n(k_0)^2} \tag{178}$$

where $\langle k_0 | t_n | k_0 \rangle$ is the on-shell matrix element ($k_0 = |\underset{\sim}{k}'| = |\underset{\sim}{k}|$) which, along with the $g_n(k)$ functions, is constructed from the

complex π-nucleon phase shifts.[75,76] Equations (178) and (166) then give a separable optical potential in momentum space.[70,77]

Landau[78,79] has used this separable potential to calculate the average total cross section $\bar{\sigma}$ for $\pi^{\pm}$ - ^{4}He scattering. His results, along with the calculations of $\bar{\sigma}$ using the other optical potentials discussed above, are given in Figures 24 and 25. (The average cross section $\bar{\sigma}$ was compared to the models, rather than σ^{+}_{TOT} or σ^{+}_{TOT}, because it is less model-dependent, in that it is independent of the Coulomb-nuclear interference.) With the exception of Landau's calculation, all of the curves in these figures were calculated with the computer code PIRK[45,46], which was also used to calculate the Coulomb-nuclear interference correction. The data in the two figures are from Wilkin et al.[8] and the present experiment (LAMPF). Together they span the energy range 50 to 250 MeV. In Figure 24, curve 1 is the calculation of Landau, curve 2 is the prediction of the Laplacian model, and curve 3 is the prediction of the Kisslinger model. In Figure 25, curves 1, 2, and 3 are the predictions of the "effective radius," the "matter radius," and the modified Kisslinger potential, respectively. Except for Landau's calculation, all of the models were used with a Gaussian nuclear matter distribution ρ given by equation (105), with the nuclear radius R equal to the charge radius $R_c = 1.63$ fm. Landau used a nuclear form factor equal to the nuclear charge form factor ρ_c with the finite proton size removed:

$$\rho(q) = \frac{\rho_c(q)}{f_c^p(q)} \tag{179}$$

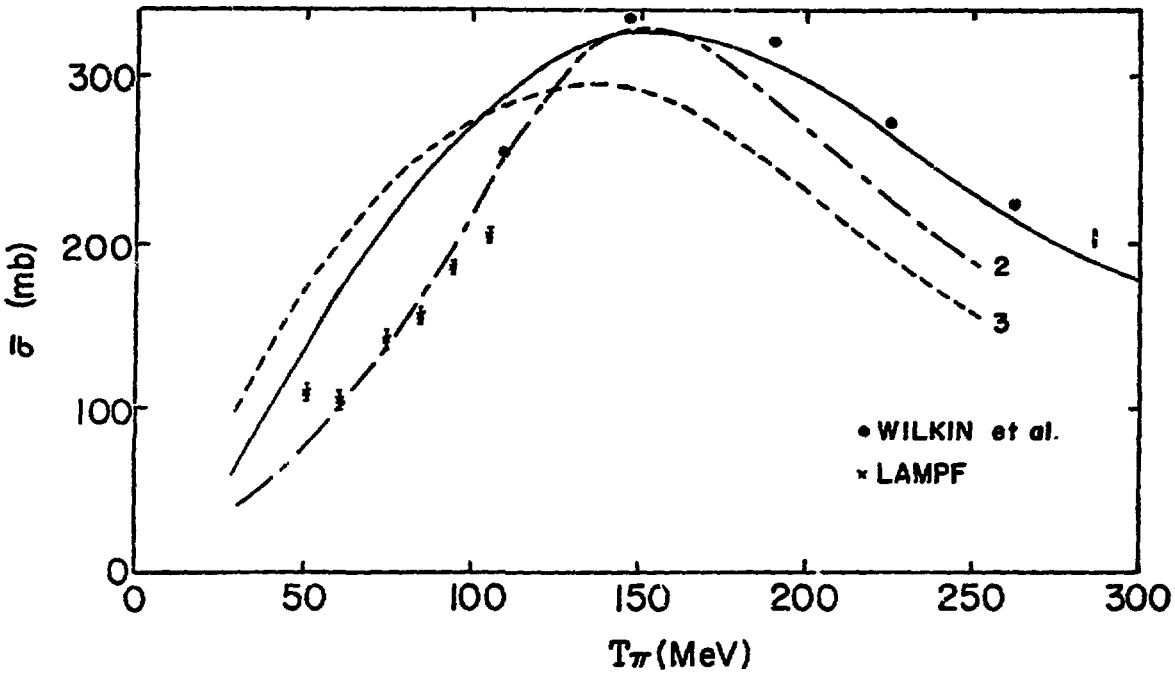

Figure 24. Comparison between the measured π-^{4}He average total cross sections and the predictions of the separable (Refs. 78 and 79) Laplacian, and Kisslinger optical potentials. The predictions of these three potentials are given by curves 1, 2, and 3, respectively. The data are from this experiment (LAMPF) and Wilkin et al. (Ref. 8).

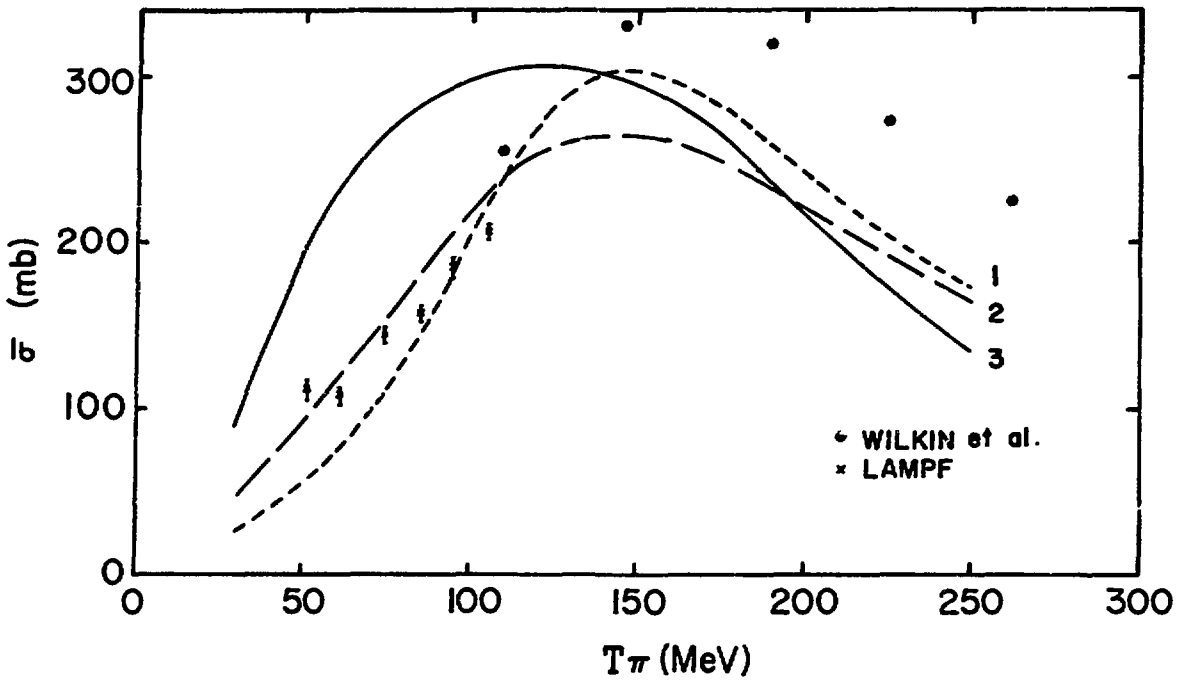

Figure 25. Comparison between the measured π-^{4}He average total cross sections and the predictions of the "effective-radius," "matter-radius," and modified Kisslinger optical potentials. The predictions of these three potentials are given by curves 1, 2, 3, respectively. The data are from this experiment (LAMPF) and Wilkin et al. (Ref. 8).

where q is the momentum transfer and $f_c^p(q)$ is the proton form factor. The nuclear charge form factor ρ_c was given by the experimental charge form factor[80]

$$\rho_c(q) = [1 - (a^2q^2)6]e^{-b^2q^2} \quad ,$$

with a = 0.316 fm and b = 0.681 fm.

It should be noted that the b_0 and b_1 parameters used in these calculations were derived from the fit to the free π-nucleon phase shifts, made by Saloman.[53] For the "effective-radius" and "matter-radius" models a correction b_0 was added to the parameter b_1 in equations (173) and (175) to account for the small S-wave π-nucleon amplitude.[71]

Unlike the other optical potentials, the separable potential of Landau does not contain any adjustable parameters. In the Kisslinger and Laplacian models, however, the b_0 and b_1 parameters can be allowed to vary to obtain the best fit to the data. Crowe et al.[52] did this to obtain the best fit of the Kisslinger model to their elastic $\pi^{\pm}$-^{4}He differential cross section data. By interpolating between and extrapolating from their parameters, $\bar{\sigma}$ was calculated both with these parameters and with the free parameters in the energy range 50 to 105 MeV. The results are given in Figure 26, where curves 1 and 2 are the Kisslinger and Laplacian calculations with the free parameters. Curves 3 and 4 are the Kisslinger and Laplacian calculations with the fitted parameters. The data are from the present experiment (LAMPF). It is clear that the two models are quite sensitive to b_0 and b_1. Furthermore, for

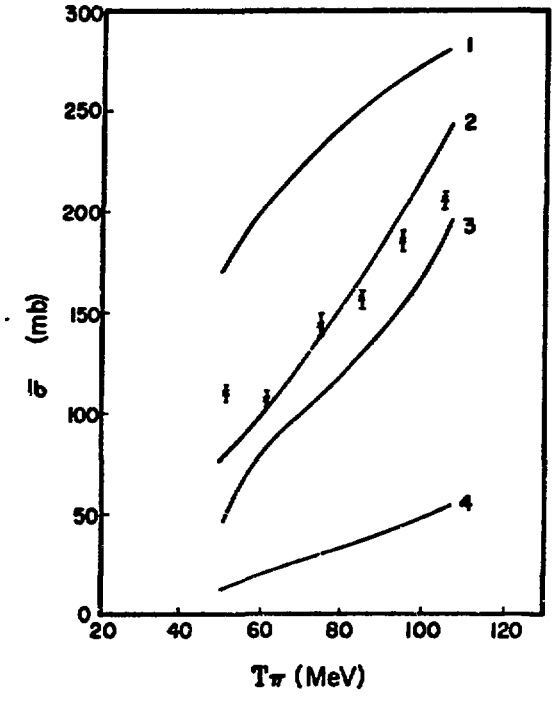

Figure 26. The effect of different values of b_0 and b_1 on the predictions of $\bar{\sigma}$ by the Kisslinger and Laplacian optical potentials. Curves 1 and 2 (3 and 4) are the Kisslinger and Laplacian predictions using the free (fitted) parameters.

the Kisslinger model with b_0 and b_1 obtained from fitting the elastic scattering data, the agreement with the total cross section data is not very good. Also as mentioned earlier, Cooper and Eisenstein[51] found that when they allowed b_0 and b_1 to vary to fit $\left(\frac{d\sigma}{d\Omega}\right)^+_{el}$ for ^{12}C and both $\left(\frac{d\sigma}{d\Omega}\right)^+_{el}$ and $\left(\frac{d\sigma}{d\Omega}\right)^-_{el}$ for ^4He, the resulting Kisslinger and Laplacian models violated unitarity. The ^4He data they used was from Crowe et al.[52] and, by fitting $\left(\frac{d\sigma}{d\Omega}\right)^+_{el}$ and $\left(\frac{d\sigma}{d\Omega}\right)^-_{el}$ separately, they obtained four sets of b_0 and b_1. They found that the fits of Crowe et al.[52] also violated unitarity.

From Figures 24, 25, and 26, it can be seen that none of the different models fit the data very well. At the higher energies the separable potential fits the best and at the lower energies the Laplacian potential is the best. However, the Laplacian potential is not successful in fitting the elastic differential cross section as shown by Cooper and Eisenstein.[51] Landau and Thomas[81] found that the separable potential did not fit the low-energy pion-nucleus elastic scattering (π^+-^{12}C and $\pi^\pm$-^4He). This failure they attributed to a lack of good low-energy π-nucleon phase shifts which are essential for their model. Amann et al.,[82] using free π-nucleon phase shift information, found that the Kisslinger and Laplacian potentials, along with the separable potential of Londergan, McVoy, and Moniz,[76] gave poor fits to their 51 MeV π^+ - ^{12}C elastic differential cross section data.

As mentioned at the beginning of this chapter, the experiments of Crowe et al.,[52] Nordberg and Kinsey,[55] and Bloch et al.[56] measured $\pi^\pm$-^4He elastic differential cross section at low energies

in an attempt to measure the rms electromagnetic radius of the pion. In their analyses, they used the Kisslinger potential. However, in view of the poor agreement between experiment and the different optical models at low energy, it appears that such analyses are unlikely to yield a reliable rms electromagnetic radius for the pion.

For the Kisslinger and Laplacian potentials, there are two other adjustable parameters, the nuclear charge radius R_c ($R_c = 1.63$ fm[40] as measured from electron scattering) and the nuclear mass radius R. With the free values of b_0 and b_1, R_c and R were varied in order to check, in a limited way, the sensitivity of the optical potentials to these parameters. It is a standard practice to define a new charge radius $R_c' = (R_c^2 + R_\pi^2)^{1/2}$ where $R_\pi = 0.8$ fm[8,39] is the charge radius of the pion so that $R_c' = 1.82$ fm. Both R_c and R_c' were used in the Gaussian charge distribution given by equation (103) to see what effect, if any, they had on the calculated $\bar{\sigma}$. There was found to be a negligible difference (less than 0.5%) between the two.

As for R, there are two common practices. The first is simply to set $R = R_c$. The other is to calculate the R from $R = (R_c^2 - R_p^2)^{1/2}$, where $R_p = 0.8$ fm[40] is the proton charge radius. In the first case, $R = 1.63$ fm and in the second $R = 1.42$ fm. Figure 27 shows the results of using $R = 1.63$ fm and $R = 1.42$ fm in the Kisslinger and Laplacian potentials. Curves 1 and 3 (2 and 4) are for the Laplacian and Kisslinger potentials, with $R = 1.63$ fm ($R = 1.42$ fm). The smaller value of R gives a worse fit to $\bar{\sigma}$ than the larger value of R. For $R = 1.42$ fm, the peak is lower, and at low energies $R = 1.42$ fm leads to

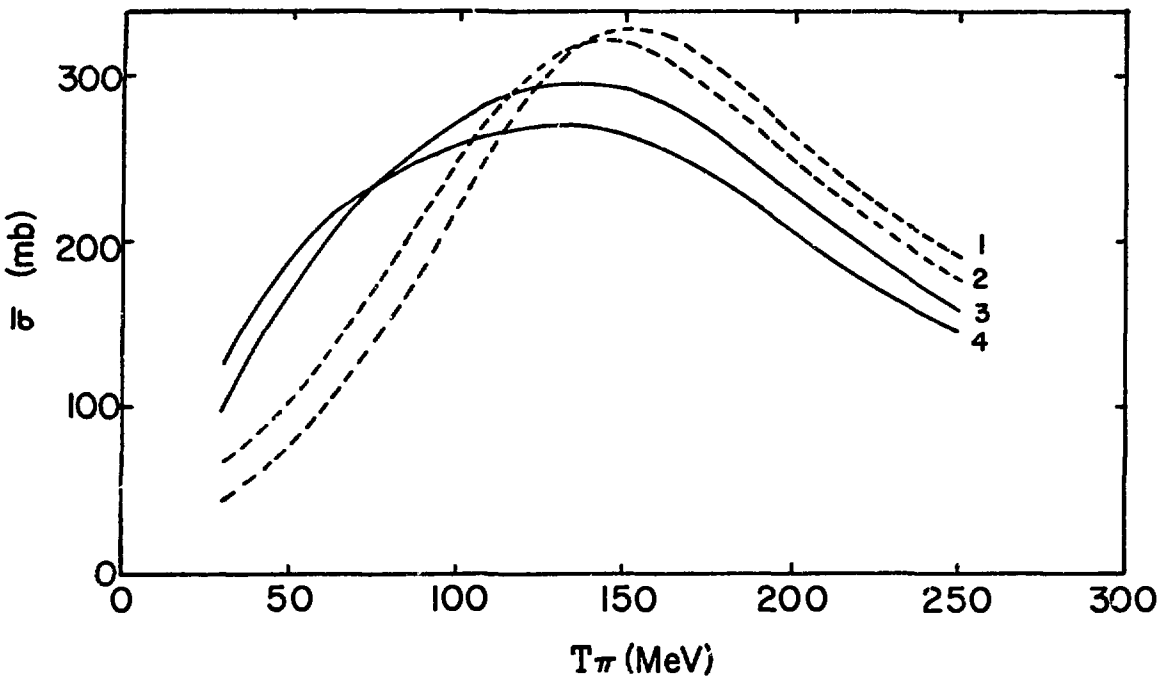

Figure 27. The effect of varying R_S on the predictions of $\bar{\sigma}$ by the Kisslinger and Laplacian optical potentials Curves 1 and 3 (2 and 4) are the Laplacian and Kisslinger predictions with $R_S = 1.63$ fm ($R = 1.42$ fm).

larger cross sections than R = 1.63 fm (this is reversed at high energies). This same behavior was exhibited by both the "matter-radius" and the modified Kisslinger models. The "effective'radius" model behaved differently. Up to about 110 MeV there was negligible difference between the two cases. Above ~110 MeV, R = 1.42 fm gave larger cross sections than R = 1.63 fm. The discrepancy was a maximum at ~170 MeV, where it was ~6% and then remained essentially constant as the energy increased. However, using R = 1.42 fm did not substantially improve the fit of the "effective-radius" model to the data.

Finally, comparisons between the models and experiment were made for the ratio $\frac{\Delta\sigma}{\bar{\sigma}}$, as shown in Figure 28. The data from this experiment (LAMPF) presented in Figure 28 have been corrected for Coulomb-nuclear interference with the Kisslinger potential using the fitted parameters derived from the work of Crowe et al.[52] Curves 1, 2, and 3 were obtained from the semi-classical model of Fäldt and Pilkuhn,[60,61] the Kisslinger potential and the Laplacian potential. According to Fäldt and Pilkuhn,

$$\frac{\Delta\sigma}{\bar{\sigma}} \sim \frac{8\alpha\beta}{kR_s} \quad , \tag{180}$$

where E is the total pion energy, k is the pion wave number, β is the pion velocity, and R_s is the strong interaction radius (R_s = 1.63 fm). Again, there does not appear to be any particularly good agreement between theory and experiment. However, the errors on the low-energy points are quite large and need to be reduced to

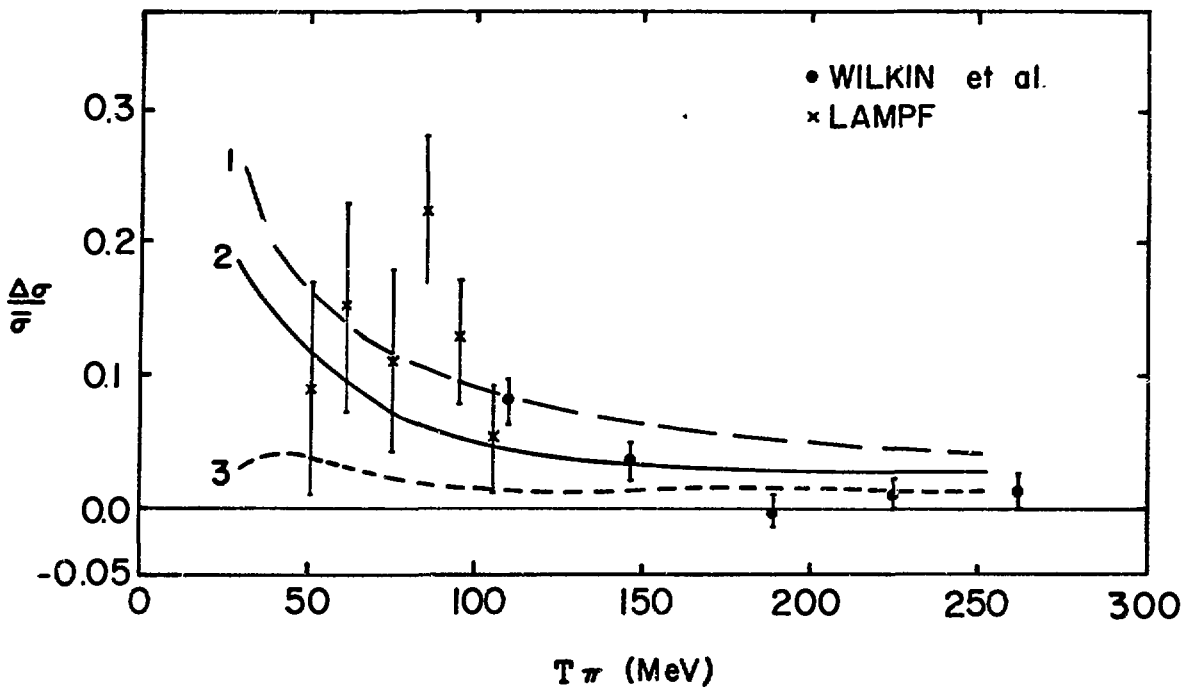

Figure 28. Comparison between the measured ratio $\Delta\sigma/\bar{\sigma}$ and the predictions of the semi-classical model of Faldt and Pilkuhn (Refs. 60 and 61) and the Kisslinger and Laplacian optical potentials. The predictions of these three models are given by curves 1, 2, and 3, respectively. The data are from this experiment (LAMPF) and Wilkin et al. (Ref. 8).

make any definitive comment on the different models. The results are the same for the other values of $\Delta\sigma/\bar{\sigma}$ in Table XV. Also, the values of $\Delta\sigma/\bar{\sigma}$ calculated from the data of Bloch et al.[56] (see Table XIII) are statistically consistent with the results of this experiment.

Concluding Remarks

The measured $\pi^{\pm}$-^{4}He total cross sections of this experiment were compared to the previous measurements of Bloch et al.,[56] Fowler, et al.,[57] Binon et al.,[59] and Wilkin et al.[8] Within the statistical errors, the agreement was good, except for the 51 MeV data of this experiment and of Bloch et al.[56] (i.e., the systematic errors appear to be much larger than the statistical errors). There is a similar disagreement among the 110 MeV data of Wilkin et al.[8] and the 110 and 105 MeV data of Binon et al.[59] and this experiment, respectively.

The average total cross section $\bar{\sigma}$ was found to be independent of the Coulomb-nuclear interference correction and therefore reasonably model-independent, since the variation in the measured values of $\bar{\sigma}$ due to the choice of the model used in the interference correction ranged from a 0.7% variation at 51 MeV to 0.2% variation at 105 MeV. This was not found to be true for the measured values of σ_{TOT}^{+} and σ_{TOT}^{-}, which varied by as much as 5%, depending upon how the interference correction was made. This suggests the desirability of measuring the elastic differential cross section in the small-angle interference region. This would allow the interference correction to be made in a model-independent way. Finally, σ_{TOT}^{-} was found to be greater than

σ^{+}_{TOT} (at all energies) as was seen in the ^{12}C data of this experiment and in the previous ^{4}He data[56,57] and ^{12}C data.[9,62] These differences in the cross sections are presumably due to an incorrect handling of the different Coulomb effects, such as distortion, interference, etc., by the different theoretical models.

The measured values of σ^{+}_{TOT} and σ^{-}_{TOT} were shown not to be related through the optical theorem to the imaginary part of the forward nuclear scattering amplitude given by equation (110), due to the Coulomb interaction. However, σ^{+}_{TOT} and σ^{-}_{TOT} were shown to be related through the optical theorem to the imaginary part of the forward scattering amplitude $\tilde{f}_n(0°)$, where $\tilde{f}_n(\theta)$ is defined by equation (121). It should be noted that $\tilde{f}_n(\theta)$ is not the scattering amplitude which contributes to the measured $\pi^{\pm}$-nucleus elastic differential cross section (the scattering amplitude which does contribute is $f_n(\theta)$ defined by equation (116)). However, through the optical theorem given by equation (122), $\tilde{f}_n(0°)$ does put a constraint on any model of the π-nucleus interaction.

An attempt was made to verify experimentally the forward dispersion relation calculations[4,8] of the real part of the forward nuclear scattering amplitude in the energy region of 50 to 75 MeV, using a phenomenological model for the nuclear amplitude f_s. The results were moderately successful in their agreement with the forward dispersion relation calculations. However, it would be desirable to measure the elastic differential cross sections in the small-angle interference region in the hope that this would reduce the large statistical errors on the experimental values of Re $f_s(0°)$.

The measured values of $\bar{\sigma}$ from this experiment and from Wilkin et al.[8] were compared to several optical potential calculations. The reason the experimental values of $\bar{\sigma}$ were compared to the theoretical calculations rather than the experimental values of $\sigma_{TOT}^{\pm}$ was because they were not strongly dependent on the Coulomb-nuclear interference correction. The agreement between experiment and theory was found to be very poor in the low-energy region. From this work and the work of others,[51,81,82] it was found that none of the optical potentials could successfully describe both the total cross section data and the elastic differential cross section data. These results suggest the need for more work in the theory of low energy π-nucleus scattering and for more low-energy data of high statistical accuracy. There are future plans for this experiment to measure $\pi^{\pm}$ - ^{4}He and, possibly, $\pi^{\pm}$ - ^{12}C total cross sections, at energies as low as 20 MeV. The poor agreement between theory and experiment also indicates that attempts to measure the rms electromagnetic radius of the pion by invoking optical models for the strong interaction are probably unreliable and also probably unnecessary due to the results of the π-electron scattering experiments.

BIBLIOGRAPHY

1. C. M. G. Lattes, H. Muirhead, G. P. S. Occhialini, and C. F. Powell, Nature (Lond.) 159, 694 (1947).

2. J. P. Stroot, "Experiments in Pion Nucleus Physics" in Lectures from the LAMPF Summer School on the Theory of Pion-Nucleus Scattering, Los Alamos Scientific Laboratory report LA-5443-C (1973).

3. T. E. O. Ericson and M. P. Locher, Nucl. Phys. A148, 1 (1970).

4. C. J. Batty, G. T. A. Squier, and G. K. Turner, Nucl. Phys. B67, 492 (1973).

5. G. T. A. Squier, M. E. Cage, G. J. Pyle, A. S. Clough, G. K. Turner, B. W. Allardyce, C. J. Batty, D. J. Baugh, W. J. McDonald, R. A. J. Riddle, and L. H. Watson, Phys. Rev. Lett. 31, 389 (1973).

6. W. O. Lock and D. F. Measday, Intermediate Energy Nuclear Physics (Methuen and Co. Ltd., London, 1970).

7. B. W. Allardyce, C. J. Batty, D. J. Baugh, W. J. McDonald, R. A. J. Riddle, L. H. Watson, M. E. Cage, G. J. Pyle, G. T. A. Squier, A. S. Clough, and G. K. Turner, Rutherford Laboratory report RPP/NS11 (1973).

8. C. Wilkin, C. R. Cox, J. J. Domingo, K. Gathuler, E. Pedroni, J. Rohlin, P. Schwaller, and N. W. Turner, Nucl. Phys. B62, 61 (1973).

9. A. S. Carroll, I-H. Chiang, C. B. Dover, T. F. Kysia, K. K. Li, P. O. Mazur, D. N. Michael, P. M. Mockett, D. C. Rahn, and R. Rubinstein, "Pion-Nucleus Total Cross Sections in the (3,3) Resonance Region" in Abstracts of Contributed Papers, Sixth International Conference on High-Energy Physics and Nuclear Structure (Santa Fe and Los Alamos, N.M., June 9-13, 1975), Los Alamos Scientific Laboratory report LA-6030-C (1975).

10. M. D. Cooper and M. B. Johnson, "Integrated Pion-Nucleus Cross Sections," Los Alamos Scientific Laboratory preprint LA-UR-75-2032 (1975).

11. J. M. Eisenberg, "Introductory Review of Multiple-Scattering Theory for Pion-Nucleus Scattering" in Lectures from the LAMPF Summer School on the Theory of Pion-Nucleus Scattering, Los Alamos Scientific Laboratory report LA-5443-C (1973).

12. D. S. Koltun, Adv. Nucl. Phys. 3, 71 (1969).

13. M. M. Sternheim and R. R. Silbar, Ann. Rev. Nuc. Sci. 24, 249 (1975).

14. J. Hüffner, "Pions Scatter by Nuclei" in AIP Conference Proceedings No. 26, High-Energy Physics and Nuclear Structure - 1975 (Santa Fe and Los Alamos), Editors D. E. Nagle, A. S. Goldhaber, C. K. Hargrove, R. L. Burman, and B. G. Storms, (American Institute of Physics, New York, 1975).

15. B. W. Allardyce, C. J. Batty, D. J. Baugh, E. Friedman, G. Heymann, M. E. Cage, G. J. Pyle, G. T. A. Squier, A. S. Clough, D. F. Jackson, S. Murugesu, and V. Rajaratnam, Nucl. Phys. A209, 1 (1973).

16. G. Giacomelli, Total Cross-Section Measurements, (Pergamon Press Ltd., Oxford, 1970).

17. J. V. Allaby, Yu. B. Bushnin, S. P. Denisov, A. N. Diddens, R. W. Dobinson, S. V. Donskov, G. Giacomelli, Yu. P. Gorin, A. Klovning, A. I. Peirukhin, Yu. D. Prokoshkin, R. S. Shuvalov, C. A. Siahlbrandt, and D. A. Sioyanova, Phys. Lett. 30B, 500 (1969).

18. H. H. Howard, B. Storms, and S. P. Slatkin, LAMPF Users Handbook, (Los Alamos Scientific Laboratory, Medium Energy Physics Division, Los Alamos, N.M., 1974).

19. J. Amato, R. Burman, H. Cowan, and M. Jakobson, "Properties of a Proposed Low Energy General Purpose Pion Channel," LAMPF internal report (August 1970).

20. R. L. Fulton, "Mechanical Design of the LAMPF Low Energy Pion Channel," Los Alamos Scientific Laboratory report LA-5222-MS (1970).

21. M. D. Cooper, "Time-of-Flight Measurements at the LAMPF Low-Energy Pion Channel," Los Alamos Scientific Laboratory report LA-55-29-MS (1974).

22. R. Meunier, "DISC Counters," in the NAL 1970 Summer Study, National Accelerator Laboratory report SS-170 (1970).

23. B. A. Leontic and J. Teiger, "A Differential Liquid Cerenkov Counter with Continuously Variable Velocity Response," Brookhaven National Laboratory report BNL 50031 (T-447) (1966).

24. G. Charpak, R. Bouclier, T. Bressani, J. Favier, and C. Zupancio, Nucl. Instrum. Methods 62, 262 (1968).

25. G. Charpak, Ann. Rev. Nucl. Sci. 20, 195 (1970).

26. G. Charpak, D. Rahm, and H. Steiner, Nucl. Instrum. Methods 80, 13 (1970).

27. H. O. Meyer, Nucl. Instrum. Methods 120, 143 (1974).

28. L. Costrell, "Standard Nuclear Instrument Modules," ERDA report TID-20893 (Rev. 4) (July 1974).

29. L. Costrell (editor), "Camac Tutorial Issue," IEE Trans. Nucl. Sci. NS-20, 1 (1973).

30. T. Kycía, Brookhaven National Laboratory, private communication, 1972.

31. W. T. Eadie, D. Dryard, F. E. James, M. Ross, and B. Sadoulet, Statistical Methods in Experimental Physics (North-Holland Publishing Company, Amsterdam, 1971).

32. G. Burleson, New Mexico State University, private communication, 1974.

33. P. R. Bevington, Data Reduction and Error Analysis for the Physical Sciences (McGraw-Hill Book Company, New York, 1969).

34. J. Orear, "Notes on Statistics for Physicists," University of California Radiation Laboratory report UCRL-8417 (Berkeley, California, August 1958).

35. G. Moliere, Z. Naturforsch 2a, 133 (1947); 3a, 78 (1948).

36. J. B. Marion and B. A. Zimmerman, Nucl. Instrum. Methods 51, 93 (1967).

37. U. Fano, Phys. Rev. 93, 117 (1954).

38. N. F. Mott and H. S. W. Massey, The Theory of Atomic Collisions, Third Edition (Oxford University Press, London, 1965).

39. G. T. Adylov, F. K. Aliev, D. Yu. Bardin, W. Gajewski, I. Ion, B. A. Kulakov, G. V. Micelmacher, B. Niczyporuk, T. S. Nigmanov, E. N. Tsyganov, M. Turala, A. S. Vodopianov, K. Wala, E. Dalby, D. Drickey, A. Liberman, P. Shepard, J. Tompkins, C. Buchanan, and J. Poirier, Phys. Lett. 51B, 402 (1974).

40. H. R. Collard, L. R. B. Elton, and R. Hofstadter, Landolt-Bornstein: Numerical Data and Functional Relationships; Nuclear Radii, edited by K. H. Hellwege (Springer, Berlin, 1967), New Series, Group I, Vol. 2.

41. G. Burleson, New Mexico State University, private communication, 1975.

42. F. Binon, V. Bobyn, P. Duteil, N. Gouanere, L. Hugon, J. P. Pergneux, J. Renuart, S. Schmit, M. Spighel, and J. P. Stroot, Nucl. Phys. B33, 42 (1971); B40, 608 (1972).

43. M. L. Scott, G. S. Mutchler, C. R. Fletcher, E. V. Hungerford, L. V. Coulson, G. C. Phillips, B. W. Mayes, L. Y. Lee, J. C. Allred, and C. Goodman, Phys. Rev. Lett. 28, 1209 (1972).

44. G. S. Mutchler, C. R. Fletchler, L. V. Coulson, D. Mann, M. D. Gabitzsch, G. C. Phillips, B. W. Mayes, E. V. Hungerford, L. Y. Lee, C. Goodman, and J. C. Allred, Phys. Rev. C11, 1873 (1975).

45. R. A. Eisenstein and G. A. Miller, Computer Physics Communications 8, 130 (1974).

46. M. D. Cooper and R. A. Eisenstein, "FITPI: Modifications to the Optical Model Program PIRK for Parameter Searches and Total Cross Sections," Los Alamos Scientific Laboratory report LA-5929-MS (1975).

57. L. S. Kisslinger, Phys. Rev. 98, 761 (1955).

48. H. K. Lee and H. McManus, Nucl. Phys. A167, 257 (1971).

49. G. Fäldt, Phys. Rev. C5, 400 (1972).

50. J. H. Koch and M. Sternheim, Phys. Rev. C6, 1118 (1972).

51. M. D. Cooper and R. A. Eisenstein, "Low Energy Pion Elastic Scattering from Light Nuclei," Los Alamos Scientific Laboratory preprint (1975).

52. K. M. Crowe, A. Fainberg, J. Miller, and A. S. L. Parsons, Phys. Rev. 180, 1349 (1969).

53. M. Saloman, "Low Energy (0-250 MeV) Pion-Nucleon Phase-Shift Fits," TRIUMF report TRI-79-2 (Tri-University Meson Facility, Vancouver, Canada, December 1974).

54. J. F. Janni, "Calculations of Energy Loss, Range, Pathlength, Straggling, Multiple Scattering, and the Probability of Inelastic Nuclear Collisions for 0.1- to 1000-MeV Protons," Air Force Weapons Laboratory technical report AFWL-TR-65-150 (Kirtland Air Force Base, New Mexico, 1966).

55. M. E. Nordberg and K. F. Kinsey, Phys. Lett. 20, 692 (1966).

56. M. M. Block, I. Kenyon, J. Keren, D. Koethe, P. Malhotra, R. Walker, and H. Winzeler, Phys. Rev. 169, 1074 (1968).

57. E. C. Fowler, W. B. Fowler, R. P. Shutt, A. M. Thorndike, and W. L. Whittemore, Phys. Rev. 91, 135 (1953).

58. L. Alexandrov, T. Angelescu, I. V. Falomkin, M. M. Kulyukin, V. I. Lyashenko, R. Mach, A. Mihul, N. M. Kao, F. Nichitiu, G. B. Pontecorvo, V. K. Saricheva, M. Semergieva, Yu. A. Shcherbakov, N. I. Trosheva, T. M. Troshev, F. Balestra, L. Busso, R. Garfagnini, and G. Piragino, "Elastic Scattering of $\pi^{\pm}$ on ^{3}He and ^{3}He in the Energy Range 68 to 208 MeV," in Abstracts of Contributed Papers, Sixth International Conference on High-Energy Physics and Nuclear Structure (Santa Fe and Los Alamos, N.M. June 9-13, 1975), Los Alamos Scientific Laboratory report LA-6030-C (1975).

59. F. Binon, P. Duteil, M. Gouanere, L. Hugon, J. Jansen, J.-P. Lagnaux, H. Paleosky, J.-P. Peigneux, M. Spighel, and J.-P. Stroot, Phys. Rev. Lett. 35, 145 (1975).

60. G. Fäldt and H. Pilkuhn, Phys. Lett. 40B, 613 (1972).

61. G. Fäldt and H. Pilkuhn, Phys. Lett, 46B, 337 (1973).

62. A. S. Clough, G. K. Turner, B. H. Allardyce, C. J. Batty, D. J. Baugh, J. D. McDonald, R. A. J. Riddle, L. H. Watson, M. E. Cage, G. J. Pyle, and G. T. A. Squier, Phys. Lett. 43B, 476 (1973).

63. J. R. Taylor, Scattering Theory (John Wiley & Sons, Inc., New York, 1972).

64. L. I. Schiff, Quantum Mechanics, Third Edition (McGraw-Hill Book Company, New York, 1968).

65. R. Roy and B. Nigam, Nuclear Physics (John Wiley & Sons, Inc., New York, 1967).

66. K. J. Foley, R. S. Jones, S. J. Lindenbaum, W. A. Love, S. Ozaki, E. D. Platner, C. A. Quarles, and E. H. Willen, Phys. Rev. Lett. 19, 193 (1967).

67. H. A. Bethe, Ann. Phys. 3, 190 (1958).

68. C. B. West and D. R. Yennie, Phys. Rev. 172, 1413 (1968).

69. K. M. Watson, Phys. Rev. 118, 886 (1960).

70. R. H. Landau, S. C. Phatak, and F. Tabakin, Ann. Phys. (N.Y.) 78, 299 (1973).

71. R. R. Silbar and M. M. Sternheim, Phys. Rev. Lett. 31, 941 (1973).

72. G. A. Miller, Phys. Rev. C10, 1242 (1974).

73. E. Kujawski and G. A. Miller, Phys. Rev. C9, 1205 (1974).

74. L. S. Kisslinger and F. Tabakin, Phys. Rev. C9, 188 (1974).

75. R. H. Landau and F. Tabakin, Phys. Rev. D5, 2746 (1972).

76. J. Londergan, K. McVoy, and E. Moniz, Ann. Phys. (N.Y.) 86, 147 (1974).

77. S. C. Phatak, F. Tabakin, and R. H. Landau, Phys. Rev. C7, 1804 (1973).

78. R. H. Landau, Phys. Lett. 57B, 13 (1975).

79. R. H. Landau, Ann. Phys. (N.Y.) 92, 205 (1975).

80. R. F. Frosch, J. S. McCarthy, R. E. Rand, and M. R. Yearian, Phys. Rev. 160, 874 (1967).

81. R. H. Landau and A. W. Thomas, "The Necessity for an Improved Optical Potential in Low Energy Pion-Nucleus Scattering," Oregon State University preprint (1975).

82. J. F. Amann, P. D. Barnes, M. Doss, S. A. Dytman, R. A. Eisenstein, and A. C. Thompson, Phys. Rev. Lett. 35, 426 (1975).

83. E. V. Hungerford, G. S. Mutchler, G. C. Phillips, M. L. Scott, J. C. Allred, L. Y. Lee, B. W. Mayes, and C. Goodman, Nucl. Phys. A230, 515 (1974).

84. B. W. Mayes, L. Y. Lee, J. C. Allred, C. Goodman, G. S. Mutchler, E. V. Hungerford, M. L. Scott, and G. C. Phillips, Nucl. Phys. A230, 515 (1974).

85. W. T. Scott, Rev. Mod. Phys. 35, 231 (1963).

86. R. Heffner, Los Alamos Scientific Laboratory (LAMPF), private communication, 1975.

87. B. H. Bransden and R. G. Moorhouse, The Pion-Nucleon System (Princeton University Press, Princeton, N.J., 1973).

APPENDIX A: EFFICIENCY AND ABSORPTION CALCULATION

The expressions for T and S in terms of N, α, β, and ε are given below.

$$T_1 = \varepsilon_1 N_1$$

$$T_2 = \varepsilon_2 (N_2 + \alpha_2 N_1)$$

$$T_3 = \varepsilon_3 (N_3 + \beta_2 \alpha_2 N_2 + \alpha_3 N_1)$$

$$T_4 = \varepsilon_4 (N_4 + \beta_3 \alpha_2 N_3 + \beta_2^2 \alpha_3 N_2 + \alpha_4 N_1)$$

$$T_5 = \varepsilon_5 (N_5 + \beta_4 \alpha_2 N_4 + \beta_3^2 \alpha_3 N_3 + \beta_2^3 \alpha_4 N_2 + \alpha_5 N_1)$$

$$T_6 = \varepsilon_6 (N_6 + \beta_5 \alpha_2 N_5 + \beta_4^2 \alpha_3 N_4 + \beta_3^3 \alpha_4 N_3 + \beta_2^4 \alpha_5 N_2 + \alpha_6 N_1)$$

$$T_7 = \varepsilon_7 (N_7 + \beta_6 \alpha_2 N_6 + \beta_5^2 \alpha_3 N_5 + \beta_4^3 \alpha_4 N_4 + \beta_3^4 \alpha_5 N_3 + \beta_2^5 \alpha_6 N_2 + \alpha_7 N_1)$$

$$T_8 = \varepsilon_8 (N_8 + \beta_7 \alpha_2 N_7 + \beta_6^2 \alpha_3 N_6 + \beta_5^3 \alpha_4 N_5 + \beta_4^4 \alpha_5 N_4 + \beta_3^5 \alpha_6 N_3 + \beta_2^6 \alpha_7 N_2 + \alpha_8 N_1)$$

$$S_2 = \varepsilon_1 N_1 + \varepsilon_2 N_2 + (1 - \varepsilon_1) \alpha_2 \varepsilon_2 N_1$$

$$S_3 = S_2 + \varepsilon_3 N_3 + (1 - \varepsilon_1)(1 - \varepsilon_2) \alpha_3 \varepsilon_3 N_1 + (1 - \varepsilon_2) \alpha_2 \varepsilon_3 \beta_2 N_2$$

$$S_4 = S_3 + \varepsilon_4 N_4 + (1 - \varepsilon_1)(1 - \varepsilon_2)(1 - \varepsilon_3) \alpha_4 \varepsilon_4 N_1 + (1 - \varepsilon_2)(1 - \varepsilon_3) \alpha_3 \varepsilon_4 \beta_2^2 N_2 + (1 - \varepsilon_3) \alpha_2 \varepsilon_4 \beta_3 N_3$$

$$S_5 = S_4 + \varepsilon_5 N_5 + (1 - \varepsilon_1)(1 - \varepsilon_2)(1 - \varepsilon_3)(1 - \varepsilon_4) \alpha_5 \varepsilon_5 N_1 + (1 - \varepsilon_2)(1 - \varepsilon_3)(1 - \varepsilon_4) \alpha_4 \varepsilon_5 \beta_2^3 N_2 + (1 - \varepsilon_3)(1 - \varepsilon_4) \alpha_3 \varepsilon_5 \beta_3^2 N_3 + (1 - \varepsilon_4) \alpha_2 \varepsilon_5 \beta_4 N_4$$

$$S_6 = S_5 + \varepsilon_6 N_6 + (1-\varepsilon_1)(1-\varepsilon_2)(1-\varepsilon_3)(1-\varepsilon_4)(1-\varepsilon_5)\alpha_6\varepsilon_6 N_1$$
$$+ (1-\varepsilon_2)(1-\varepsilon_3)(1-\varepsilon_4)(1-\varepsilon_5)\alpha_5\varepsilon_6\beta_2{}^4 N_2$$
$$+ (1-\varepsilon_3)(1-\varepsilon_4)(1-\varepsilon_5)\alpha_4\varepsilon_6\beta_3{}^3 N_3$$
$$+ (1-\varepsilon_4)(1-\varepsilon_5)\alpha_3\varepsilon_6\beta_4{}^2 N_4 + (1-\varepsilon_5)\alpha_2\varepsilon_6\beta_5 N_5$$

$$S_7 = S_6 + \varepsilon_7 N_7$$
$$+ (1-\varepsilon_1)(1-\varepsilon_2)(1-\varepsilon_3)(1-\varepsilon_4)(1-\varepsilon_5)(1-\varepsilon_6)\alpha_7\varepsilon_7 N_1$$
$$+ (1-\varepsilon_2)(1-\varepsilon_3)(1-\varepsilon_4)(1-\varepsilon_5)(1-\varepsilon_6)\alpha_6\varepsilon_7\beta_2{}^5 N_2$$
$$+ (1-\varepsilon_3)(1-\varepsilon_4)(1-\varepsilon_5)(1-\varepsilon_6)\alpha_5\varepsilon_7\beta_3{}^4 N_3$$
$$+ (1-\varepsilon_4)(1-\varepsilon_5)(1-\varepsilon_6)\alpha_4\varepsilon_7\beta_4{}^3 N_4$$
$$+ (1-\varepsilon_5)(1-\varepsilon_6)\alpha_6\varepsilon_7\beta_5{}^2 N_5 + (1-\varepsilon_6)\alpha_2\varepsilon_7\beta_6 N_6$$

$$S_8 = S_7 + \varepsilon_8 N_8$$
$$+ (1-\varepsilon_1)(1-\varepsilon_2)(1-\varepsilon_3)(1-\varepsilon_4)(1-\varepsilon_5)(1-\varepsilon_6)(1-\varepsilon_7)\alpha_8\varepsilon_8 N_1$$
$$+ (1-\varepsilon_2)(1-\varepsilon_3)(1-\varepsilon_4)(1-\varepsilon_5)(1-\varepsilon_6)(1-\varepsilon_7)\alpha_7\varepsilon_8\beta_2{}^6 N_2$$
$$+ (1-\varepsilon_3)(1-\varepsilon_4)(1-\varepsilon_5)(1-\varepsilon_6)(1-\varepsilon_7)\alpha_6\varepsilon_8\beta_3{}^5 N_3$$
$$+ (1-\varepsilon_4)(1-\varepsilon_5)(1-\varepsilon_6)(1-\varepsilon_7)\alpha_5\varepsilon_8\beta_4{}^4 N_4$$
$$+ (1-\varepsilon_5)(1-\varepsilon_6)(1-\varepsilon_7)\alpha_4\varepsilon_8\beta_5{}^3 N_5$$
$$+ (1-\varepsilon_6)(1-\varepsilon_7)\alpha_3\varepsilon_8\beta_6{}^2 N_6 + (1-\varepsilon_7)\alpha_2\varepsilon_8\beta_7 N_7$$

These equations may be rewritten as

$$T_1 = \varepsilon_1 N_1$$

$$T_2 = \varepsilon_2 N_2 + \varepsilon_2\alpha_2 N_1 + X_2$$

$$T_3 = \varepsilon_3 N_3 + \varepsilon_3\alpha_3 N_1 + X_3$$

$$\vdots$$

$$T_8 = \varepsilon_8 N_8 + \varepsilon_8\alpha_8 N_1 + X_8$$

and

$$S_2 = \epsilon_2 N_2 + Y_2 \alpha_2 + Z_2$$

$$S_3 = \epsilon_3 N_3 + Y_3 \alpha_3 + Z_3$$

$$\vdots$$

$$S_8 = \epsilon_8 N_8 + Y_8 \alpha_8 + Z_8 \quad .$$

So that solving for N and α gives

$$N_1 = \frac{T_1}{\epsilon_1}$$

$$\alpha_i = \frac{T_i - X_i - S_i + Z_i}{\epsilon_1 N_1 - Y_i}$$

$$N_i = \frac{T_i - X_i - \epsilon_i \alpha_i N_1}{\epsilon_i}$$

where $i \geq 2$. The quantities X_i, Y_i, and Z_i are defined as follows where only the first three will be given.

$$X_2 \equiv 0$$

$$X_3 = \epsilon_3 (\beta_2 \alpha_2 N_2)$$

$$X_4 = \epsilon_4 (\beta_2^2 \alpha_3 N_2 + \beta_3 \alpha_2 N_3)$$

$$Y_2 = (1 - \epsilon_1)\epsilon_2 N_1$$

$$Y_3 = (1 - \epsilon_1)(1 - \epsilon_2)\epsilon_3 N_1$$

$$Y_4 = (1 - \epsilon_1)(1 - \epsilon_2)(1 - \epsilon_3)\epsilon_4 N_1$$

and

$$Z_2 = \varepsilon_1 N_1$$

$$Z_3 = \varepsilon_1 N_1 + \varepsilon_2 N_2 + (1 - \varepsilon_2)\alpha_2 \varepsilon_3 \beta_2 N_2 + (1 - \varepsilon_1)\alpha_2 \varepsilon_2 N_1$$

$$\begin{aligned} Z_4 = {} & \varepsilon_1 N_1 + \varepsilon_2 N_2 + \varepsilon_3 N_3 + (1 - \varepsilon_2)(1 - \varepsilon_3)\alpha_3 \varepsilon_4 \beta_2^2 N_2 \\ & + (1 - \varepsilon_3)\alpha_2 \varepsilon_4 \beta_3 N_3 + (1 - \varepsilon_1)(1 - \varepsilon_1)\alpha_3 \varepsilon_3 N_1 \\ & + (1 - \varepsilon_2)\alpha_2 \varepsilon_3 \beta_2 N_2 + (1 - \varepsilon_1)\alpha_2 \varepsilon_2 N_1 \end{aligned}$$

APPENDIX B: COVARIANCE OF S_i AND S_j

By definition the covariance $(\Delta S_{ij})^2$ of S_i and S_j is

$$(\Delta S_{ij}) = (S_i - \langle S_i \rangle)(S_j - \langle S_j \rangle)$$

$$= S_i S_j - \langle S_i \rangle \langle S_j \rangle$$

where $\langle S_i \rangle$ is the expectation value of S_i.

The probability that $S_i = X_0$ in Y trials is

$$P_r(S_i = X_0) = \binom{Y}{X_0} P_i^{X_0} (1 - P_i)^{Y - X_0}$$

where P_i is the probability of an event in S_i and $\langle S_i \rangle = YP_i$.

Now consider the covariance $(\Delta S_{i,i+1})$ which has the constraint $S_{i+1} = S_i + Z_i$. Let P_{i+1}, P_i, and Q_i be the probabilities of an event in S_{i+1}, S_i, and Z_i, respectively, where Z_i is the angular ring where S_i does not shadow S_{i+1}. Also let X, X_0, and k be the number of events in S_{i+1}, S_i, and Z_i. Then the probability Q_i for an event in Z_i is

$$Q_i = \frac{X - X_0}{Y - X_0}$$

$$= \frac{P_{i+1} - P_i}{1 - P_i}$$

where $X > X_0$.

Then the conditional probability for $Z_i = k$ when $S_i = X_0$ is

$$P_r(Z_i=k|S_i=X_0) = \binom{Y-X_0}{k}\left(\frac{P_{i+1}-P_i}{1-P_i}\right)^k\left(1-\frac{P_{i+1}-P_i}{1-P_i}\right)^{Y-X_0-k}$$

$$= \binom{Y-X_0}{k}(P_{i+1}-P_i)^k(1-P_{i+1})^{Y-X_0-k}(1-P_i)^{X_0-Y}$$

$$= \binom{Y-X_0}{X-X_0}(P_{i+1}-P_i)^{X-X_0}(1-P_{i+1})^{Y-X}(1-P_i)^{X_0-Y}$$

$$= P_r(S_{i+1}=X|S_i=X_0)$$

where $k = 0, 1, \ldots, Y-X_0$.

What is desired is the probability that $S_{i+1} = X$ and $S_i = X_0$

$$P_r(S_{i+1}=X \text{ and } S_i=X_0) = P_r(S_{i+1}=X|S_i=X_0)P_r(S_i=X_0)$$

$$= \binom{Y}{X_0}P_i^{X_0}\binom{Y-X_0}{X-X_0}(P_{i+1}-P_i)^{X-X_0}(1-P_{i+1})^{Y-X}$$

$$= \binom{Y}{X}\binom{X}{X_0}\left(\frac{P_i}{P_{i+1}-P_i}\right)^{X_0}(P_{i+1}-P_i)^X(1-P_{i+1})^{Y-X}$$

remembering that $X \geq X_0$. That this is the correct probability distribution is easily checked by summing over X_0 from 0 to X.

$$P_r(S_{i+1}=X) = \binom{Y}{X}(P_{i+1}-P_i)^X(1-P_{i+1})^{Y-X}\sum_{X_0=0}^{X}\binom{X}{X_0}\left(\frac{P_i}{P_{i+1}-P_i}\right)^{X_0}$$

$$= \binom{Y}{X}(P_{i+1}-P_i)^X(1-P_{i+1})^{Y-X}\left(1+\frac{P_i}{P_{i+1}-P_i}\right)^X$$

$$= \binom{Y}{X}P_{i+1}^X(1-P_{i+1})^{Y-X}$$

where the binomial theorem

$$(P+q)^n = \sum_{X=0}^{n} \binom{n}{X} p^X q^{n-X}$$

has been used.

Now for any $j \geq i$ and $X_j \geq X_i$

$$P_r(S_j=X_j \text{ and } S_i=X_i) = \binom{Y}{X_j}\binom{X_j}{X_i}\left(\frac{P_i}{P_j-P_i}\right)^{X_i}(P_j-P_i)^{X_j}(1-P_j)^{Y-X_j} .$$

This now permits $\langle X_i X_j \rangle$ to be calculated

$$\langle X_i X_j \rangle = \sum_{X_j=0}^{Y} \sum_{X_i=0}^{X_j} X_i X_j P_r(S_j=X_j \text{ and } S_i=X_i)$$

$$= \sum_{X_j=0}^{Y} X_j \binom{Y}{X_j}(P_j-P_i)^{X_j}(1-P_j)^{Y-X_j} \sum_{X_i=0}^{X} X_i \binom{X_j}{X_i}\left(\frac{P_i}{P_j-P_i}\right)^{X_i} .$$

The second summation can be done and

$$\sum_{X_i=0}^{X_j} X_i \binom{X_j}{X_i}\left(\frac{P_i}{P_j-P_i}\right)^{X_i} = X_j P_i P_j^{X_j-1}(P_j-P_i)^{-X_j} .$$

so that $\langle X_i X_j \rangle$ is given by

$$\langle X_i X_j \rangle = \sum_{X_j=0}^{Y} X_j^2 \binom{Y}{X_j} P_i P_j^{X_j-1}(1-P_j)^{Y-X_j}$$

$$= \frac{P_i}{P_j} \sum_{X_j=0}^{Y} X_j^2 \binom{Y}{X_j} P_j^{X_j}(1-P_j)^{Y-X_j}$$

$$= \frac{P_i}{P_j}\left[YP_j(1-P_j) + Y^2P_j^2\right]$$

$$= P_i[Y(1-P_j) + Y^2P_j] \quad .$$

Finally, the covariance $(\Delta S_{ij})^2$, $j > i$, is

$$(\Delta S_{ij})^2 = \langle S_iS_j \rangle - \langle S_i \rangle \langle S_j \rangle$$

$$= P_i[Y(1 - P_j) + Y^2P_j] - Y^2P_iP_j$$

$$= YP_i(1 - P_j) \quad .$$

This reduces to the variance $(\Delta S_i)^2$ for $i = j$.

APPENDIX C: COVARIANCE MATRIX FOR THE PARTIAL CROSS SECTIONS

The sample covariance[33] $(\Delta\sigma_{ij})$ for the partial cross sections σ_i and σ_j is

$$(\Delta\sigma_{ij})^2 = \lim_{N\to\infty} \frac{1}{N-1} \sum_{\ell=1}^{N} (\sigma_{i\ell} - \langle\sigma_i\rangle)(\sigma_{j\ell} - \langle\sigma_j\rangle)$$

where $\sigma_{i\ell}$ and $\sigma_{j\ell}$ are the ℓ-th observed values of σ_i and σ_j and $j \geq i$.

The partial cross sections σ_i are given by

$$\sigma_i = \frac{1}{nt} \ln \frac{R_{0i}}{R_i}$$

$$= \sigma(R_{0i}, R_i)$$

so that $(\sigma_i - \langle\sigma_i\rangle)$ can be expanded about $\langle R_{0i}\rangle$ and $\langle R_i\rangle$

$$(\sigma_i - \langle\sigma_i\rangle) = (R_{0i} - \langle R_{0i}\rangle)\left(\frac{\partial\sigma_i}{\partial R_{0i}}\right) + (R_i - \langle R_i\rangle)\left(\frac{\partial\sigma_i}{\partial R_i}\right) + \cdots$$

where the partial derivatives are evaluated at $\langle R_{0i}\rangle$ and $\langle R_i\rangle$, respectively. A good approximation to $(\sigma_i - \langle\sigma_i\rangle)$ is obtained by keeping only the first two terms in the series since for large Y, $R_{0i} \simeq \langle R_{0i}\rangle$ and $R_i \simeq \langle R_i\rangle$.

Using this result, one obtains the following expression for $(\Delta\sigma_{ij})^2$:

$$(\Delta\sigma_{ij})^2 \simeq \lim_{N\to\infty}\left(\frac{1}{N-1}\right)\sum_{\ell}\left[(R_{0i\ell}-\langle R_{0i}\rangle)\left(\frac{\partial\sigma_i}{\partial R_{0i}}\right)+(R_{i\ell}-\langle R_i\rangle)\left(\frac{\partial\sigma_i}{\partial R_i}\right)\right]$$

$$\times\left[(R_{0j\ell}-\langle R_{0j}\rangle)\left(\frac{\partial\sigma_j}{\partial R_{0j}}\right)+(R_{j\ell}-\langle R_j\rangle)\left(\frac{\partial\sigma_j}{\partial R_j}\right)\right]$$

$$\simeq \lim_{N\to\infty}\left(\frac{1}{N-1}\right)\sum_{\ell}\left[(R_{0i\ell}-\langle R_{0i}\rangle)(R_{0j\ell}-\langle R_{0j}\rangle)\left(\frac{\partial\sigma_i}{\partial R_{0j}}\right)\left(\frac{\partial\sigma_j}{\partial R_{0j}}\right)\right.$$

$$+(R_{i\ell}-\langle R_i\rangle)(R_{j\ell}-\langle R_j\rangle)\left(\frac{\partial\sigma_i}{\partial R_i}\right)\left(\frac{\partial\sigma_j}{\partial R_j}\right)$$

$$+(R_{0i\ell}-\langle R_{0i}\rangle)(R_{j\ell}-\langle R_j\rangle)\left(\frac{\partial\sigma_i}{\partial R_{0i}}\right)\left(\frac{\partial\sigma_j}{\partial R_j}\right)$$

$$\left.+(R_{i\ell}-\langle R_i\rangle)(R_{0j\ell}-\langle R_{0j}\rangle)\left(\frac{\partial\sigma_i}{\partial R_i}\right)\left(\frac{\partial\sigma_j}{\partial R_{0j}}\right)\right]$$

where the last two terms are zero since there is no correlation between R_{0i} and R_j or between R_i and R_{0j}, so that

$$(\Delta\sigma_{ij})^2 \simeq \lim_{N\to\infty}\left(\frac{1}{N-1}\right)\sum_{\ell}\left[(R_{0i\ell}-\langle R_{0i}\rangle)(R_{0j\ell}-\langle R_{0j}\rangle)\left(\frac{\partial\sigma_i}{\partial R_{0i}}\right)\left(\frac{\partial\sigma_j}{\partial R_{0j}}\right)\right.$$

$$\left.+(R_{i\ell}-\langle R_i\rangle)(R_{j\ell}-\langle R_j\rangle)\left(\frac{\partial\sigma_i}{\partial R_i}\right)\left(\frac{\partial\sigma_j}{\partial R_j}\right)\right] .$$

If it is noted that the covariance $(\Delta R_{ij})^2$ is

$$(\Delta R_{ij})^2 = \lim_{N\to\infty}\left(\frac{1}{N-1}\right)\sum_{\ell}(R_{i\ell}-\langle R_i\rangle)(R_{j\ell}-\langle R_j\rangle),$$

then

$$(\Delta\sigma_{ij})^2 = (\Delta R_{0ij})^2\left(\frac{\partial\sigma_i}{\partial R_{0i}}\right)\left(\frac{\partial\sigma_j}{\partial R_{0j}}\right)+(\Delta R_{ij})^2\left(\frac{\partial\sigma_i}{\partial R_i}\right)\left(\frac{\partial\sigma_j}{\partial R_j}\right) .$$

The partial derivatives are given by

$$\left(\frac{\partial\sigma_i}{\partial R_{0i}}\right) = (nt\langle R_{0i}\rangle)^{-1}$$
$$\simeq (ntR_{0i})^{-1}$$

and

$$\left(\frac{\partial\sigma_i}{\partial R_i}\right) = -(nt\langle R_i\rangle)^{-1}$$
$$\simeq -(ntR)^{-1}$$

so that

$$(\Delta\sigma_{ij})^1 = \left(\frac{1}{nt}\right)^2\left(\frac{(\Delta R_{0ij})^2}{R_{0i}R_{0j}} + \frac{(\Delta R_{ij})^2}{R_iR_j}\right) .$$

In Appendix B it was shown that

$$(\Delta S_{ij})^2 = YR_i(1 - R_j)$$

or

$$(\Delta R_{ij})^2 = \left(\frac{1}{Y}\right)R_i(1 - R_j)$$

so that

$$(\Delta\sigma_{ij})^2 = \left(\frac{1}{nt}\right)^2\left(\frac{1 - R_{0j}}{YR_{0j}} + \frac{1 - R_j}{YR_j}\right)$$

$$= (\Delta\sigma_j)^2$$

where $j \geq i$ and $(\Delta\sigma_j)^2$ is the variance of σ_j.

The covariance matrix V for the partial cross sections can now be constructed using the expression for $(\Delta\sigma_{ij})^2$. From equation (57), V was defined by

$$V_{ij} = \langle(\sigma_i - \langle\sigma_i\rangle)(\sigma_j - \langle\sigma_j\rangle)\rangle$$
$$= (\Delta\sigma_{ij})^2$$

therefore

$$V_{ij} = (\Delta\sigma_j)^2$$

for $j \geq i$. Because V is symmetric, then $V_{ji} = V_{ij}$.

The above expression for V is appropriate when equation (48) is used to fit the σ_i. However, if equation (49) is used to fit the $\ln(\sigma_i)$, then it is necessary to know the covariance matrix for the $\ln(\sigma_i)$'s and $\ln(\sigma_j)$'s. To do this, let

$$X_i = \ln(\sigma_i)$$

with a variance $(\Delta X_i)^2$ given by

$$(\Delta X_i)^2 = \left(\frac{\Delta\sigma_i}{\sigma_i}\right) \quad .$$

The covariance matrix for the X_i's and X_j's is

$$(\Delta X_{ij})^2 = \lim_{N\to\infty} \left(\frac{1}{N-1}\right) \sum_{\ell=1}^{N} (X_{i\ell} - \langle X_i\rangle)(X_{j\ell} - \langle X_j\rangle) .$$

By expanding $(X_i - \langle X_i\rangle)$ about $\langle X_i\rangle$, one obtains

$$(X_i - \langle X_i\rangle) \simeq (\sigma_i - \langle\sigma_i\rangle)\left(\frac{\partial X_i}{\partial\sigma_i}\right)$$

where

$$\frac{\partial X_i}{\partial\sigma_i} = \frac{1}{\sigma_i} \quad .$$

Then

$$(\Delta X_{ij})^2 = \lim_{N\to\infty} \left(\frac{1}{N-1}\right) \sum_{\ell=1}^{N} (\sigma_{i\ell} - \langle\sigma_i\rangle)(\sigma_{j\ell} - \langle\sigma_j\rangle) \left[\frac{\partial X_i}{\partial \sigma_i}\right] \left[\frac{\partial X_j}{\partial \sigma_j}\right]$$

$$= \frac{(\Delta\sigma_{ij})^2}{\sigma_i \sigma_j}$$

$$= \frac{(\Delta\sigma_j)^2}{\sigma_i \sigma_j}$$

for $j \geq i$. The covariance matrix is then

$$V_{ij} = \frac{(\Delta\sigma_j)^2}{\sigma_i \sigma_j}$$

and $V_{ji} = V_{ij}$, since V is symmetric.

APPENDIX D: COVARIANCE FORM OF THE METHOD OF LEAST SQUARES

In this appendix, it will be shown how the best values of a_j, to be used in

$$\sigma_i(a_j) = \sum_{j=0}^{N} a_j t_i^j \quad ,$$

are determined by minimizing M for each a_j.

From equation (56), M is defined by

$$M = D^T V^{-1} D$$

where V is the covariance matrix with elements $V_{ij} = (\Delta\sigma_j)^2$ for $j \geq i$ (with $V_{ji} = V_{ij}$) and D is a vector with components $D_i = \sigma_i - \sigma_i(a_j)$.

Now M can also be written as

$$M = \sum_{k=1}^{P} \sum_{j=1}^{P} D_k R_{kj} D_j \quad ,$$

where $R = V^{-1}$ and P is the number of data points to be fit.

In the case of uncorrelated errors, then $V_{ij} = 0$ for $i \neq j$ and $V_{ii} = (\Delta\sigma_i)^2$ so that M reduces to the standard χ^2 given by

$$\chi^2 = \sum_{i=1}^{P} \frac{(\sigma_i - \sigma_i(a_j))^2}{(\Delta\sigma_i)^2} \quad .$$

Now using $D_i = \sigma_i - \sum_{n=0}^{N} a_n t_i^n$ where N is the order of the polynomial to be used in the fit, one obtains

$$M = \sum_{k=1}^{P} \sum_{j=1}^{P} R_{kj} D_k D_j$$

$$= \sum_{k=1}^{P} \sum_{j=1}^{P} R_{kj} \left(\sigma_k - \sum_{n=0}^{N} a_n t_k^n \right) \left(\sigma_j - \sum_{\ell=0}^{N} a_\ell t_j^\ell \right)$$

$$= \sum_{k=1}^{P} \sum_{j=1}^{P} R_{kj} \left(\sigma_k \sigma_j - \sigma_k \sum_{\ell=0}^{N} a_\ell t_j^\ell - \sigma_j \sum_{n=0}^{N} a_n t_k^n + \sum_{n=0}^{N} a_n t_k^n \sum_{\ell=0}^{N} a_\ell t_j^\ell \right).$$

To minimize M with respect to a_m, $\frac{\partial M}{\partial a_m}$ is calculated and set equal to zero so

$$0 = \frac{\partial M}{\partial a_m}$$

$$= \sum_{k=1}^{P} \sum_{j=1}^{P} R_{kj} \left(-\sigma_k t_j^m - \sigma_j t_k^m + t_k^m \sum_{\ell=0}^{N} a_\ell t_j^\ell + t_j^m \sum_{n=0}^{N} a_n t_k^n \right)$$

$$= \sum_{k=1}^{P} \sum_{j=1}^{P} R_{kj} \left(\sigma_k t_j^m + \sigma_j t_k^m \right) - \sum_{k=1}^{P} \sum_{j=1}^{P} R_{kj} \sum_{n=0}^{N} a_n (t_k^m t_j^n + t_j^m t_k^n) .$$

It is now useful to make some definitions

$$U_m = \sum_{k=1}^{P} \sum_{j=1}^{P} R_{kj} \left(\sigma_k t_j^m + \sigma_j t_k^m \right)$$

and

$$H_{nm} = \sum_{k=1}^{P} \sum_{j=1}^{P} R_{kj} \left(t_j^n t_k^m + t_k^n t_j^m \right)$$

$$= \frac{\partial^2 M}{\partial a_n \partial a_m} .$$

This gives

$$U_m = \sum_{n=0}^{N} a_n H_{nm}$$

or, in matrix notation

$$U = aH .$$

This leads to

$$a = UH^{-1}$$

or

$$a_n = \sum_{m=0}^{N} U_m (H^{-1})_{mn} \quad ,$$

which is the desired result.

To find the variance $(\Delta a_n)^2$ of a_n, first expand $(\sigma_i - \langle\sigma_i\rangle)$ in a_i about $\langle a_i \rangle$ to first order so that

$$\sigma_i - \langle\sigma_i\rangle = \sum_{n=0}^{N} \left(\frac{\partial \sigma_i}{\partial a_n}\right)(a_n - \langle a_n \rangle) \quad .$$

Then

$$\langle(\sigma_i - \langle\sigma_i\rangle)(\sigma_j - \langle\sigma_j\rangle)\rangle = \sum_{n=0}^{N} \sum_{m=0}^{N} \left(\frac{\partial \sigma_i}{\partial a_n}\right)\left(\frac{\partial \sigma_i}{\partial a_m}\right)\langle(a_n - \langle a_n\rangle)(a_m - \langle a_m\rangle)\rangle$$

or

$$V_{ij} = \sum_{n=0}^{N} \sum_{m=0}^{N} t_i^n t_j^m A_{nm} \quad ,$$

where

$$A_{nm} = \langle(a_n - \langle a_n\rangle)(a_m - \langle a_m\rangle)\rangle \quad .$$

Then, using $R = V^{-1}$, one obtains

$$1 = \sum_{i=1}^{P} \sum_{j=1}^{P} R_{ij} V_{ij}$$

$$= \sum_{i=1}^{P} \sum_{j=1}^{P} \sum_{n=0}^{N} \sum_{m=0}^{N} R_{ij} t_i^n t_j^m A_{nm} \quad .$$

This implies that the matrix inverse of A has the elements

$$(A^{-1})_{nm} = \sum_{i=1}^{P} \sum_{j=1}^{P} R_{ij} t_i^n t_j^m \quad .$$

Using the definition of H_{nm} and the fact that A_{nm} is symmetric, one obtains

$$H_{nm} = 2(a^{-1})_{nm}$$

or

$$A_{nm} = \frac{1}{2}(H^{-1})_{nm} \quad .$$

Finally, the variance $(\Delta a_n)^2 = A_{nn}$ is given by

$$(\Delta a_n)^2 = \frac{1}{2}(H^{-1})_{nn} \quad .$$

APPENDIX E· MONTE CARLO CALCULATIONS

In this appendix, the Monte Carlo computer programs used to calculate the multiple and single Coulomb scattering corrections $\sigma_m(\Omega)$ and $\sigma_c(\Omega)$, respectively, and the pion decay correction $\sigma_D(\Omega)$ to the measured partial cross sections will be discussed briefly.

A right-handed coordinate system was used in these programs. The origin was located at the perpendicular intersection of the beam axis, which was horizontal and passed through the center of the target. The positive z axis lay along the beam axis in the downstream direction· the positive y axis was in the upward direction from the beam axis; and the positive x axis was to the left of the beam axis (i.e., it was to the left if one was looking downstream).

Multiple Coulomb Scattering

The Monte Carlo computer program for calculating the multiple Coulomb scattering correction started with an individual pion at the upstream face of TOF2. It then followed the pion's history until it hit or missed the transmission stack. It repeated this process for thousands of events for both target "in" and target "out" to obtain the distribution of pions at the transmission stack for the two situations. With this information, it was possible to calculate the multiple Coulomb scattering correction $\sigma_m(\Omega)$ to the measured partial cross sections.

The calculation began with a random selection of both the pion's x and y positions and its divergencies $\frac{dx}{dz}$ and $\frac{dy}{dz}$ in the xz and yz planes, respectively, at the upstream face of TOF2. From the MWPC data, the pion distributions in x, y, $\frac{dx}{dz}$, and $\frac{dy}{dz}$ were found to be nearly Gaussian. Therefore, these quantities were chosen randomly from the Gaussian distribution f(x)

$$f(x) = \exp\left[-\frac{(x - x_0)^2}{2\sigma_x^2}\right] ,$$

where f(x) is characterized by a central value x_0, a standard deviation σ_x, and a cutoff width w_x (it provided a cutoff point on the tail of the distribution). Here, x_0, σ_x, and w_x were obtained from the MWPC data. It should be noted that $0 \leq f(x) \leq 1$.

After the pion's position and divergence were selected, its multiple Coulomb scattering in TOF2 was simulated by the random selection of a multiple scattering angle chosen from the distribution given in equations (62) and (63)

$$f(\theta) = \frac{1}{\chi_c^2 B}\left[f_0(\theta) + \frac{1}{B} f_1(\theta) + \frac{1}{2B^2} f_2(\theta) + \cdots\right]$$

and

$$f_k(\theta) = k!\int_0^\infty u J_0\left(\frac{u\theta}{\chi_c B^{1/2}}\right) \exp\left(-\frac{u^2}{4}\right)\left(\frac{u^2}{4} \ln\left(\frac{u^2}{4}\right)\right)^k ,$$

which were modified as in the work of E.V. Hungerford et al.[83] to give $f(\theta_p)$ and $f_k(\theta_p)$. Here, θ_p is the projected angle of θ onto some plane (e.g., the xz and yz planes). This parameter was used because it was more convenient to work with the projected angles than with the

spatial angle. As in the work of B.W. Mayes et al.[84] the $f_k(\theta_p)$ were written in terms of a set of functions $D_k(a;b;z)$, defined by

$$D_k(a;b;z) = \frac{\partial^k}{\partial a^k}\Gamma(a)\,{}_1F_1(a;b;z) \quad ,$$

where $\Gamma(a)$ is the gamma function and ${}_1F_1$ is Kummer's confluent hypergeometric function. The D_k functions are described and tabulated as a function of $\sigma_p/(\chi_c B^{1/2})$ in the paper by W.T. Scott.[85] It was found necessary to keep only f_0 and f_1 in the expression for $f(\theta_p)$. With f expressed in terms of D_0 and D_1, a table of $f(\theta_p)$ versus θ_p was created, and θ_p was chosen randomly from it. The portion of the computer code which handled the multiple scattering was originated and developed by R. Heffner.[86]

After selecting the multiple scattering angle of the pion in TOF2, the program did one of two things. For a simulated target "out" run, it translated the pion in a straight line to the transmission stack to find which counter it hit. For a simulated target "in" run, it translated the pion in a straight line to the upstream face of the target. Multiple scattering in the target was simulated in the same way as it was in TOF2. After selecting the multiple scattering angle, the program translated the pion in a straight line to the transmission stack to determine which counter it hit. The energy loss of the pion in both TOF2 and the target was included in the random selection of the multiple scattering angles.

After repeating the above procedure for several thousand events for both target "in" and "out," the program then calculated $r(\Omega)$ and $r_0(\Omega)$, the fraction of pions starting at the upstream face of TOF2

and hitting the i-th transmission counter for target "in" and "out," respectively. For nt nuclei/cm^2 in the target, the multiple Coulomb scattering correction $\sigma_m(\Omega)$ for each partial cross section was calculated from

$$\sigma_m(\Omega) = \frac{1}{nt} \ln \left[\frac{r_0(\Omega)}{r(\Omega)} \right] .$$

Single Coulomb Scattering

The calculation of multiple and single Coulomb scattering corrections were similar. They differed in that in the latter there was no target "out" calculation.

To simulate single Coulomb scattering, it was necessary to determine the appropriate probability distribution from which the scattering angle could be randomly selected. To see how this was done, consider the expression

$$P(\Omega) = e^{-nt\sigma_c(\Omega)} ,$$

where $\sigma_c(\Omega)$ is the Coulomb cross section for a pion scattering outside the solid angle Ω, nt is the number of nuclei/cm^2, and $P(\Omega)$ is the probability that a pion will not scatter outside Ω. It should be noted that P is uniformly distributed between 0 and 1 for $0 \leq \Omega \leq 4\pi$. For convenience the pion and ^{4}He nucleus were assumed to be point charges, so that

$$\sigma_c(\Omega) = \int_0^{2\pi} \int_\theta^\pi \left(\frac{d\sigma}{d\Omega}\right)_c \sin\theta' \, d\theta' \, d\phi$$

$$= \pi \left(\frac{Ze^2E}{c^2p^2}\right)^2 \left(\frac{1 + \cos\theta}{1 - \cos\theta}\right) \quad ,$$

where as given in equation (79),

$$\left(\frac{d\sigma}{d\Omega}\right)_c = \frac{1}{4} \left(\frac{Ze^2E}{c^2p^2}\right) \frac{1}{\sin^4(\theta/2)} \quad .$$

Here, Z is the charge of the nucleus, e is the electron charge, c is the velocity of light in vacuum, and E, p, and θ are the pion total energy, momentum, and scattering angle in the laboratory, respectively. With the above result for $\sigma_c(\Omega)$, one can write the probability distribution $P(\theta)$, from which θ was randomly chosen as

$$P(\theta) = \exp\left[-\pi nt \left(\frac{Ze^2E}{c^2p^2}\right)\left(\frac{1 + \cos\theta}{1 - \cos\theta}\right)\right] \quad .$$

However, this is unwieldly at small angles because the Coulomb cross section becomes infinite as θ goes to zero. Consequently a minimum angle θ_m was chosen such that for $\theta < \theta_m$ the pion was considered not to have scattered since it would hit the second transmission counter anyway. (It should be remembered that in the experiment any pion hitting the second transmission was considered to be an unscattered pion.) The probability for not scattering at an angle greater than θ_m is given by $P_m(\theta_m) > 0$. So in selecting an angle θ from the expression for $P(\theta)$, the acceptable range for $P(\theta)$ was $P_m \leq P \leq 1$ rather than $0 \leq P \leq 1$.

The program calculated the correction to the measured partial cross section from the following expression:

$$\sigma_c(\Omega) = -\frac{1}{nt} \ln\left(1 - \frac{m(\Omega)}{Y}\right) \quad ,$$

where $m(\Omega)$ was the number of pions scattered outside of the i-th transmission counter as determined from the program. Here, Y is the total number of pions incident on the target and is related to Y', the number of scattered events handled by the program for which $\theta > \theta_m$, by

$$Y = \frac{Y'}{1 - P_m} \quad .$$

If $P_c(\Omega)$ is the probability for a pion to single Coulomb scatter within the solid angle Ω, then

$$P_c(\Omega) = 1 - \frac{m(\Omega)}{Y}$$

and

$$\sigma_c(\Omega) = -\frac{1}{nt} \ln P_c(\Omega) \quad .$$

Pion Decay

As stated in Chapter IV, the calculation of the pion decay correction was concerned only with those pions which decayed after leaving the target. Multiple scattering in the target was included although for convenience only the gaussian term in the multiple scattering distribution was considered. The finite size and divergence of the beam were also included in the program, as well as the large-angle tail of its distribution. The program started with an

individual pion at the upstream face of the target and followed its history until it or its decay muon hit the transmission stack. By repeating this process for thousands of events, the program calculated the muon distribution at the transmission stack.

In following the pion from the target to the transmission stack, the distance it traveled before decaying and the angle which the decay muon made with the original pion trajectory were randomly chosen. The distance ℓ traveled by the pion before decaying was chosen from the distribution

$$P(\ell) = e^{-\ell/\lambda} \quad ,$$

where $\lambda \equiv \lambda(p)$ is the mean decay length and $P(\ell)$ is the probability that the pion will not decay in traveling a distance ℓ. The mean decay length is a function of the pion momentum p and is different for target "in" and "out" runs. In choosing ℓ, $P(\ell)$ was restricted to the range $e^{-\ell_m/\lambda} \geq P(\ell) \geq 1$ rather than $0 \geq P(\ell) \geq 1$, where ℓ_m was the maximum distance the pion could travel before being detected in the transmission stack.

The angle between the trajectories of the decay muon and the parent pion was chosen in the pion rest frame, where the decay is isotropic, and transformed to the laboratory frame. Because of the energy difference between the target "in" and "out" runs, the angular distributions in the laboratory were different for the two cases.

After generating the muon distributions at the transmission stack for both the target 'in" and target "out" situations, the

program calculated the decay corrections to the measured partial cross sections using equation (192). The exact correction depends very sensitively on the actual number of pions that decayed and the number of decay muons that were detected, for both target "in" and "out."

APPENDIX F. FORWARD DISPERSION RELATIONS

In this appendix, some of the basic features of forward dispersion relations will be discussed. A more detailed account may be found in the papers by Ericson and Locher[3] and by Batty, Squier, and Turner,[4] and in the texts by Taylor[64] and by Bransden and Moorhouse.[87]

The forward amplitude $f(0°)$ is a function of the total laboratory energy $\omega = (k^2 + m^2)^{1/2}$, where k is the momentum and m the rest mass, and will be written as $f(\omega) \equiv f(\omega, 0°)$. It is useful to allow ω to be complex. Then it is assumed that $f(\omega)$ is an analytic function of the complex energy ω for all ω, apart from certain cuts and poles. Also it is assumed that there are no singularities in $f(\omega)$ for $\mathrm{Im}\,\omega > 0$.

Now by assumption, the scattering amplitude $f(\omega)$ is analytic for $\mathrm{Im}\,\omega > 0$ so that Cauchy's theorem can be applied

$$f(\omega) = \frac{1}{2\pi i} \oint_C \frac{f(z)}{(z - \omega)}\, dz \tag{181}$$

The path of integration is along the closed contour C consisting of a segment along the real axis from $z = -L$ to $z = +L$ and closed by a semicircle of radius L in the upper half plane, where ω lies within the contour C. If the integrand is sufficiently small at infinity, so that in the limit $L \to \infty$ the distant contribution to the integral is negligible, then the only contribution to the integral will come from the real axis

$$F(\omega) = \frac{1}{2\pi i} \int_{-\infty}^{\infty} \frac{f(z)}{(z - \omega)} dz \quad . \tag{182}$$

By writing $\omega \to \omega + i\epsilon$, where ω and ϵ are real, $\epsilon > 0$, and taking the limit as ϵ goes to zero, $f(\omega)$ is given by

$$f(\omega) = \frac{1}{i\pi} P \int_{-\infty}^{\infty} \frac{f(z)}{(z - \omega)} dz \quad , \tag{183}$$

where P denotes that a principal value integral is to be taken. By separating the real and imaginary parts of $f(\omega)$, the basic forward dispersion relations are given by

$$\mathrm{Re}\, f(\omega) = \frac{1}{\pi} P \int_{-\infty}^{\infty} \frac{\mathrm{Im}\, f(z)}{(z - \omega)} dz \tag{184}$$

and

$$\mathrm{Im}\, f(\omega) = \frac{1}{\pi} P \int_{-\infty}^{\infty} \frac{\mathrm{Re}\, f(z)}{(z - \omega)} dz \tag{185}$$

In this work only equation (184) is of interest. It is characteristic that this relation involves positive and negative energies. To use this relation, $\mathrm{Im}\, f(\omega)$ for all real ω must be expressed in terms of measurable or calculable physical quantities.

Frequently equation (184) does not converge because the distant contribution does not vanish. Any function of $f(\omega)$ that is analytic in the upper half plane could be used in this expression in place of $f(\omega)$, such as $(\omega - \omega_0)^{-1}[f(\omega) - f(\omega_0)]$, where ω_0 is an arbitrary but fixed energy. If this is done, equation (184) becomes

$$\mathrm{Re}\, \frac{f(\omega) - f(\omega_0)}{\omega - \omega_0} = \frac{1}{\pi} P \int_{-\infty}^{\infty} \frac{\mathrm{Im}[f(z) - f(\omega_0)]}{(z - \omega_0)(z - \omega)} dz \tag{186}$$

or

$$\mathrm{Re}\, f(\omega) = \mathrm{Re}\, f(\omega_0) + \frac{\omega - \omega_0}{\pi} P \int_{-\infty}^{\infty} \frac{\mathrm{Im}\, f(z)}{(z - \omega_0)(z - \omega)} dz \tag{187}$$

Equation (187) could be obtained formally by subtracting $f(\omega_0)$ from equation (184), so that Re $f(\omega_0)$ is known as a subtraction term. Further convergence may be obtained by repeated subtractions. The price paid for convergence is that $f(\omega_0)$ is unknown.

Another relation that is necessary before applying the general relationship of equation (187) is the crossing relation. This relates the scattering amplitude $f(\omega)$ of the particle to the scattering amplitude $\bar{f}(\omega)$ of its antiparticle according to

$$f(-\omega) = \bar{f}^*(\omega). \tag{188}$$

Also it should be noted that $\mathrm{Im}\, f(-\omega) = -\mathrm{Im}\, \bar{f}(\omega)$.

In the physical region, $\mathrm{Im}\, f(\omega)$ is measurable. From the total cross section $\sigma(\omega)$ and the optical theorem,

$$\mathrm{Im}\, f(\omega) = \frac{k\sigma(\omega)}{4\pi}, \quad \omega > m_\pi .$$

For the antiparticle of energy $\bar{\omega} = -\omega > m_\pi$ and momentum $\bar{k}$,

$$\mathrm{Im}\, \bar{f}(\bar{\omega}) = \frac{\bar{k}\sigma(\bar{\omega})}{4\pi}$$

so that

$$\mathrm{Im}\, f(\omega) = -\frac{k\bar{\sigma}(-\omega)}{4\pi}, \quad \omega < -m_\pi .$$

The last equation follows from the crossing relation.

The unphysical region for π-nucleus scattering includes in general many poles corresponding to nuclear excited states, and pion absorption extends as a cut below the threshold for scattering.

The amplitude to be used is $f^+(\omega)$ defined by

$$f^+(\omega) = \frac{1}{2}[f_{\pi^+}(\omega) + f_{\pi^-}(\omega)], \tag{189}$$

which is symmetric under crossing $f^+(-\omega) = +f^{+*}(\omega)$, with the corresponding total cross section

$$\sigma^+(\omega) = \frac{1}{2}[\sigma_{\pi^-}(\omega) + \sigma_{\pi^+}(\omega)]. \tag{190}$$

In equation (187) it is convenient to do the subtraction at the threshold for scattering with $\omega_0 = m_\pi$. Collecting the above results and using $k^2 = \omega^2 - m_\pi^2$, the forward dispersion relation for f^+ for π-nucleus scattering becomes

$$\text{Re } f^+(\omega) - \text{Re } f^+(m_\pi) = \sum_i \frac{2\omega_i r_i}{\omega^2 - \omega_i^2} \frac{k^2}{k_i^2} + \frac{2k^2}{\pi} P\int_{\omega_1}^{\infty} \frac{\omega' d\omega' \, \text{Im } f^+(\omega')}{k'^2(\omega'^2 - \omega^2)} \tag{191}$$

The summation term on the LHS of equation (191) is the contribution of the poles in the unphysical region, where ω_i, k_i, and r_i are the total energy, the momentum, and the residue of the i-th pole. Also, ω_1 is an energy close to $\omega = 0$ so that the unphysical region in equation (191) is $0 = \omega_1 < \omega < m$.

It is argued by Ericson and Locher[3] that the contribution of the pole terms can be neglected, so that the final expression for the dispersion relation becomes

$$\text{Re } f^+(\omega) = \text{Re } f^+(m_\pi) + \frac{2k^2}{\pi} P\int_0^{\infty} \frac{\omega' d\omega' \, \text{Im } f^+(\omega)}{k'^2(\omega'^2 - \omega^2)} \tag{192}$$

where $\text{Im } f^+(\omega') = \dfrac{k'\sigma^+(\omega')}{4\pi}$. It was this expression that Batty, Squier, and Turner[4] used in their calculations.

☆ U S GOVERNMENT PRINTING OFFICE 1976—777-018/13